High Field EPR and ENDOR Investigations on Radicals and Metal Centers in Subunit R2 Wild Type and Mutant Class Ia Ribonucleotide Reductase

vorgelegt von
Master of Arts
Günther Bleifuß
aus Aschaffenburg

Von der Fakultät II - Mathematik und Naturwissenschaften -
der Technischen Universität Berlin
zur Erlangung des akademischen Grades

Doktor der Naturwissenschaften
- Dr. rer. nat.-

genehmigte Dissertation

Promotionsausschuß:

Vorsitzender:	Prof. Dr. Ralf Steudel
Berichter:	Prof. Dr. Wolfgang Lubitz
Berichter:	Priv.-Doz. Dr. Günter Laßmann

Tag der mündlichen Prüfung: 5.Juli.2001

Berlin 2001

D 83

High Field EPR and ENDOR Investigations on Radicals and Metal Centers in Subunit R2 of Wildtype and Mutant Class IA Ribonucleotide Reductase

Abstract

Ziel dieser Arbeit ist die Aufklärung der elektronischen Struktur paramagnetischer Zentren in der Untereinheit R2 von Wildtyp als auch Mutanten Protein des Enzyms Ribonucleotide Reduktase in Bakterium *Escherichia coli* und Maus. Untersucht werden transiente Tryptophanradikale in den Mutanten Y177W (Mausprotein) und R2-Y122F (*E. coli*), sowie ein stabiles paramagnetisches Zweieisenzentrum (Zentrum H), das in der Mutante R2-Y122H auftritt. Verwendet werden hierzu moderne Methoden der EPR, wie Hochfeld-EPR sowie CW- und gepulste ENDOR Techniken. Die proteinassoziierten Tryptophanradikale als auch die im entsprechenden Wildtypprotein auftretenden Tyrosinradikale werden mit EPR im Hochfeld (Mikrowellenfrequenz: 94 GHz) charakterisiert und verglichen. Aufgrund der etwa zehnfachen Zeemanaufspaltung im Vergleich zu X-Band (9.7 GHz) und der damit verbundenen besseren Auflösung des g-Tensors kann gezeigt werden, dass sich beide Radikaltypen mittels ihrer charakteristischen g-Tensorhauptwerte im W-Band bereits ohne aufwendige Isotopenmarkierung eindeutig voneinander unterscheiden lassen.
Ein bisher nicht charakterisiertes paramagnetisches Zentrum (Zentrum H), das in R2-Y122H auftritt, zeigt im X-Band ein inhomogen verbreitertes Singulett ohne aufgelöste Hyperfeinstruktur b.z.w. g-Anisotropie. Es wird gezeigt, dass im Hochfeld bei 94 GHz der g-Tensor vollständig aufgelöst ist. Die g-Tensor Hauptwerte für Zentrum H können somit bestimmt und mit Werten aus früheren Messungen an bekannten paramagnetischen Fe(II)Fe(III) und Fe(III)Fe(IV) Zweieisenzentren verglichen werden. Zentrum H in ^{57}Fe substituiertem Protein R2-Y122H zeigt eine Verbreiterung der Linie von 2.2 mT auf 4.3 mT im X-Band, was auf eine starke, aber unaufgelöste Eisenkopplung hinweist. Mittels Davies Puls-ENDOR sowie CW-ENDOR konnten zwei ^{57}Fe Hfs-Tensoren vollständig aufgelöst werden. Der Vergleich der isotropen als auch anisotropen Anteile beider Tensoren mit ^{57}Fe Tensoren, wie sie für mixed-valence Fe(III)Fe(IV) und Fe(II)(III) Zentren theoretisch erwartet und auch gemessen wurden, ergibt keine befriedigende Übereinstimmung. Daher wird ein Modell vorgeschlagen, das eine Kopplung von 3 Spins untereinander beschreibt, und in dem beide Eisenatome (beide high spin Fe(III), daher jeweils S=5/2) miteinander und mit einem S=1/2 Ligandenradikal zu einem S=1/2 Grundzustand gekoppelt sind. Die ^{57}Fe Kopplungen, die sich aus diesem Modell berechnen lassen, stehen in guter Übereinstimmung mit den Messungen an Zentrum H. ^{14}N und ^{15}N CW- und Puls-ENDOR an Zentrum H ermöglicht die Identifizierung zweier koordinierter Stickstoffatome und ihre Zuordnung zu dem Imidazol-N_δ von zwei Histidinen. Aufgrund der hohen Stabilität von Zentrum H ist es möglich, R2-Y122H Kristalle zu ziehen, in denen sich das orientierte Zentrum H im Hochfeld charakterisieren läßt. Basierend auf ersten Messungen konnte das g-Tensor Rotationspattern des Zentrums H im Kristall im W-Band simuliert werden und eine vorläufige Zuordnung der Orientierung der Hauptachsen des g-Tensors in die Molekülstruktur des Zentrums vorgeschlagen werden. Basierend auf den Ergebnissen dieser Arbeit wird Zentrum H als Fe(III)Fe(III) Zentrum plus Ligandenradikal interpretiert.

Teile der vorliegenden Arbeit wurden bereits veröffentlicht:

[1] G. Bleifuss, M. Kolberg, S. Pötsch, W. Lubitz, A. Gräslund, G. Lassmann, and F. Lendzian, *Tryptophan and Tyrosine Radicals in Ribonucleotide Reductase: A Comparative High-Field EPR Study at 94 GHz*, submitted to Biochemistry

[2] M. Kolberg, G. Bleifuss, S. Pötsch, A. Gräslund, W. Lubitz, G. Lassmann, and F. Lendzian, *A New Stable High-Valent Diiron Center in R2 Mutant Y122H of E. coli Ribonucleotide Reductase Studied by High-Field EPR and ^{57}Fe ENDOR*, J. Am. Chem. Soc., 122, 9856-9857, **2000**

[3] G. Bleifuss, S. Pötsch, W. Hofbauer, A. Gräslund, W. Lubitz, G. Lassmann, and F. Lendzian, *High Field EPR at 94 GHz of Amino Acid Radicals in Ribonucleotide Reductase*, Proceedings of the Joint 29th. Ampere - 13th. Ismar International Conference, 879-880, **1998**

[4] G. Lassmann, F. Lendzian, S. Pötsch, R. Ingemarsson, L. Thelander, G. Bleifuss, A. Gräslund, and W. Lubitz, *EPR and ENDOR Study of Tryptophan Radicals in Ribonucleotide Reductase*, Proceedings of the Joint 29th. Ampere - 13th. Ismar International Conference, 816-817, **1998**

[5] G. Lassmann, F. Lendzian, S. Pötsch, G. Bleifuss, W. Hofbauer, M. Kolberg, L. Thelander, A. Gräslund, and W. Lubitz, *Structure of tryptophan radicals in mutants of protein R2 of ribonucleotide reductase studied by X-band EPR/ENDOR and by high-field EPR*, J. Inorg. Biochem., 74, 201, **1999**

[6] M. Kolberg, G. Bleifuss, B.-M. Sjöberg, A. Gräslund, W. Lubitz, F. Lendzian, and G. Lassmann, *Generation and EPR Spin Trapping Detection of Thiyl Radicals in Model Proteins and the R1 Subunit of E. coli Ribonucleotide Reductase*, submitted to Arch. Biochem. Biophys.

Konferenzbeiträge

[1] G. Bleifuss, S. Pötsch, W. Hofbauer, A. Gräslund, W. Lubitz, G. Lassmann, and F. Lendzian, *High-Field EPR at 94 GHz of Amino Acid Radicals in Ribonucleotide Reductase*, 29th. Ampere - 13th. Ismar Coference, Berlin, 1998

[2] G. Lassmann, F. Lendzian, S. Pötsch, R. Ingemarsson, L. Thelander, G. Bleifuss, A. Gräslund, and W. Lubitz, *EPR and ENDOR Study of Tryptophan Radicals in Ribonucleotide Reductase*, 29th. Ampere - 13th. Ismar Conference, Berlin, 1998

[3] F. Lendzian, G. Bleifuss, M. Kolberg, S. Pötsch, A. Gräslund, W. Lubitz, G. Lassmann, *A new Stable Paramagnetic State of the Di-Iron center in Mutant Y122H Ribonucleotide Reductase R2 of E. coli Studied by high-Field EPR and ^{57}Fe ENDOR*, 5th. EUROBIC Toulouse, 2000

[4] G. Bleifuss, S. Pötsch, M. Kolberg, D. Logan, W. Hofbauer, A. Gräslund, W. Lubitz, G. Lassmann, and F. Lendzian, *High-Field EPR Studies of Stable Diiron Center in a Single Crystal of the Mutant R2-Y122H of E. coli Ribonucleotide Reductase*, Conference on Desoxyribonucleotide Synthesis, Engeltofta, Sweden 2000

Contents

Chapter 1

Introduction to Ribonucleotide Reductase

1.1 Biological Role of RNR: Structure and Function

The conversion of ribonucleotides to deoxyribonuleotides is an essential and also rate limiting step in the synthesis of DNA, the carrier of the genetic information of almost any living organism. During this conversion the 2'-OH group in the ribose of the ribonucleotide is replaced by a hydrogen. The reaction is catalyzed by ribonucleotide reductase which is capable of turning all four types of ribonucleotides into their deoxyribonucleotide counterparts. The ribonucleotide reductase in different organisms can be devided into three classes [1]. All have in common that they consist of a protein unit, which contains the active site responsible for substrate binding and at least one site for allosteric effectors necessary for controlling the activity of the enzyme, and, additionally, a cofactor carrying a metal center. This cofactor also consists of a protein subunit in the case of class I RNR.

This work exclusively deals with two types of ribonucleotide reductase, the enzymes from *Echerischia coli* and mouse. Both belong to class Ia and possess essentially the same features:

- Both enzymes consist of two protein subunits.
- The subunit called R1 carries the active center.
- The cofactor subunit R2 carries a di-iron center and a tyrosyl radical.

Both subunits of *E. coli* and mouse RNR are homodimers: They consist of two identical polypeptide chains. The structure of the cofactor subunit R2 has been

determined in the case of *E. coli* with a resolution of 2.2 Å by X-ray crystallography [10]. For the mouse protein the structure has been determined with a resolution of 2.3 Å [11]. The structure of *E. coli* subunit R1 carrying the active center is known up to a resolution of 2.5 Å[12]. The subunits together are assumed to form a $\alpha_2\beta_2$ complex.

1.2 The Subunit R1

Both polypeptide chains of the *E. coli* protein R1 consist of 761 amino acids and possess a molecular weight of 85.7 kDa. They contain [2]

- a binding site for the substrates (active center),
- two different allosteric sites for regulators of the activity and substrate specifity.

A scheme for the reduction process of the substrates has been proposed by J. Stubbe and coworkers [15]: The first step consists of the abstraction of a hydrogen at the 3' position of the substrate by a postulated thiyl radical at Cys439. Subsequently or, according to theoretical studies [16] simultanuously, a water derived from the 2' hydroxyl group and a thiol hydrogen is leaving the binding site and the intermediate α keto radical at the substrate oxidizes the thiols at Cys225 and Cys462 to a disulfide. A thereby generated 3'-deoxynucleotide radical reproduces the thiyl radical at Cys439 by abstracting the hydrogen atom from the SH group and terminates the reduction process. The thiol groups at Cys225 and Cys462 in the active center are regenerated by thioredoxin and glutaredoxin after each turnover. Since the proposal of this reaction model, a lot of research work consisting of biochemical investigations, application of inhibitors and site directed mutagenesis in order to stop the turnover at an intermediate step [17] and also theoretical computing [20, 21] has been done. These studies support the model very well.

1.3 The Subunit R2 and the Di-iron Center

The two equal polypeptide chains of *E. coli* R2 consist of 375 amino acid residues, each of 43.4 kDa. They contain more than 70 % α-helices. Together, they form a heart shaped structure (see Figure 1.1).

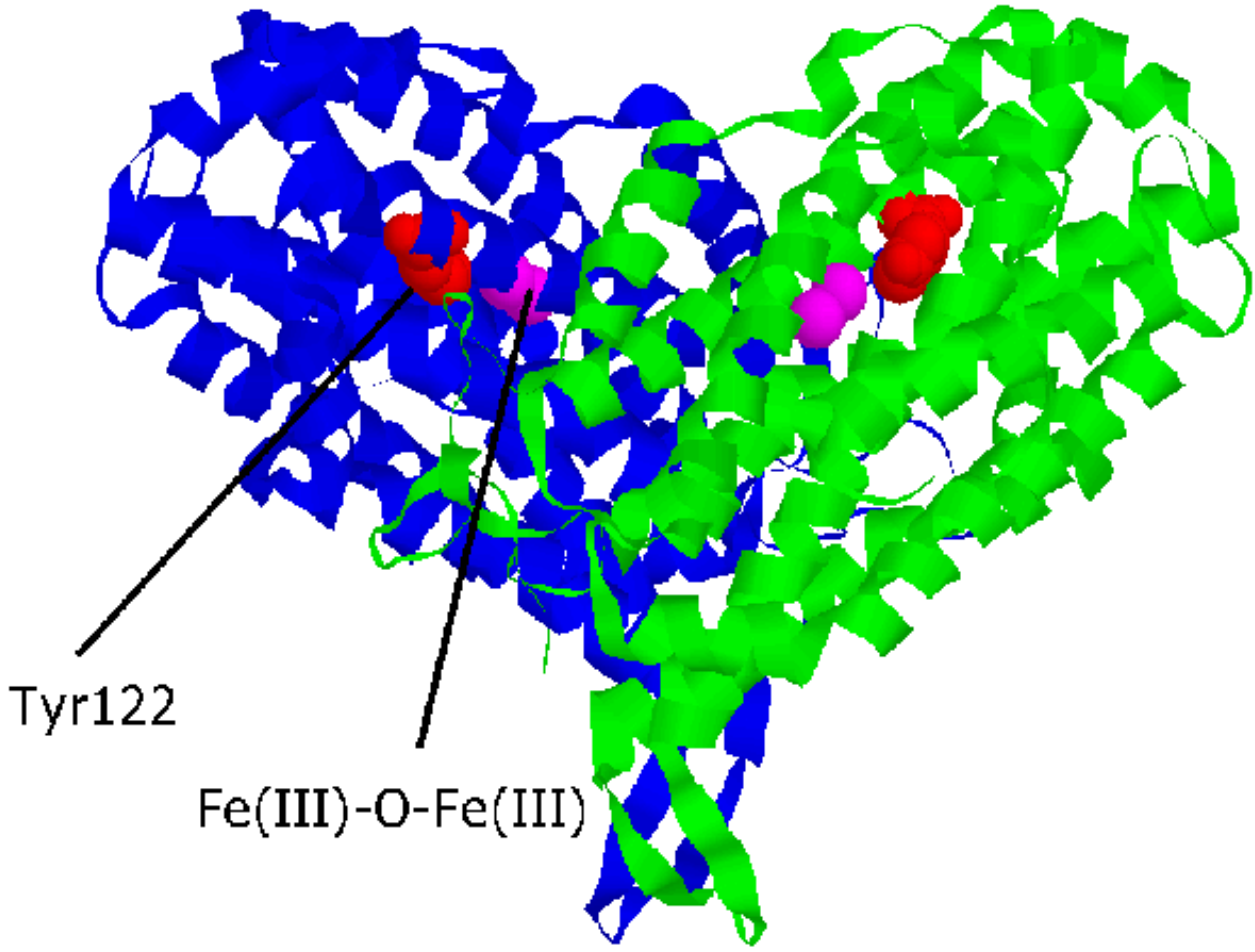

Figure 1.1: *Subunit R2 of E. coli Ribonucleotide Reductase. The position of the iron center and the tyrosine radical is indicated.*

Each chain carries a diferric iron center and a tyrosyl radical at Y122 lying in a pocket about 10 Å from the surface of the protein and 5.3 Å from the di-iron center. The tyrosyl radical is stabilized by its surrounding of hydrophobic amino acid residues [10, 22]. It exhibits a life time of approximately 2 days at room temperature in *E. coli* [10, 22]. In the mouse protein the tyrosyl radical is much less stable than in *E. coli* due to differences in its surrounding; it decays with a time constant of 10 minutes [23] at room temperature. The iron complex plays an important role in generating the tyrosyl radical during the activation reaction of the protein. In its active form the iron complex Fe(III)-O-Fe(III) consists of two ferric irons, both of which are in the high spin state : $S_1 = S_2 = 5/2$. The spins are antiferromagnetically coupled to a S=0 ground state.

Each of the six-coordinated irons (see Figure 1.2) is ligated by a histidine, a bridging glutamate and a water molecule and the complex is connected via a μ-oxo bridge, which mediates the strong antiferromagnetic coupling between the two irons [28] and is derived from dioxygen during the reconstitution reaction [29]. The other ligands are also oxygenic and contain carboxylates from Glu and Asp.

Beside its active form, the iron complex is found in several oxidation states [24]:

- The **apo-protein** contains neither the iron complex nor the tyrosyl radical. It can be generated by exposing the active form of the protein to hydroxyquinoline (chelating agent) and imidazole [29] for abstraction of the iron or by growing the cells in iron free medium [25].

- The **reduced form** carries a diferrous iron center Fe(II)Fe(II) and no tyrosyl radical. It builds when apo-protein is allowed to react with iron(II) in the absence of oxygen [26]. In the reduced state, as displayed in Figure 1.3, each iron exhibits a coordination number of four and is ligated by one histidine, one carboxylate and two bridging carboxylates connecting the two metal sites [10].

- In the **active form** of the center described above the two ferric irons Fe(III)Fe(III) are antiferromagnetically coupled and 3.3 Å separated from each other. The active form builds when the apo protein is exposed to ferrous iron (in vitro an iron ascorbate complex is used in order to stabilize the iron(II) in the presence of oxygen [29, 30]).

- In the **met form**, as shown in Figure 1.2, the ferric irons exhibit the same

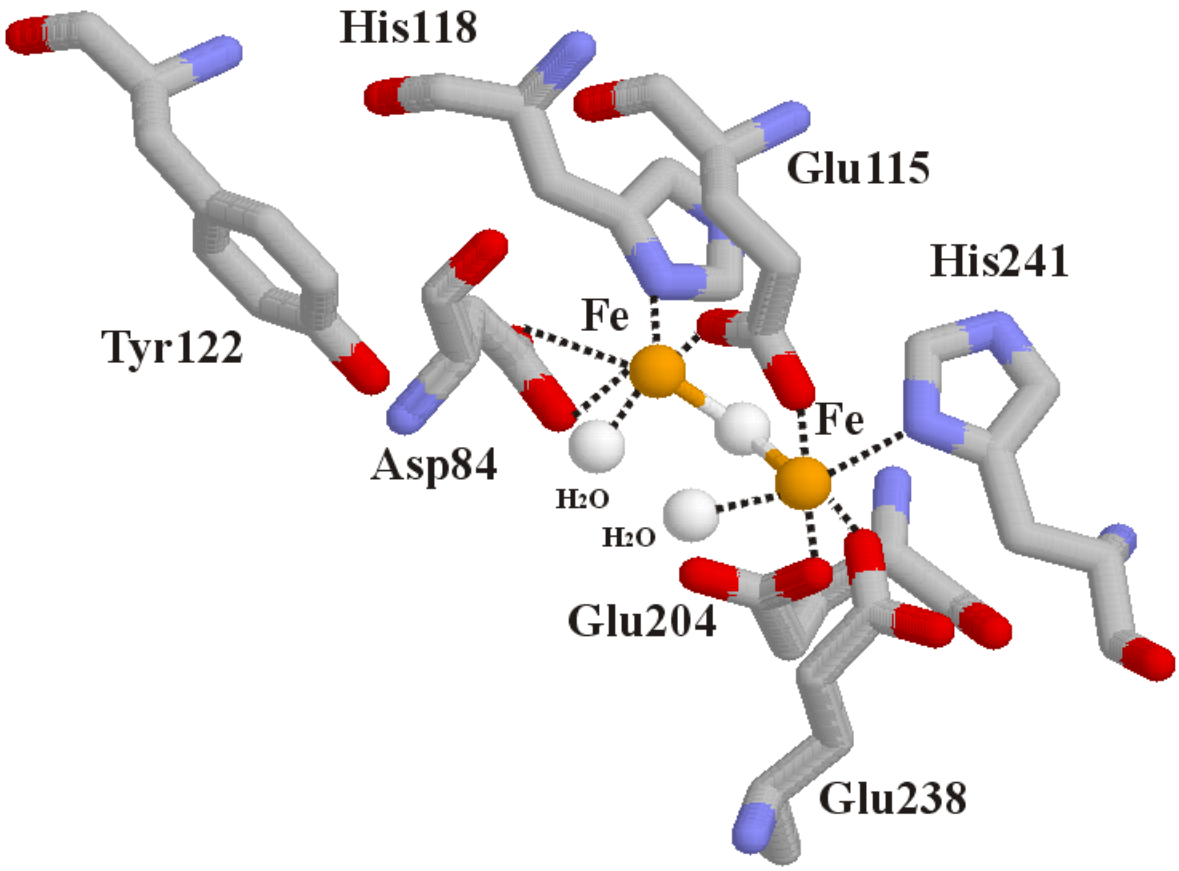

Figure 1.2: *Ligation of the di-iron center in subunit R2 of E. coli RNR (met-form: Fe(III)Fe(III)-Tyr122-OH) [74]*

ligation as in the active form, but the met form does not have the tyrosyl radical. It can be generated by reaction of the active protein with hydroxyurea, [32] which reduces the tyrosyl radical to tyrosine while leaving the iron center intact. This reaction is reversible since addition of water peroxide to the met form oxidizes Y122 again, thereby regenerating the radical [33].

- A **mixed valence intermediate Fe(III)Fe(IV) state** (intermediate X) is the precursor of the active form and occurs during the reconstitution reaction. This form is paramagnetic with S=1/2 [84].

1.3.1 The Reconstitution Reaction

During the reconstitution reaction the iron complex is built into the protein and the tyrosyl radical is generated, thus bringing the protein into its active form. The different steps of the reconstitution reaction are shown in Figure 1.3. In the reconstitution reaction apo-protein is incubated with iron(II), which is built into the protein and activated by oxygen [29]. Thereby the diferric iron complex is formed and the tyrosyl radical emerges.

First, the iron(II) is bound in the form of a diferrous cluster (reduced form) [34]. A rapid reaction with dioxygen produces a short lived intermediate believed to be a peroxo compound on the basis of a model system [36, 37], which decays to the so-called intermediate X, a Fe(III)Fe(VI) cluster which has been investigated far better than its precursor [84]. intermediate X has the capability of oxidizing the tyrosine at position Y122, thus generating the tyrosyl radical while the iron center is converted into its diferric form. The activated protein subunit R2 is now able to function as cofactor for the catalytic reduction of ribonucleotides.

1.3.2 The Radical Transfer Pathway

Radical transfer from Y122• in R2 to C439• in R1 is believed to initialize the turnover reaction in R1. Y122, however, is separated by a distance of around 35 Å from the active center in R1 as was estimated from modelling the docking of the three dimensional protein structures of the R1 and R2 subunits [12]. Therefore, a coupled electron/ proton transfer or, alternatively, hydrogen atom transfer between radical and active site has been postulated. The crystal structures reveiled a number of hydrogen bonded and fully conserved amino acid residues connecting these amino

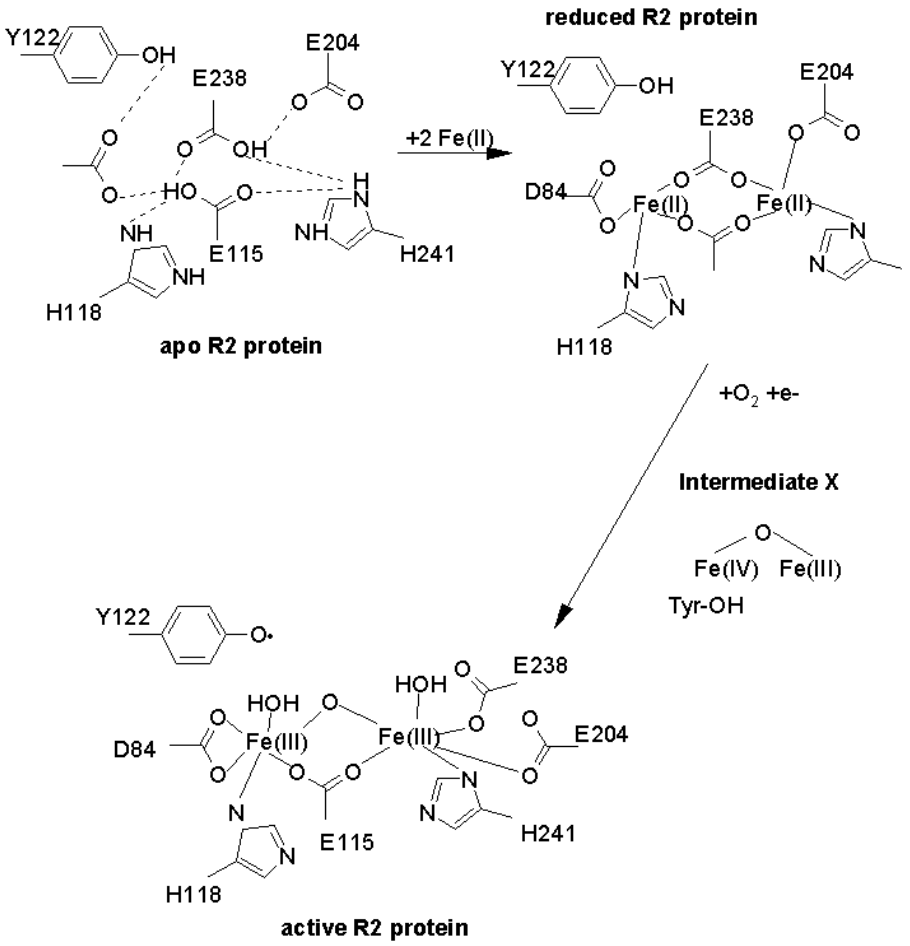

Figure 1.3: *The figure shows the chemical structure of the di-iron ligating site in protein R2 during the different steps of the reconstitution reaction. [24]*

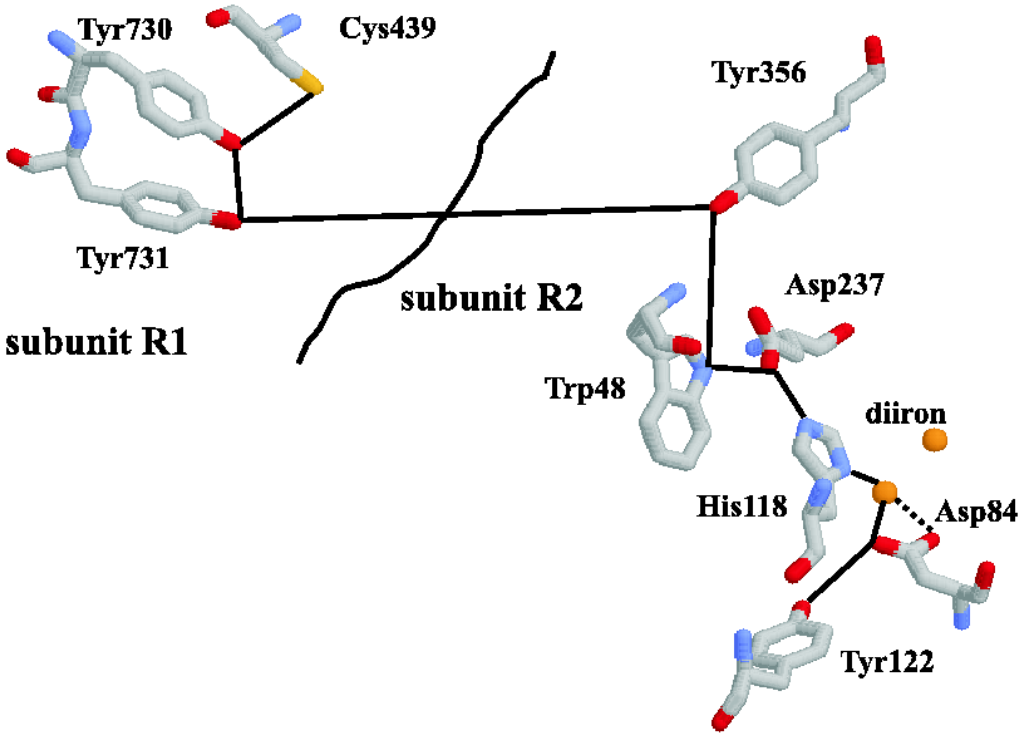

Figure 1.4: *Sketch of the radical transfer pathway from the tyrosyl radical of R2 to C439 at the active center of R1. The amino acids participating in the transfer are all connected with each other via hydrogen bridges.*

acid side chains as candidates of a possible electron transfer pathway [38]. Indeed, as some of them were substituted by site-directed mutagenesis, a severe loss of enzymatic activity was observed [40]. In R1 mutant E441Q an intermediate radical state at the active center could be detected and identified as a disulfide radical anion [66]. The putative electron transfer pathway is shown in Figure 1.4.

Theoretical studies employing quantum chemical methods indicate on the basis of energy considerations that an electron transfer from the tyrosine to the active center is highly unlikely [42]. This was supported by the fact that an ionisation of an amino acid is energetically less favorable than the charge separation in a radical pair - metal complex as it occurs for example in the electron transfer of the photosynthetic reaction center [42]. Instead, for RNR a hydrogen atom transfer model is favored which faces considerably lower energy barriers (coupled electron/proton transfer) [41].

1.3.3 Background of the Dissertation: Substitution of Y122 in *E.coli* and Y177 in Mouse RNR

The background of this dissertation are studies where Y122 in wild type R2 was replaced by other amino acids via site-directed mutagenesis [44, 53]: The reason was to find out whether other redox-active amino acids at the position of the tyrosine in *E. coli* and mouse R2 can be oxidized similarly during the reconstitution and in case it succeeds, whether they can substitute the tyrosine radical for catalytic activity [43, 44, 53, 54]. The oxygen activated intermediate di-iron state X (Fe(III)Fe(IV)) exhibits a high oxidative power. In wild type protein R2 it oxidizes the tyrosines Y122 (*E. coli*) and Y177 (mouse) to its corresponding radical. The tyrosine radicals formed are stabilized by their environment of hydrophobic amino acids. By substituting the tyrosine, it was investigated

- if intermediate X is capable of oxidizing other amino acids, such as tryptophan and cysteine, exhibiting a redox potential similar to tyrosine.
- if these amino acid radicals - in case they are formed - are stabilized in the hydrophobic pocket as well and exhibit also a long life time, and if they can take over the enzymatic function of the tyrosine radical;
- in the case of amino acids, which are hard to oxidize, such as phenylalanine or histidine, if the oxidative power of X is redirected towards other amino acid residues in the surroundings of the di-iron center
- if the life time of X, the precursor of the tyrosine radicals, changes and whether other paramagnetic states of the di-iron center occur in the mutants.

Especially tryptophan exhibits a redox potential very similar to that of tyrosine (1.05 V compared with 0.94 V for Tyr) and therefore seems to be a very promising substitute [53, 54]. A series of mutants has been created by Swedish groups at the University of Stockholm, where the redox active tyrosine is substituted by tryptophan, histidine, cysteine and phenylalanine and the corresponding plasmid was used for overexpression of *E. coli* and mouse R2 [53].

None of the investigated systems showed any enzymatic activity [53]. The only mutant where a radical at the desired position of the former tyrosine was found turned out to be Y177W [53]. In Y122F several radical species have been detected,

two of them neutral tryptophan radicals at W111 and W107 [43, 54]. In some of the mutants, however, intermediate X turned out to exhibit a much longer life time than in wild type protein, which made them appropriate mutants for rapid freeze-quench (RFQ) EPR and ENDOR studies on this EPR active iron center [53]. Extensive EPR and ENDOR investigations have taken place for the radicals detected in Y122F and Y177W [53, 54]. Here, mutant protein with indole-d_5 labelled tryptophan led to a considerably reduced line width indicating significant spin density on a tryptophan indole ring. This led to the identification of the trapped radicals as tryptophan radicals. EPR and ENDOR studies have elucidated the electronic structure of both tryptophan radicals [44, 53]. The EPR spectra revealed two large H_β couplings in the case of W111• in Y122F and one large coupling for W177• in Y177W. The H_β coupling strength yielded valuable information on the side chain orientation. This information and the saturation behaviour was used to assign the radicals to W177 and W111, respectively [53, 54]. Both radicals exhibit largely anisotropic ^{14}N couplings, which are typical for tryptophan radicals which was recently confirmed by a theoretical study [99]. ENDOR studies furtheron resolved several proton couplings assigned to ring α-hydrogens thus making it possible to determine the spin density distribution on the indole ring experimentally for a tryptophan radical. Hereby H_2O/D_2O exchange was employed [44]. It could be shown that both tryptophan radicals are in a neutral state [44]. A very stable paramagnetic species (so-called center H) was found in mutant R2-Y122H. Dr. S. Pötsch observed a singlet Gaussian EPR line at X-band in R2-Y122H. Neither the g-tensor nor hyperfine couplings were resolved.

1.3.4 Objective of this Dissertation

The present dissertation continues the spectroscopic studies of R2 mutants at the state described above, in order to characterize the electronic structure of paramagnetic centers in R2 protein in detail using advanced EPR and ENDOR spectroscopy. Subject of the studies are protein-associated tryptophan radicals in Y122F and Y177W and a paramagnetic metal center in R2-Y122H.

The first part of this work describes the high field EPR characterization and identification of the tryptophan radicals W177• and W111• introduced in the last section. A discrimination between tryptophan and tyrosine radicals based on their

characteristic g-anisotropy is proposed: In previous high field EPR investigations on tyrosine radicals it was shown that the spectrum is dominated by a well resolved characteristic g-tensor [51]. Tryptophan radicals are expected to exhibit a different g-anisotropy. In the previous investigations at X-band frequency the spectra for both radical types are dominated by the large H_β couplings. Only isotope labelling led to their identification. It will be shown, that the identification of tryptophan radicals is much easier at high field EPR. The effect of hydrogen bonding on the g-tensor and side chain geometry on the H_β couplings will be discussed as well.

In the second part the paramagnetic center H detected in mutant R2-Y122H is analyzed in collaboration with Matthias Kolberg. Matthias Kolberg was responsible for the biochemical part of the investigation, which included protein preparation, ^{57}Fe substitution and the investigation of the redox behaviour of center H. The part of the investigation presented in this work will be mainly the spectroscopic characterization of the center.

The identification of center H includes

- the determination of the g-tensor with high field EPR.
- the resolution of two ^{57}Fe hfs-tensors by CW- and pulsed ENDOR.
- the analysis of the nitrogen hfs-couplings using CW- and pulsed ENDOR.
- the determination of the orientation of the g-tensor in the molecular frame using high-field EPR at 94 GHz on single crystals of R2-Y122H containing the center H.

The aim is a complete analysis of the type of paramagnetic species of center H in R2-Y122H including its electronic structure. Comparison with similar paramagnetic di-iron centers such as intermediate X is given and a model for center H will be presented at the end of this work.

Chapter 2

Background of EPR Techniques

2.1 Electron Paramagnetic Resonance

An unpaired electron spin $\vec{\mathbf{S}}$ interacts with a static magnetic field $\vec{B_0}$ via the Zeeman Hamiltonian

$$H = \beta \vec{\mathbf{S}} \mathbf{g} \vec{B_0},$$

where $\mathbf{g}$ denotes the g-tensor and β the Bohr magneton. H is responsible for splitting up the degenerate spin up and spin down state by an energy difference, which lies in the GHz domain for a static field of around 300 mT. Due to the Boltzmann law these energy levels exhibit a slight population difference which depends upon temperature. When an oscillating magnetic field is created at the site of the sample via microwave irradiation, transitions between these energy levels are induced, if the resonance condition

$$\omega = \frac{\beta}{h} g B_0 \tag{2.1}$$

is fulfilled [55]. Owing to the population difference microwave power is effectively absorbed from the field which can be detected as an EPR signal. The so-called g-factor takes up the value

$$g_e = 2.00231930386$$

in the ideal case of a free electron [56]. Usually, however, g differs from this value and often becomes anisotropic due to the contribution of other Hamiltonian terms, for example the spin orbit coupling term, which lead according to first order perturbation theory to a mixing of excited states to the ground state. In the case of organic radicals this effect remains small and the g-value only becomes slightly higher compared with a free electron, whereas for paramagnetic centers in metals

the deviation can become considerable and values below the free electron value are often observed. Therefore the g values are a fingerprint of the electronic environment of the unpaired spin. In the anisotropic case g becomes a tensor, which in its eigensystem is diagonal and described by its principal values g_x, g_y and g_z (in the axial case two of the principal values are identical) [57]. In a crystal, the EPR signal then exhibits a orientation dependence which, when measured as a function of the rotation angle, can yield insight into the orientation of the g-tensor eigensystem with respect to the crystal axes and thus give valuable information on the site of the paramagnetic center. The effective g-value then depends upon the orientation of the g-tensor axis system with respect to the magnetic field:

$$h\nu = g_{eff}(\theta, \phi)\beta B_0, \tag{2.2}$$

For a powder as well as a frozen solution all orientations are contributing to the spectrum, resulting in a signal shape which can be calculated by integrating the single EPR line over all possible orientations (see powder spectra in chapter 3.1). The g-factor principal values can be determined from the line shape of a powder-like spectrum, if the g-anisotropy exceeds the line width of the EPR transition. In a liquid, however, this anisotropy is averaged out by the fast rotations of the molecules and the EPR signal gets much narrower and appears at the position of the isotropic part of the g-tensor:

$$g_{iso} = \frac{1}{3}Tr(\mathbf{g}), \tag{2.3}$$

where Tr denotes the trace of $\mathbf{g}$. For more viscous liquids and for larger molecules as for example proteins where the correlation time of the molecular rotation gets larger, finally immobilization takes place and the spectra become more and more powder-like [57].

2.2 Hyperfine Interaction

The interaction of the electron spin with a nuclear spin I leads to a further splitting of the energy level as pictured in Figure 2.1.

This interaction is included into the Hamiltonian via a hyperfine coupling constant $\mathbf{A}$:

$$H = \beta_e \vec{B_0}\mathbf{g}\vec{S} - g_n\beta_n\vec{B_0}\vec{I} + \vec{S}\mathbf{A}\vec{I} \tag{2.4}$$

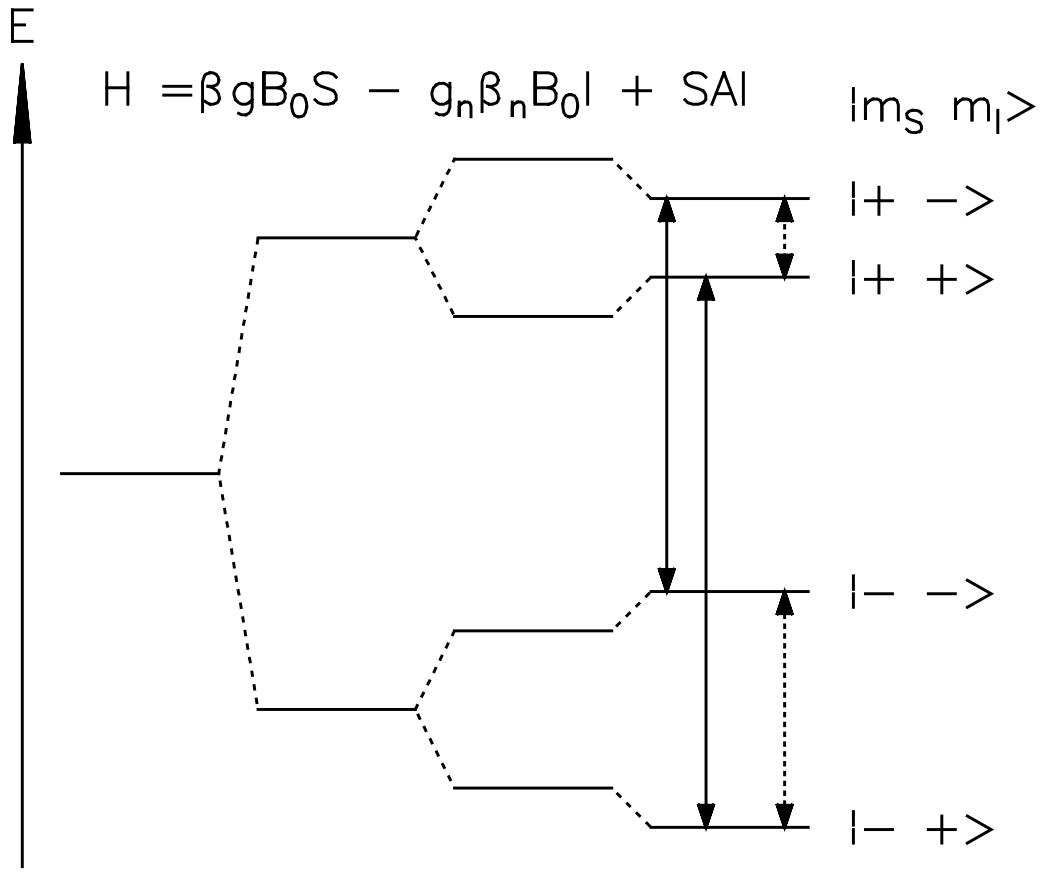

Figure 2.1: *Energy splittings due to the different terms in the spin Hamiltonian; The allowed ESR and NMR (dashed) transitions are marked.*

where the second term describes the nuclear Zeeman interaction (β_n is the nuclear magneton, which corresponds to the Bohr magneton β_e for electrons), which has no effect on the continuous wave (CW) ESR spectra. The hyperfine coupling tensor **A** can be split into two parts [58]:

- The isotropic part of the hyperfine interaction due to the Fermi contact term

$$A_{iso} = \frac{2}{3}\mu_0 g\beta_e g_n\beta_n \mid \psi(0) \mid^2 \tag{2.5}$$

  only effects electrons with s-orbital character, which have a finite probability density $\mid \psi(0) \mid^2$ at the site of the nucleus.

- A magnetic dipolar interaction between electron and nuclear spin

$$H = -\frac{\mu_0}{4\pi} g\beta_e g_n\beta_n (\frac{3(\vec{\mathbf{I}}\vec{r})(\vec{\mathbf{S}}\vec{r})}{r^5} - \frac{\vec{\mathbf{I}}\vec{\mathbf{S}}}{r^3}) \tag{2.6}$$

  contributes as the anisotropic part of the hyperfine interaction tensor.

The isotropic part A_{iso} can be calculated for the tensor **A**:

$$A_{iso} = \frac{1}{3} Tr(\mathbf{A})$$

When the hyperfine coupling A is larger than the natural line width Γ of the EPR line a splitting of the singlet line into

$$\prod_k (2n_k I_k + 1)$$

distinct lines (n = number of equivalent nuclei, I = nuclear spin, the product with index k is over all inequivalent nuclei), each separated by A, will occur as becomes evident when the eigenvalues of the Hamiltonian to first order perturbation theory are determined (for the case of I=1/2 and isotropic interactions):

$$\Delta E = g\beta B \pm \sum_{nuclei} \frac{A_i}{2} \tag{2.7}$$

If the line width exceeds the hyperfine coupling strength the hyperfine splitting is unresolved and the spectrum consists of a singlet line of Lorentzian shape:

$$f(\nu) = \frac{1}{\pi} \frac{\Gamma^2}{(\nu - \nu_{res})^2 + 2\Gamma^2} \tag{2.8}$$

In the opposite case, when many couplings of different nuclei contribute, the coupling will cause a inhomogeneous broadening of the line. Many unresolved hyperfine

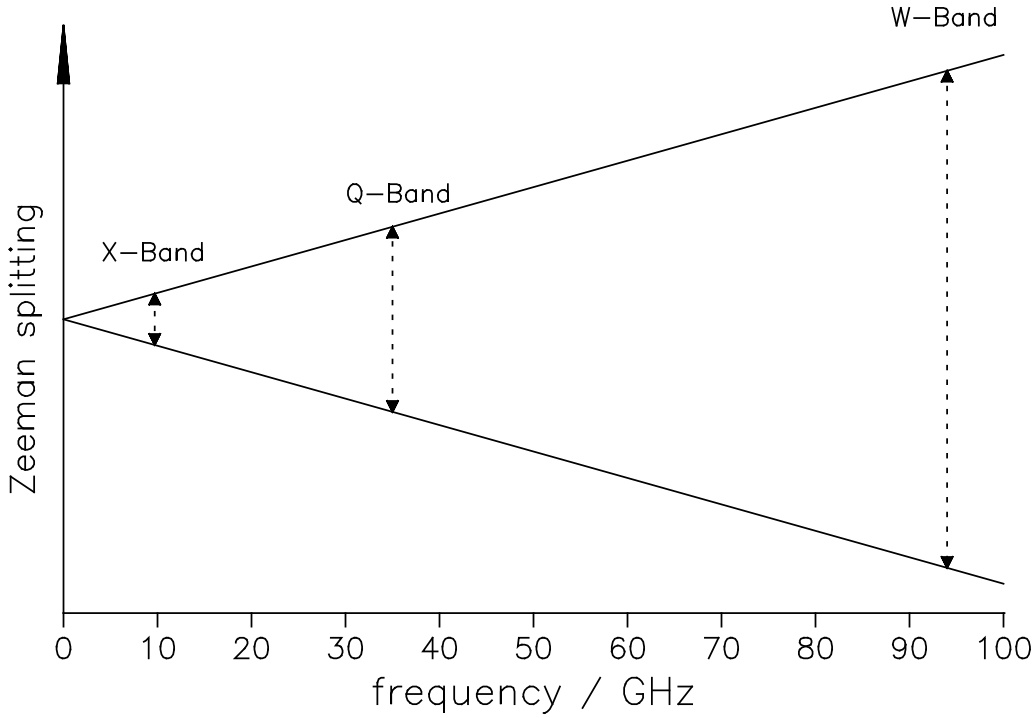

Figure 2.2: *The Zeeman splitting as function of the microwave frequency. The microwave bands used in this work are marked*

couplings thus give the absorptive ESR line a Gaussian shape:

$$f(\nu) = \frac{1}{\sqrt{2\pi}\Gamma} e^{-\frac{(\nu-\nu_{res})^2}{2\Gamma^2}} \tag{2.9}$$

By the method of ENDOR spectroscopy many of the couplings obscured in a broad line width can be resolved.

2.3 Frequency Bands

Taking another look at the spin Hamiltonian 2.4 it becomes clear that the energy difference imposed by the Zeeman interaction scales with the external magnetic field whereas the splitting or line broadening due to a hyperfine interaction does not. Going to higher frequency bands, and thus higher magnetic fields, it is possible to resolve a g-tensor anisotropy otherwise obscured under a inhomogeneously broadened EPR line at low frequency bands. Going from X-band to W-band stretches the g anisotropy by a factor of 10. The behaviour of the Zeeman energy splitting at several frequently used bands, also in this work, is pictured in Figure 2.2.

High field EPR at 94 GHz was employed several times during this work to resolve

a g-tensor at 94 GHz W-band frequency which was completely hidden under a Gaussian line shape at 9.7 GHz in X-band. Therefore, the major advantage of EPR at higher frequency bands compared with X-band lies in the larger resolution of the g-tensor anistropy. Measurements at different frequency bands are therefore an effective probe of

- the g-tensor anisotropy
- a discrimination between different mechanisms responsible for line broadening: mechanisms due to hyperfine interaction or others caused by the electron Zeeman term like g-anisotropy or g-strain [59].

In this work the technique is applied sucessfully to different paramagnetic centers found in wild type and mutant R2 protein of mouse and *E. coli*:

- The increased resolution of the g-anisotropy compared with X-band permits the discrimination between different amino acid radical species solely due to their characteristic g-tensor anistropy without further need of isotope labelling. This is shown for the case of tyrosine and tryptophan radicals in wildtype and mutant R2.
- In case of the paramagnetic center H in mutant R2-Y122H the g-tensor principal values - which are unresolved at 9.4 GHz - are determined and compared with the well known values for similar paramagnetic species.
- Measurements at 94 GHz make it possible to detect the angular dependence of the g-anisotropy in the case of R2-Y122H crystals and yield the orientation of the g-tensor axis system in the molecule when the EPR rotation pattern are set into correlation with the information from the X-ray crystal structure.

Further advantages of the measurements at higher frequency bands worth mentioning are the small quantities of material needed for the samples due to the smaller cavity dimensions and the at the same time higher transition probability. This makes it possible to receive a reasonable signal-to-noise ratio, for example, for crystals with sizes in the submillimeter regime, as they are used for X-ray experiments.

2.4 Saturation and Relaxation

A spin system which undergoes transitions in a microwave field returns to equilibrium after the microwave field is turned off via interactions with neighboring spins and with phonons in the lattice. The interactions with neighboring spins lead to a dephasing and therefore a loss of coherence. Effectively no energy is transferred to or from the spin system. The relaxation is described by a time constant T_2, the spin-spin relaxation time. The lattice interactions lead to a energy transfer between the spins and the lattice. It is described by T_1, the spin-lattice relaxation time. Due to the spin-lattice relaxation the spins are achieving thermal equilibrium according to the Boltzmann law and the population difference between the spin energy levels is reestablished. The relaxation processes are also important in the case of continuous microwave irradiation: When the microwave power becomes high enough, so that the relaxation is slow compared with the transition rate, finally an equal population of the spin energy levels will occur. In this case effectively no power is absorbed anymore from the microwave field: The signal is saturated. There is a relationship between the microwave power, where the saturation begins to occur and the relaxation times inherent to the spin system. In the non-saturating domain the square of the double integral over the intensity I of a derivative signal is proportional to the microwave power irradiated. If the line width does not change, one can write this as:

$$I \sim \sqrt{P}$$

As the line is saturating the signal intensity does not grow as fast as $\sqrt{P}$ anymore and finally decreases. The power, where the quotient out of I and $\sqrt{P}$ has been reduced to one half of its non-saturating value, is called half saturation power $P_{\frac{1}{2}}$. The saturation curve usually obeys the empirical law [59]:

$$\frac{I}{\sqrt{P}} = \left(\frac{1}{1+\frac{P}{P_{\frac{1}{2}}}}\right)^{\frac{b}{2}}$$

where $b = 1$ in case of a inhomogeneous line broadening and $b = 2$ for a homogeneously broadened line. The microwave field B_1 at the half saturation power depends upon the relaxation times T_1 and T_2 [59]:

$$B_1 = \frac{2}{\gamma}\sqrt{\frac{1}{T_1 T_2}}, \tag{2.10}$$

where γ is the magnetogyric ratio. There are different relaxation mechanisms contributing to T_1 and T_2. For indirect relaxation, as for example Orbach processes, low lying excited states are involved: Hereby the relaxation path to the ground level goes through an excited state. Such processes become important in temperature domains, where enough phonons of the appropriate energy are present [59]. Low lying excited states are particularly found in metal centers, for example the higher spin states $S = 3/2, 5/2...$ in the $S = 1/2$ - ground state di-iron center intermediate X in R2 (introduced in chapter 1). This is one reason why paramagnetic metal centers are often relaxing much faster than organic radicals and are saturating at much higher microwave power levels (see center H and Y122• in chapter 4.2).

2.5 ENDOR Spectroscopy

In a Continuous Wave ENDOR experiment nuclear spin transitions are observed via the intensity change of partially saturated EPR transition. The higher resolution of NMR is here combined with the higher intensity of the EPR. Whereas in CW-EPR $\prod_k(2n_kI_k + 1)$ lines contribute which can be obscured under an inhomogeneously broadened Gaussian line shape, in ENDOR only $2 \cdot m$ lines are seen at the same conditions (m denotes the number of inequivalent nuclei). During an ENDOR experiment an EPR transition (path $1 \rightarrow 3$ in Figure 2.3) is driven at resonance and partially saturated while simultanously a variable rf field is irradiated. If the radio frequency (rf) field is in resonance with a nuclear transition, the respective relaxation path (path $1 \rightarrow 2$ in 2.3) is short circuited. This leads to a change in the contribution of the different relaxation path ways connecting level 1 and level 3 (see 2.3). The pumped EPR level 1 gets depopulated, leading to an increase of the power absorption from the microwave field which is detected as the ENDOR signal. The intensity of the ENDOR signal is limited by all electron and nuclear relaxation rates involved. It is only a few percent of the intensity of the corresponding EPR transition (see spectra in chapter 3). In an typical ENDOR experiment the intensity of the EPR line is observed as a function of the rf frequency [60].

The ENDOR signal thereby depends crucially upon the relaxation rates W_{12}, W_{13}, W_{24}, W_{34} of the electron and nuclear transitions and the cross relaxation rates W_{14}, W_{23}. An important conclusion of this fact is, that ENDOR intensities do not reflect nuclear multiplicities. Therefore the double integral of an ENDOR transition

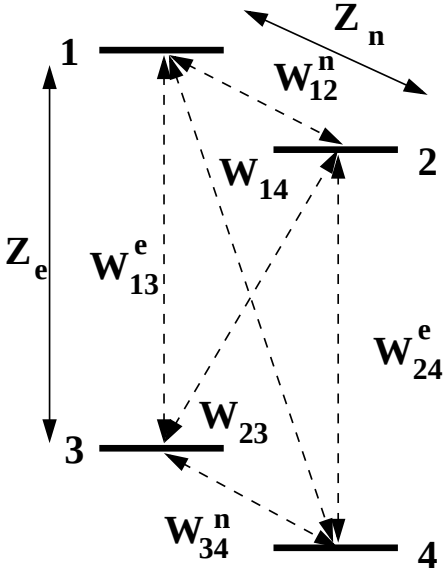

Figure 2.3: *The ENDOR relaxation paths: The relaxation paths with rates $W_{12}, W_{13}, W_{24}, W_{34}$ and the cross relaxation paths W_{14}, W_{23} are drawn by dashed lines and the induced EPR (Z_e) and NMR (Z_n) transitions by solid lines.*

generally is not proportional to the quantity of nuclear spins, which contribute to the signal. The resonance condition for an ENDOR transition is calculated employing the nuclear Hamiltonian:

$$H = g_n \mu_n B_0 I + S\mathbf{A}I \tag{2.11}$$

In the simplest case of first order perturbation theory and just one isotropic hyperfine interaction two lines are observed: In the case of A being smaller than the Zeeman resonance frequency ENDOR resonances occur symmetrically around the point of the pure nuclear Zeeman transition separated by A, while, if A exceeds the Zeeman frequency, the lines are separated by twice the Zeeman frequency and appear symmetrically around $\frac{A}{2}$:

$$\nu_{ENDOR} = |\nu_n \pm \frac{A}{2}| \tag{2.12}$$

The nuclear Zeeman term depends on the nuclear g-value which has characteristic values for different types of nuclei allowing one to discriminate for different nuclei in the ENDOR spectra. In the Table 2.1 g-factors for nuclear transitions used in this work in ENDOR measurements are displayed together with their Zeeman resonance frequency ν_n at X-band conditions ($B_0 = 3400$ G).

The Zeeman splitting term scales with B_0 in contrast to the hyperfine coupling term in the Hamiltonian. By taking ENDOR spectra at different microwave

g_n **and nuclear Zeeman transition frequency for the most frequently used ENDOR nuclei**			
nucleus	spin	g_n	ν_n (MHz) at 3300 G
^1H	1/2	5.5857	14.05
^2H	1	0.8574	2.16
^{14}N	1	0.4038	1.02
^{15}N	1/2	-0.5664	1.42
^{57}Fe	1/2	0.1806	0.45

Table 2.1: *g_n and nuclear Zeeman transition frequency for the ENDOR nuclei used in this work*

frequencies, and thus resonance fields, one can therefore discriminate between a nucleus with large Zeeman term and small hyperfine coupling, and the opposite case since only for the first case the symmetry point of the ENDOR lines will vary with the micro wave frequency (see example in chapter 3.4 where transitions are assigned to nitrogen and hydrogen nuclei by this method).

It should, however, be mentioned that the assumption of the hyperfine interaction being independent of the external magnetic field remains only valid up to first order perturbation theory. The higher order terms show a clear field dependence and become important at low magnetic fields.
When a nucleus with anisotropic hyperfine coupling is measured in frozen solution a powder average over all orientations is received as ENDOR spectrum if the pumped ESR transition effects all orientations. In the case of a pronounced g anisotropy only the contributions from the orientations also contributing to the ESR signal at the chosen resonance field are measured. Owing to this effect one can get information on the orientation of the A-tensor with respect to the g-tensor principal axes by measuring ENDOR spectra at different points on the envelope of the ESR line (orientation selective ENDOR). The resonance condition now depends upon the polar and azimutal angles with respect to the g-tensor principal axes and has to be integrated over all orientations contributing to the spectrum [63].

2.6 Pulsed EPR Methods

While in CW-EPR the microwave is irradiated continuously and the signal is detected via the absorption of microwave power by the sample, the methods discussed in this section employ short pulses of high power microwave radiation creating a strong magnetic field $\vec{B_1}$ at the position of the sample. The electron spin magnetization of the macroscopic sample $\vec{M}$ due to the population difference produced by the static magnetic field $\vec{B_0}$ is turning around $\vec{B_1}$ during the pulse duration τ at a frequency $\omega = \gamma_e B_1$, where γ_e denotes the gyromagnetic ratio of the electron spin. The turning angle ϕ is proportional to the effective strength of the B_1 field and the pulse length τ:

$$\phi = \gamma_e B_1 \tau$$

In a spin echo pulse sequence transversal (perpendicular to $\vec{B_0}$) magnetization is created by a $\frac{\pi}{2}$ pulse ($\phi = 90^o$). After a time T letting the spins dephase in the transversal plane, a π-pulse is employed for effectively inverting the effects of the spin dephasing. The spins become coherent again at a time $2T$ after the initial pulse, which is detected as a spin echo signal. Another frequently applied spin echo pulse sequence makes use of three $\frac{\pi}{2}$ pulses creating a so-called stimulated echo [64]. The height of the spinecho as a function of the pulse separation time between the second and third pulse decays due to T_1 rather than T_2 as is the case during the delay between the pulses in a $\frac{\pi}{2}$-π pulse pattern.

2.6.1 Field-Swept Electron Spin Echo Spectroscopy (ESE)

The measurement of the echo intensity for a given pulse sequence and separation time T as a function of the magnetic field strength $\vec{B_0}$ represents an alternative method of acquiring an EPR spectrum. The resonance signal is detected in the absorption mode. Hereby, the signal is detected via an integration over the spin echo as a function of the magnetic field B_0. The integration interval t has to fulfill the condition $t > \frac{2\pi}{\Delta\omega}$, where $\Delta\omega \sim \frac{1}{pulselength}$ giving the width of the part of the EPR spectrum being resolved by the used pulses [69]. The advantage here is that even very broad lines, unobservable by applying the usual Continuous Wave method can often be resolved. Furtheron the method is employed for filtering out unwanted signals which is possible if they exhibit a different relaxation behaviour. By carefully

choosing the appropriate pulse sequence and pulse separation times one can suppress fast relaxing species [66].

2.6.2 Pulsed ENDOR Spectroscopy

In pulsed ENDOR spectroscopy nuclear transitions are detected via their effect on the spin echo intensity at a field point on the EPR line envelope. Two different pulse sequences, the so-called Mims and Davies ENDOR, are applied frequently. Both are pictured in Figure 2.4. In a Davies ENDOR experiment first the polarization of an EPR transition is inverted by a selective 180^o pulse (so-called preparation pulse). An rf pulse, for which the frequency is varied continuously during one sweep, shifts spin packets within the EPR line, if it is in resonance with a nuclear transition. The last two pulses, a $\frac{\pi}{2} - \pi$ sequence, create a spin echo and thereby serve as detection pulses of the remaining polarization. The intensity of an integration window over the echo is measured as a function of the rf frequency. For the Davies pulse sequence one usually chooses rather long microwave pulses thus exciting a - compared with the width of the EPR spectrum - narrow resonant bandwidth $\Delta\omega$ in the frequency domain:

$$\tau_{MWpulse} = \frac{1}{\Delta\omega}$$

The Davies ENDOR effect can be explained as follows [67]: The preparation pulse inverts the electron polarization in a narrow region within the inhomogenously broadened EPR transition in the frequency domain. The width of this region can be adjusted via the preparation pulse length. Actually a hole is burnt into the electron polarization pattern, as visualized in Figure 2.5. The following rf pulse now is able to transfer polarization out of this hole by driving nuclear transitions, thereby decreasing the depth of the magnetization hole (see Figure 2.5, dashed line). The detection pulse sequence creates an echo testing the actual electron spin polarization at the magnetization hole. It is clear that the intensity of this effect and therefore the sensitivity varies with different strengths of the hyperfine coupling interaction: Very small couplings with

$$A \leq \frac{1}{\tau_{MWpulse}}$$

cannot be detected since no magnetization can be transferred within the inversion hole. On the other hand, the pulse length cannot be increased arbitrarily (which would enable the method to detect arbitrarily small hyperfine couplings) because

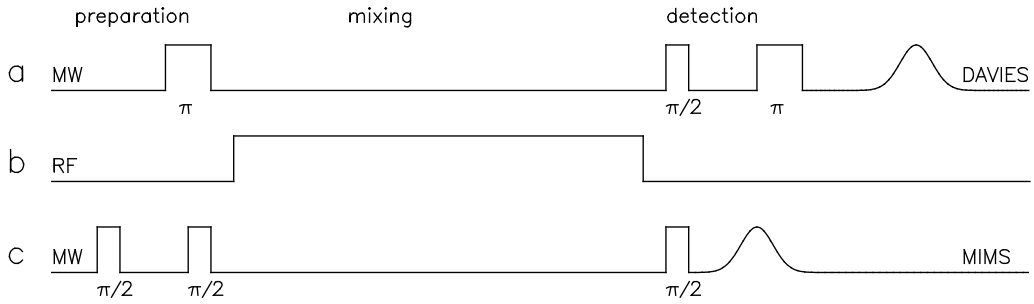

Figure 2.4: *Frequently employed pulsed ENDOR Sequences: a,b: Davies ENDOR c,b: Mims ENDOR*

this will reduce the echo height due to the dephasing of the spins during the pulse duration. The method therefore is suitable particularly if large coupling constants are to be resolved.

For usually applied pulse lengths of around 200 ns, the Davies ENDOR method is suited to detect hyperfine couplings $A > 7\,MHz$.

For the second method, the so-called Mims ENDOR, the pulse length is chosen very short in order to excite the whole bandwidth of the electron polarization. After the first two pulses, the spins are not inverted over the entire inhomogeneous EPR line since a spin packet with a dephasing frequency of $\frac{n\pi}{\tau}$ (with $n = 1, 3, 5...$) in the rotating frame will be turned back into positive polarization by the second pulse. Rather a sinusoidal magnetization pattern (see Figure 2.6) is created by the preparation pulse sequence with an encoding frequency of [67]

$$\omega_{polarization} = \frac{2\pi}{\tau}.$$

The following rf pulse is capable of moving spin packets within this polarization pattern by driving nuclear spin transitions.
One problem of the Mims ENDOR method is that it suffers from blind spots: No magnetization is transferred from one minimum (maximum) to another minimum (maximum) in the sinusodial polarization pattern. Therefore hyperfine couplings of strength:

$$A = \frac{n}{\tau}, \quad n = 1, 2, 3...$$

cannot be detected [69]. The intensity of the ENDOR response I depends upon the strength of the hyperfine coupling as [69, 70].

$$I \sim 1 - cos(2\pi A\tau).$$

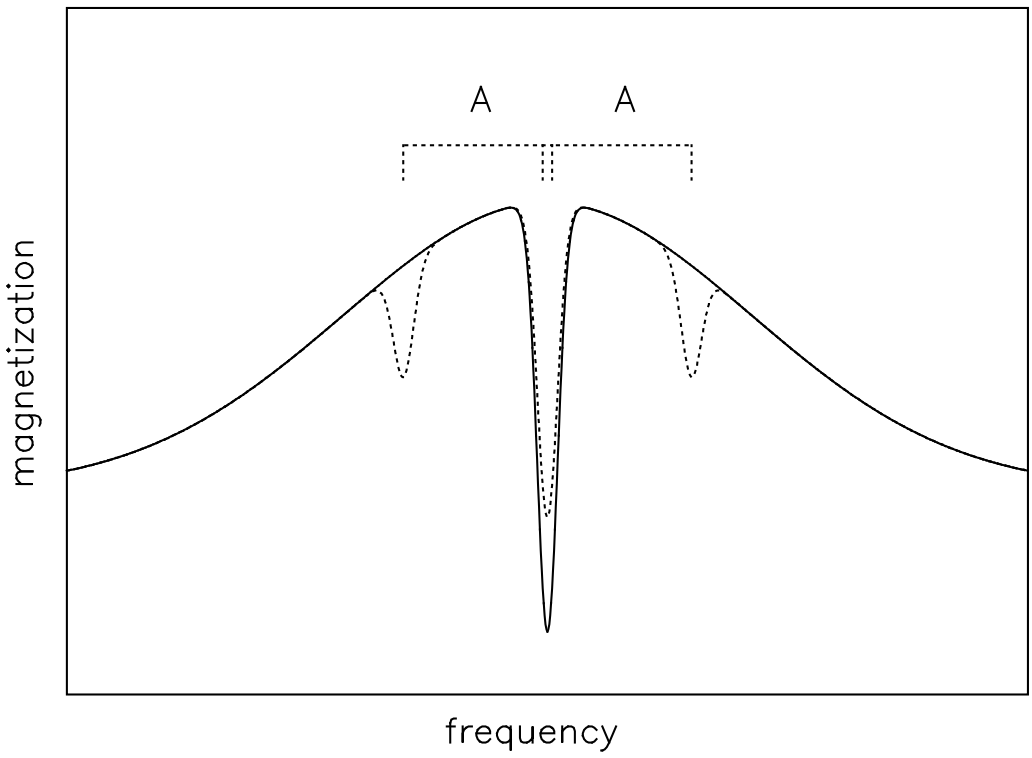

Figure 2.5: *In this figure the Davies ENDOR effect is visualized [67]: The MW preparation pulse burns a narrow hole into the EPR spectrum (continuous line). The rf pulse - if in resonance - then transfers magnetization into this hole from regions of the spectrum which - in the ideal case - were unaffected by the long preparation pulse and which lie in a distance to the hole given by the hyperfine coupling strength in frequency units (dashed line). The reduced hole depth then is detected via the 2 pulse spin echo sequence shown above.*

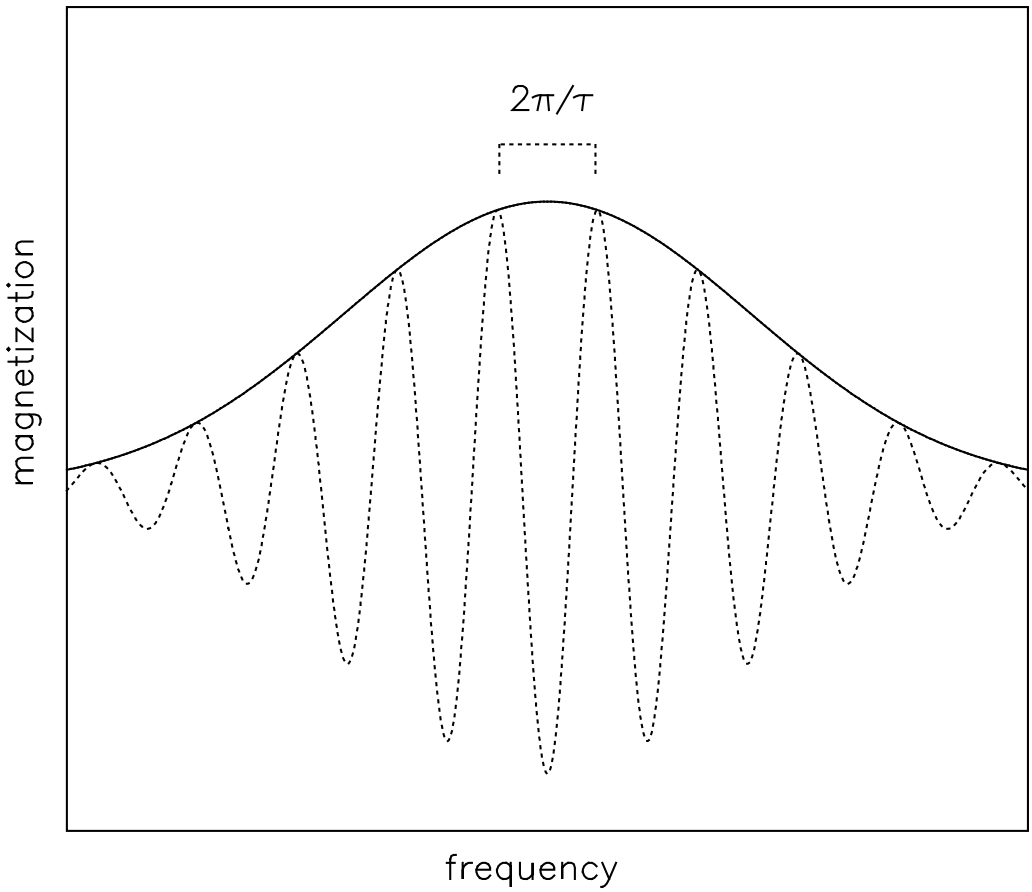

Figure 2.6: *The first two $\pi/2$ pulses in a Mims ENDOR pulse sequence create a sinusodial magnetization pattern as shown by the dashed curve. The rf pulse then is capable of transferring spin packets within this pattern if it is in resonance with a nuclear transition. [67]*

Mims ENDOR is particularly suitable for detecting weakly coupled nuclei, whose hyperfine coupling constants are small compared with $1/\tau$. For the pulsed ENDOR experiments in this work the couplings detected are larger than 7 MHz, for the ^{57}Fe ENDOR as well as the nitrogen ENDOR. Therefore a Davies pulse sequence was preferred over the Mims ENDOR method due to its advantages for the detection of large couplings and the absence of blind spots for this technique. The pulse length for a π pulse was chosen t_p=192 ns, thus exhibiting a narrow excitation band width of approximately 0.2 mT. To achieve a suitable microwave pulse power the Q-value for the pulse ENDOR cavity was adjusted to 800 by detuning into the region of overcritical coupling. This Q is low enough for the relatively long pulses employed in a Davies ENDOR sequence. The echo intensity detected via a $\pi/2 - \pi$ pulse sequence was maximized by adapting the microwave power, microwave quadrature phase and magnetic field value. The rf mixing pulse, ideally a π pulse with respect to the nuclear transitions, was set to a length of 8 μs.

For pulsed ENDOR experiments, nuclear transitions occur at the same frequencies as for common CW ENDOR experiments but are detected in the absorption mode. For the ENDOR effect in CW-ENDOR, the electronic and nuclear relaxation rates have to be in the same order of magnitude. In pulsed ENDOR, however, the MW and RF pulse lengths have to be chosen smaller than the respective electronic and nuclear spin-spin relaxation times.

2.7 EPR of Exchange Coupled Systems

2.7.1 Di-iron Proteins

In this section a comprehensive introduction into exchange coupled spin systems and their magnetic behaviour shall be given for the case of coupled di-iron centers. Non-heme di-iron bridged centers play an important role for the function of several well-known proteins. They all are capable of activating dioxygen and the metal centers can usually exist in several oxidation states [74]:

- In the hydroxylase component of methane monooxygenase (MMO) dioxygen binds at the diferrous iron site, oxidizing it to a diferric state thus initializing the turnover, which ulimatively catalyzes the oxidation of methane to methanol. The di-iron site resembles very much the one in RNR: Each iron is coordinated by a nitrogen derived from histidine, while the other ligands are oxygenic. As most important difference to RNR, MMO contains a hydroxo-bridge in contrast to a μ-oxo bridge [24, 74].
- The di-iron site in hemerythrin, an oxygen carrier protein, binds dioxygen in the form of a peroxide, converting the metal center to a diferric state. Five histidines are coordinated to the two irons in contrast to two in RNR and MMO [74].
- The iron center in the R2 subunit of RNR is essential for the formation of the tyrosine radical in the active enzyme. It has already been described in chapter one.

Other proteins belonging to this group are purple acid phosphatase, ruberythrin, stearolacyl carrier protein, Δ_9 Desaturase and Ferritin [74]. In many cases mixed valence species are occuring either as intermediates during the reaction with oxygen or can be generated through γ-irradiation or chemically under reducing conditions.

2.7.2 Exchange Coupled Two Spin Systems

The metal center of active R2 contains two high spin iron(III) linked by an oxygen atom. Fe(III) in a high spin state possesses five unpaired spins adding together to a $S = 5/2$ ground state for each of the two irons in the complex [75].
In paramagnetic centers consisting of more than one unpaired electron the spins

interact with each other, if they are close enough. This leads to a splitting in the spin energy levels even in zero magnetic field. In general, there are different types of interactions contributing.

First of all there is the magnetic dipolar interaction between two spins S_A and S_B:

$$H = -\frac{\mu_0}{4\pi} g_A \beta_e^2 g_B \left(\frac{3(\vec{\mathbf{S}}_\mathbf{A}\vec{r})(\vec{\mathbf{S}}_\mathbf{B}\vec{r})}{r^5} - \frac{\vec{\mathbf{S}}_\mathbf{A}\vec{\mathbf{S}}_\mathbf{B}}{r^3}\right) \tag{2.13}$$

which can be described phenomenologically by a tensor $\mathbf{D}$:

$$H = \vec{\mathbf{S}}_\mathbf{A}\mathbf{D}\vec{\mathbf{S}}_\mathbf{B} \tag{2.14}$$

The dipolar coupling shows a highly anisotropic behaviour since $\mathbf{D}$ is symmetric and traceless [76].

Secondly, and more important when regarding the di-iron cluster in active R2, there is the isotropic exchange interaction which can be described by a phenomenological Hamiltonian

$$H = -2J\vec{S}_A\vec{S}_B \tag{2.15}$$

where J is called the exchange coupling constant. This interaction is not magnetic in nature but actually emerges owing to the Pauli principle when two overlapping wavefunctions are combined antisymmetrically [55].

A large exchange term in the Hamiltonian leads to energy eigenstates carrying spin quantum numbers

$$S = |S_A - S_B|, |S_A - S_B + 1|, ..., S_A + S_B \tag{2.16}$$

which are separated energetically as expressed by the energy eigenvalues of the Hamiltonian [76]:

$$E(S) = J(S(S+1) - S_A(S_A+1) - S_B(S_B+1))$$

A negative coupling constant J favours the lowest S as ground state and thus couples the spins antiferromagnetically, while a positive J leads to a ferromagnetic interaction where the highest S state lies lowest in energy.

In the di-iron complex of R2 the μ-oxo bridge mediates a strong antiferromagnetic interaction (so-called superexchange) between the two $S = 5/2$ high spin irons [79]. The dipolar interaction is much smaller and therefore can be neglected. The result is a $S = 0$ ground state, which is not sensitive to EPR, and $S = 1, 2, 3, 4, 5$ excited states. The exchange coupling constant has been determined experimentally

applying magnetic susceptibility measurements yielding $J = -108 \pm^{25}_{20}\ cm^{-1}$ for *E. coli* [75], and by investigation of the relaxation behaviour of $Y122\bullet$ via saturation recovery yielding $-92 \pm 6\ cm^{-1}$ for *E. coli* and $-77 \pm 4\ cm^{-1}$ for mouse protein [80, 81]. In Figure 2.7 the different S-states are shown in an energy diagram and the occupation probability of these states has been plotted as a function of temperature, where the partition function

$$P(S) = \frac{(2S+1)e^{-\frac{E(S)}{kT}}}{\sum_S (2S+1)e^{-\frac{E(S)}{kT}}}$$

with the canonical sum of states in the denominator is employed [78].

The couplings of the diferrous center in reduced R2, in which the μ-oxo bridge is missing, have been determined experimentally as well, this time by magnetic circular dichroism measurements. Here, two $S = 2$ states are coupling and only a small exchange coupling constant $J = -0.5 \pm 0.1\ cm^{-1}$ has been found in contrast to a larger dipolar coupling ($D_1 = -10.0 \pm 2.0\ cm^{-1}$, $D_2 = -4.0 \pm 1.0\ cm^{-1}$ [82]). Intermediate X in R2 of RNR (see Figure 1.3) is a mixed valence state, in which high spin Fe(IV) (S=2) couples with highspin Fe(III) (S=5/2) antiferromagnetically. This leads to a $S = 1/2$ Kramers doublet ground state [78] and to $S = 3/2, 5/2...$ excited states. The ground state is therefore EPR active in contrast to the EPR silent $S = 0$ state of the diferric complex in active R2. An analogous situation is found for Fe(II)Fe(III) couples. If the dipolar coupling is small enough and can be neglected in comparison to a strong exchange coupling, the g-factor as well as the hyperfine coupling constant, either for a ligand nucleus interaction or for ^{57}Fe of these mixed valence metal center can be written as a sum of the intrinsic g or A values:

$$\mathbf{g_{eff}} = \sum_{i=A,B} c_i \mathbf{g_i} \tag{2.17}$$

and

$$\mathbf{A_{eff}} = \sum_{i=A,B} c_i \mathbf{A_i} \tag{2.18}$$

The coefficients c_i are the projections of the ground states of the coupled spins onto the substates S_A and S_B (spin projection coefficients). They can be written as a function of the total spin S and the uncoupled spins S_A and S_B [77]:

$$c_1 = \frac{S(S+1) + S_A(S_A+1) - S_B(S_B+1)}{2S(S+1)}$$

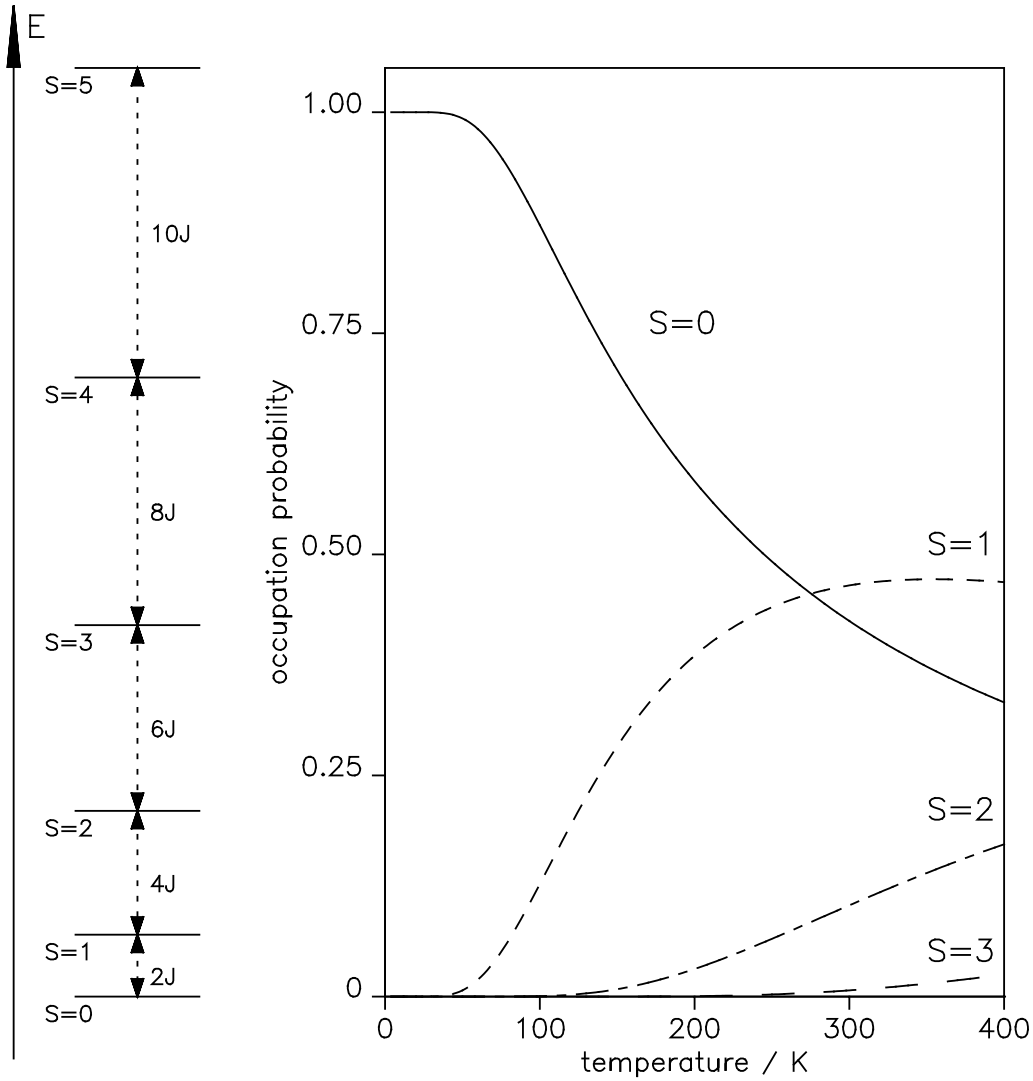

Figure 2.7: *Energy levels for an antiferromagnetically coupled diferric center (left) and the occupation probability of various spin states as a function of temperature is displayed for J=-108 cm^{-1} (as measured for the Fe(III)Fe(III) complex in R2 of RNR)(right).*

$$c_2 = \frac{S(S+1) - S_A(S_A+1) + S_B(S_B+1)}{2S(S+1)} \tag{2.19}$$

In the case of Fe(III)Fe(IV) and Fe(II)Fe(III) complexes formula 2.17 and 2.18 then become

$$\mathbf{g} = \frac{7}{3}\mathbf{g}_A - \frac{4}{3}\mathbf{g}_B \tag{2.20}$$

$$\mathbf{A} = \frac{7}{3}\mathbf{A}_A - \frac{4}{3}\mathbf{A}_B \tag{2.21}$$

where index A belongs to the ferric iron Fe(III) and B to the ferryl iron Fe(IV) (or equivalently ferrous iron Fe(II)). The spin projection coefficients derive from the Clebsch Gordan coefficients known from the theory of a angular momentum addition [55]. Since

$$< Sm_S|\beta\vec{S}\mathbf{g}\vec{B}_0|Sm_S > = < Sm_S|\beta(\vec{S}_A\mathbf{g}_A + \vec{S}_B\mathbf{g}_B)\vec{B}_0|Sm_S >$$

holds $|Sm_S >$ can be written in terms of eigenstates of $(\vec{S}_A\mathbf{g}_A + \vec{S}_B\mathbf{g}_B)\vec{B}_0$, called $|S_Am_{S_A}; S_Bm_{S_B} >$:

$$|Sm_S > = \sum_{m_{S_A}, m_{S_B}} < S_Am_{S_A}; S_Bm_{S_B}|Sm_S > |S_Am_{S_A}; S_Bm_{S_B} >$$

By calculating the coefficients $< S_Am_{S_A}; S_Bm_{S_B}|Sm_S >$ for the case $S_A = 5/2$, $S_B = 2$, $S = 1/2$, the factors $7/3$ and $-4/3$ are received [55].

2.8 Instrumentation

2.8.1 X-band CW EPR

CW EPR measurements at X-band frequency (9.5 GHz) were performed on a spectrometer of type ESP300E (Bruker). Here a standard rectangle TE102 was used. It exhibits an unloaded Q of around 4000. A helium flow cryostat (Oxford ESR 900) enables the adjustment of the temperature at the position of the sample from 4.2 to 200 K. The temperature was measured by a thermocouple against liquid nitrogen 77 K and controlled by an ITC 4 temperature controller (Oxford). Prior to the first measurements, the temperature was calibrated by an Au 0.03 At%Fe/NiCr thermocouple against a reference at liquid nitrogen. For the exact measurement of the microwave frequency a Hewlett Packard 5352 B microwave counter was employed. An NMR ER 035 Teslameter from Bruker allows an exact measurement of the magnetic field strength at the position of the sample.

2.8.2 X-band CW ENDOR

For the CW ENDOR measurements a Bruker ESP300E spectrometer was employed as well. The ENDOR cavity used is of type TM110 with the rf coil fixed within the cavity on the outer wall of a doubly walled quartz dewar [72]. The rf field produced by the coil is chosen perpendicular to the microwave field in the resonator in order to reduce contributions to the fields from mixing frequencies. In the inner space of the dewar the sample is cooled down by a variable helium current, while the space between is evacuated to 10^{-4} mbar for insulation. The equipment for temperature adjustment and control is equivalent to the one used in the CW spectrometer (EPR 910 Oxford). The rf signal for the rf coils is provided by a SMT Rhode&Schwarz frequency synthesizer. For CW ENDOR the rf frequency needs to be frequency modulated in order to detect derivative signals. The self-built ENDOR accessary is described in [72]. A self-written correction program UCOR2 adjusts the output of the frequency synthesizer in order to get a constant output rf power of the ENI over a frequency range between 0.5-50.5 MHz. The rf circuit is terminated by a 50 Ω load.

2.8.3 X-band Pulsed ENDOR

The pulsed ENDOR experiments are performed on a spectrometer of the ESP380 series (Bruker), which allows an operation in the CW as well as in the pulse mode. The microwave pulses created by use of the pulse programmer in the High Power Pulse channel of the spectrometer are amplified in a travelling wave tube amplifier TWT 117X (Applied Engineering Systems Inc.) to a maximum output power of 1 kW before they reach the dielectrical sapphire ring resonator (1052 DLQ-H, Bruker) [65]. The detector diode has to be protected from this high power microwave pulse by several well adjusted defense pulses with a minimum length of 280 ns. Q is adjusted to around 800 for a pulsed ENDOR and to $\leq$ 500 for ESE by overcoupling the resonator. At critical coupling the resonator exhibits a Q of around 5000 at 10 K. The rf frequency required for a pulsed ENDOR experiment is synthesized in an ESP 360 DICE system (Bruker) and amplified in an ENI A 500 power amplifier to maximum 500 W output power.

2.8.4 W-band EPR

The high field EPR measurements were performed on a Bruker Elexsys High Field EPR spectrometer of the ESP680 series. It employes the so-called superheterodyne technique: the microwave source and detection operates at an intermediate frequency of 9 to 10 GHz. This frequency is upconverted to the 94 GHz excitation signal in the W-band microwave bridge before it reaches the probehead. In order to decrease power losses the waveguide which connects the probehead and the W-band bridge output is oversized and adapted to standard W-band size only at a small distance from the cavity. The cylindrical cavity (3 mm diameter) operates in the TE011 mode. The volume of the EPR sample lies around 0.5 mm^3. Its resonance frequency exhibits a strong sensitivity on size, position and physical properties of the sample. The static magnetic field at the position of the sample is produced by a superconducting split-coil magnet. It reaches magnetic field strengths of around 6 T maximum and operates at a temperature of 4.2 K. It is cooled by a liquid helium reservoir which is surrounded by a second reservoir filled with liquid nitrogen for insulation. For field sweeps up to $\pm$ 400 G room temperature coils sweep the magnetic field at the site of the sample with a maximum precision of better than 10 mG over a full sweep width. In order to achieve larger sweeps the main coil field

has to be swept.

Chapter 3

Experimental Results

3.1 High Field EPR on Amino Acid Radicals in RNR

3.1.1 Tyrosine Radicals in Class Ia RNR

The tyrosine radical Y122• in wild type *E. coli* RNR has been well characterized by various methods of EPR spectroscopy. At 9 GHz X-band frequency it exhibits a doublet EPR signal due to a large hyperfine coupling ($\sim 2\ mT$) from one of the two β methylene hydrogens. For phenoxyl type radicals the couplings to the H_β protons have been shown to yield insight into the dihedral angle θ between the p_z orbital of the neighbouring ring carbon and the $H_\beta - C$ bonding axis, since $A_{iso}(H_\beta)$ depends upon θ according to the McConnell relation

$$A_{iso}(H_\beta) = \rho_C^\pi (B_1 + B_2 cos^2\theta) \tag{3.1}$$

where ρ_C^π denotes the spin density at the ring carbon C_1 next to the β protons and B_1, B_2 are empirical constants [43, 44]. Employing this relation with $B_1 = 0$ and $B_2 = 4$ mT, a dihedral angle of 33^o was found for Y122• [45]. CW-ENDOR experiments revealed the somewhat smaller hyperfine couplings to the ring protons at positions 3,5 and 2,6, and the second β hydrogen [45]. The knowledge about these coupling strengths made it possible to determine the spin densities throughout the aromatic ring [45, 46], which are found to be symmetric with respect to the $C_1 - C_4$ axis. Employing ^{17}O labelled tyrosine made it possible to measure the spin density at the phenol oxygen directly: $\rho = 0.29 \pm 0.02$ [46]. At high frequency bands (145 GHz) a resolved g-anisotropy was observed. The measured g-tensor principal values were $g_x = 2.00912$, $g_y = 2.00457$, and $g_z = 2.00225$ [47]. The proposed orientation of the g-tensor in the tyrosine radical is shown in Figure 3.1.

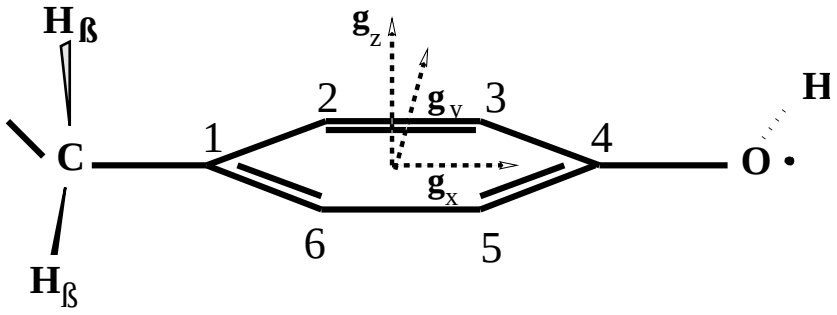

Figure 3.1: *Orientation of the g-tensor axis in a tyrosine radical*

Most recently an orientation selective pulsed ENDOR study at 140 GHz microwave frequency of a frozen solution has reproduced the hyperfine coupling tensors to the ring protons and H_β and their orientation with respect to the g-tensor [48]. Investigations on the tyrosine radical in mouse RNR, Y177•, revealed several differences to Y122•: First of all, Y177• exhibits a faster relaxation throughout the temperature range than Y122•, thus saturating at higher microwave power levels [49]. The reason for this may be a stronger interaction with the neighbouring diferric center, either due to the smaller exchange coupling within the iron center [80], which results in a larger population of paramagnetic excited states at comparable temperatures, or due to a larger coupling of the tyrosine spin to the excited paramagnetic states of the di-iron center of the irons itself, which may be correlated with the existence of a hydrogen bond to the phenol oxygen in Y177• [50]. The presence of this bond in mouse R2 and its absence in *E. coli* R2 has been verified directly in a pulsed Q-band EPR study [50]: In this study, the protein was reconstituted in D_2O in order to exchange hydrogen bonded protons. The experiment revealed the corresponding hyperfine tensor principal components of the proton, their principal axes, and the bonding length (1.89 Å). As the most probable candidate for the H-bond, the water ligand of Fe_1 was suggested [50]. This hydrogen bond has a pronounced influence on the g-value along the $C_1 - C_4$ axis, g_x, as studied in high field EPR [51, 52]: For Y177• this value is lowered to $g_x = 2.0076$ in comparison to $g_x = 2.00912$ for Y122• (see Figure 3.2). Furtheron, the hydrogen bond is supposed to break the symmetry for the spin densities in the aromatic ring. This has been shown by the unequal α-hydrogen coupling constants for positions 3 and 5 measured with ENDOR [51].

3.1.2 High Field EPR Measurements on Tyrosine Radicals in RNR

A main aim of this dissertation was an EPR spectroscopic characterization of protein-associated tryptophan radicals using high-field EPR at W-band and their discrimination from protein-associated tyrosine radicals. Therefore, spectroscopic properties of tyrosine radicals at 94 GHz are described first.

In this section high field EPR experiments (at 94 GHz) on the tyrosine radicals in active wild type R2 of *E. coli* and mouse RNR are reported. There will be a focus on the investigation of the g-tensor anisotropy exhibited by these radical types.
Wild type *E. coli* and mouse R2 for Tyr•, as well as mutant apoR2-Y122F (*E. coli*) and apoR2-Y177W (mouse) protein for Tryp• were prepared as described in [27, 107] by M. Kolberg and Dr. S. Pötsch.
The wild type samples containing Tyr• were filled into a W-band tube (0.9 mm o.d. and 0.7 mm i.d.) and stored at liquid nitrogen temperature.

Y122• in *E. coli* R2 and Y177• in mouse R2 are measured at 94 GHz W-band frequency. The spectra of the Tyr• in the wild type samples are shown in Figure 3.2 and show a well resolved g-anisotropy. The g_x component of Y122• is larger than g_x for Y177•, while the other components of the g-tensor are comparable for both radicals. A hyperfine pattern is resolved on the g-components for both species: The line of g_y is split by a single large coupling, the other g-components show splittings, which can be attributed to at least two couplings: In Y122• on g_x at least three lines are resolved, in Y177• four.

For the interpretation of the spectra a simulation and fit program written in FORTRAN 77 was employed, which calculates EPR resonance positions to second order perturbation theory. The g-tensor principal values, Gaussian line width, hyperfine tensor principal values and their orientations with respect to the g-tensor axes are used as start parameters and the resonance positions of powder average spectra are fit by a general linear least square fit. Arbitrary angles between axes of g- and hf-tensor are possible. An exact description of the algorithm is found in reference [112]. Linewidth and g-tensor principal values were fitted while hyperfine tensor literature data were used as start parmeters in the simulation. The values obtained from the simulation of the spectra for g-tensor principal values and hyperfine couplings of the wild type samples are listed in Table 3.1.

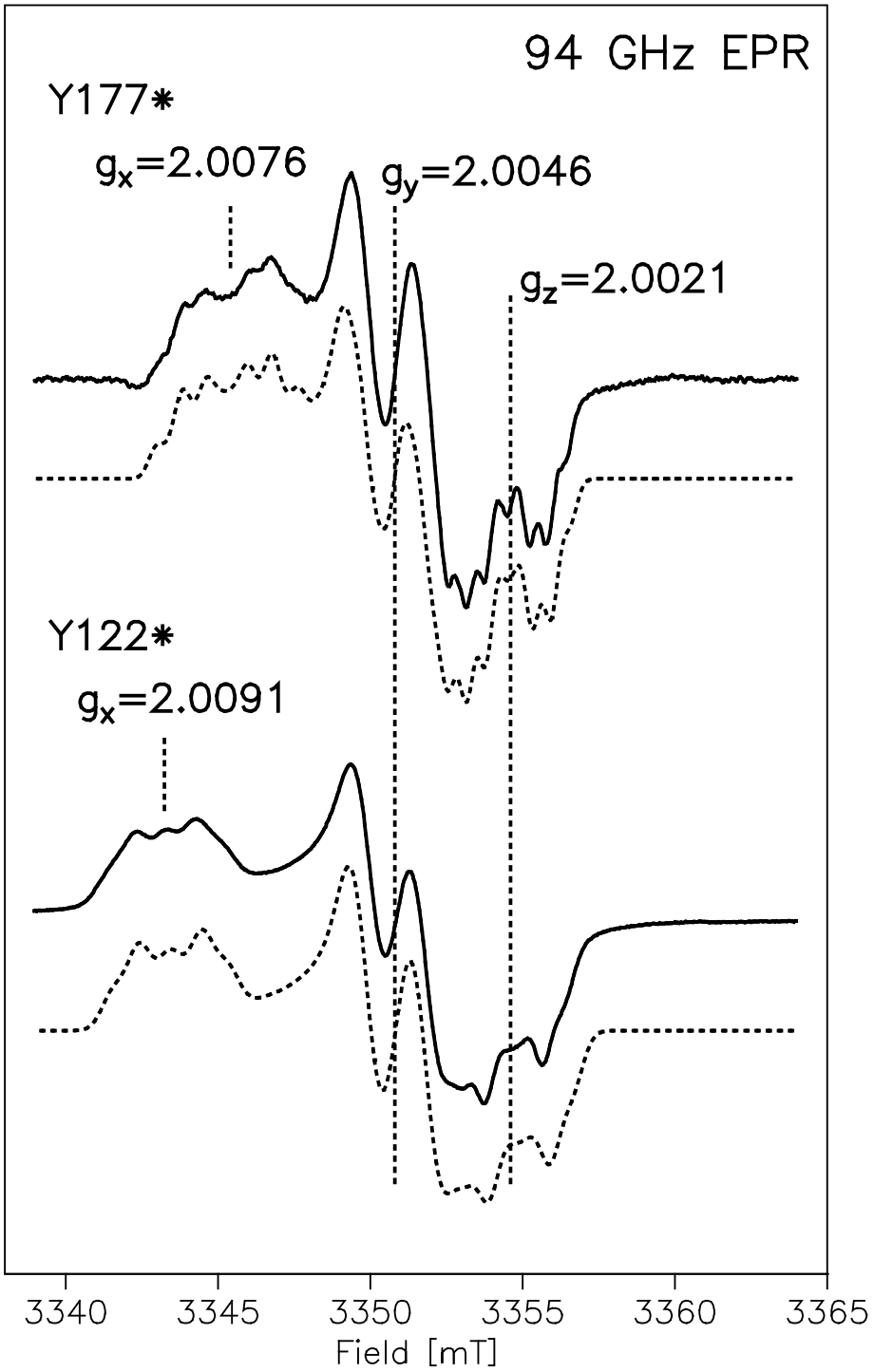

Figure 3.2: *High Field EPR Spectra (94 GHz) of Y122• in Escherichia coli and Y177• mouse R2; Experimental conditions: temperature 20 K, microwave power 2 μW, time constant 20 ms, modulation amplitude 4 G, modulation frequency 100 kHz; The dashed lines are best simulations using the parameters given in the Table 3.1.*

g-tensor principal values for the tyrosine radicals			
radical	g_x^a	g_y^a	g_z^a
Y122•	2.0092(2)	2.0046(2)	2.0021(2)
Y177•	2.0076(1)	2.0046(1)	2.0021(1)
hyperfine tensor principal values for Y122• (mT)			
proton	A_x^b	A_y^b	A_z^b
H_β	2.17	1.96	2.06
$H_{(3,5)}$	0.96	0.28	0.70
hyperfine tensor principal values for Y177• (mT)			
proton	A_x^b	A_y^b	A_z^b
H_{β_1}	2.15	1.90	2.14
H_{β_2}	0.95	0.25	0.57
$H_{1(3,5)}$	-0.91	-0.44	-0.66
$H_{2(3,5)}$	-0.75	-0.49	-0.58
H_{H-bond}	0.25	-0.12	-0.12

Table 3.1: *g-tensor principal values and hyperfine tensor principal values for the resolved α and β proton couplings as used for the simulation of the Y122• and Y177• EPR spectra (see Figure 3.2).*

[a] The numbers in brackets denote errors in the last digit.

[b] A-tensor assumed to be collinear with the g-tensor.

protein/tyrosine	g_x	H-bond	reference
E.coli R2-Y122•	2.0091	-	this work
Salmonella typhimurium R2	2.0089	-	[52]
HSV I R2	2.0076	+	[50]
mouse R2	2.0076	+	this work
spinach PS II Y_D•	2.00745	+	[100]
Synechococcus elongatus PS II Y_D•	2.00767	+	[101]

Table 3.2: *H-bond correlated g_x values for protein-associated tyrosyl radicals. The g_y and g_z are very similar for all of them and do not shift.*

Both tyrosine radicals Y122• and Y177• exhibit a rather similar line shape: The spectra ar dominated by the g-anisotropy with a subsplitting of each g-component by the hf couplings. The (for an organic radical) relatively large g-anisotropy can be attributed to the high spin density at the phenoxyl oxygen and is characteristic for tyrosine radicals. Oxygen exhibits a larger spin-orbit coupling constant than for example carbon or nitrogen [57]. Since the spin orbit coupling causes a by-mixing of excited states to the ground state of the unperturbed Hamiltonian in perturbation theory, which has an effect on the g-tensor, the g-anisotropy of oxygen centered radicals is larger than for other C and N centered organic radical species.
However, there are significant differences in the spectra for the tyrosine radicals in both species: The shift of g_x for Y122• compared with Y177• has previously been attributed to a H-bond to the phenoxyl oxygen in Y177•, which is missing in the *E. coli* protein [50]. In Table 3.2 the g_x values of some protein-bound tyrosine radicals are listed.

A hydrogen bond to the phenoxyl oxygen has already been detected for mouse R2 [50] and HSV I R2 [50], as well as PSII in spinach and *Synechocystis* 6803 Y_D• [102, 103]. In *E. coli* no similar bond was observed [50]. Thus, the common scheme indicates a relation between a shift in the g_x value, which is supposed to align with the phenoxyl oxygen-C4 bond (see Figure 3.1), and the existence of a hydrogen bond to the phenoxyl oxygen.

Theoretically, this is described by Stone's g-tensor model [104]. According to this model the g_x-shift originates from an excitation of the electron into a non-bonding lone-pair orbital of the oxygen. The deviation of g_x from the free electron value (g=2.00231930386) is given by:

$$\Delta g_x \sim 2\xi\rho_O^\pi c_y^2/\Delta E_{n\pi^*} \tag{3.2}$$

where ξ denotes the spin orbit coupling constant of oxygen, ρ_O^π the π spin density at the oxygen and c_y the orbital coefficient of the lone-pair orbital described by a wave function $\psi_n = c_s s + c_x p_x + c_y p_y$. The H-bond is expected to

- decrease the spin density at the phenoxyl oxygen, for the positive partial charge at the proton increases the negative partial charge at the oxygen [105].
- increase the energy difference $\Delta E_{n\pi^*}$ between the non-bonding n- and half filled π orbital, thereby decreasing Δg_x [104].

Both effects will lead to a shift especially for g_x [105], thus explaining the experimental results.
The differences in the hyperfine pattern between Y177• and Y122• can be attributed to the H-bond as well. The C_2 symmetry of the phenoxyl ring with respect to the C1-C4 axis (see Figure 3.1) and therefore the equivalence of positions 3,5 and 2,6 within the ring is lifted due to the presence of the H-bond. This becomes evident in the spectra by comparing the g_x and g_z region: For Y122• three lines are observed in the hyperfine pattern on g_x deriving from a 1:2:2:2:1 line pattern: The large splitting caused by the β proton is superimposed by a 1:2:1 subsplitting caused by the identical couplings of the ring protons at the 3,5 positions. In Y177• the protons are inequivalent of which the four strongest lines are clearly resolved.

The hf-tensor for the H-bond proton in Y177• was measred by ENDOR previously [50]:

$$A_1 = 1.06\,MHz$$

$$A_2 = A_3 = -0.53\,MHz$$

It is not resolved in the EPR spectra.

3.1.3 High Field EPR Measurements on Tryptophan in RNR

In this chapter, measurements at high field EPR on protein-associated tryptophan radicals are reported. The investigation will be focused on the g-tensor at 94 GHz

and the hyperfine pattern exhibited by the spectra. The purpose is a comparison with the tyrosine radicals of the last section and a discrimination of both radical types based on their g-anisotropies.

The preparation of the samples was done by Dr. S. Pötsch. The tryptophan radicals were trapped during the reconstitution reaction. Herefore a solution of ApoR2 Y122F was quickly mixed with ferrous ammonium sulfate (7.2 mM) and frozen after 26 s reaction time in a W-band EPR tube [54]: During the reconstitution reaction Fe(II) is built into the protein, which is converted to its reduced form. Subsequent activation with oxygen leads to the formation of the short-lived intermediate X, which is capable of oxidizing the tyrosine in wild type protein. In mutants Y122F and Y177W short-lived tryptophan radicals are generated instead via the oxidative power of intermediate X.

The R2-Y177W sample was treated in a similar manner (see reference [53]). The tryptophan radicals W111• and W177• were stabilized at liquid nitrogen temperature in frozen solution.

In Figure 3.3 the EPR spectra of the two different tryptophan radicals are displayed. The EPR spectra of both radicals are dominated by hfs couplings, they do not exhibit a resolved g-anisotropy at 94 GHz. However, the asymmetry of both spectra implies an orientation dependence of the resonance position and therefore an anisotropic g-tensor. This asymmetry is larger at W-band than at X-band frequency (see spectra in Figure 3.5), however, the deviation of the g-components from the free electron value is significantly smaller than for the tyrosine radicals. The spectrum for W177• shows a two line hfs pattern, while W111• exhibits a four line hfs pattern: In the first case there is one large hyperfine coupling, in the second one, two couplings. The parameters for the simulations of the spectra are listed in Table 3.3.

For the tryptophan radicals the g-tensor anisotropy is poorly resolved even at 94 GHz and the g-tensor is only obtained from spectral simulation. In tryptohan radicals, the spin density is essentially localized at C and N nuclei which exhibit only small spin orbit coupling constants. Thus, using high-field EPR (94 GHz), one can clearly distinguish between tyrosyl and tryptophan radicals in a protein solely based on the resolved anisotropies in the g-factors without a need of further isotope labelling. Both tryptophan species exhibit a nearly axial g-tensor.

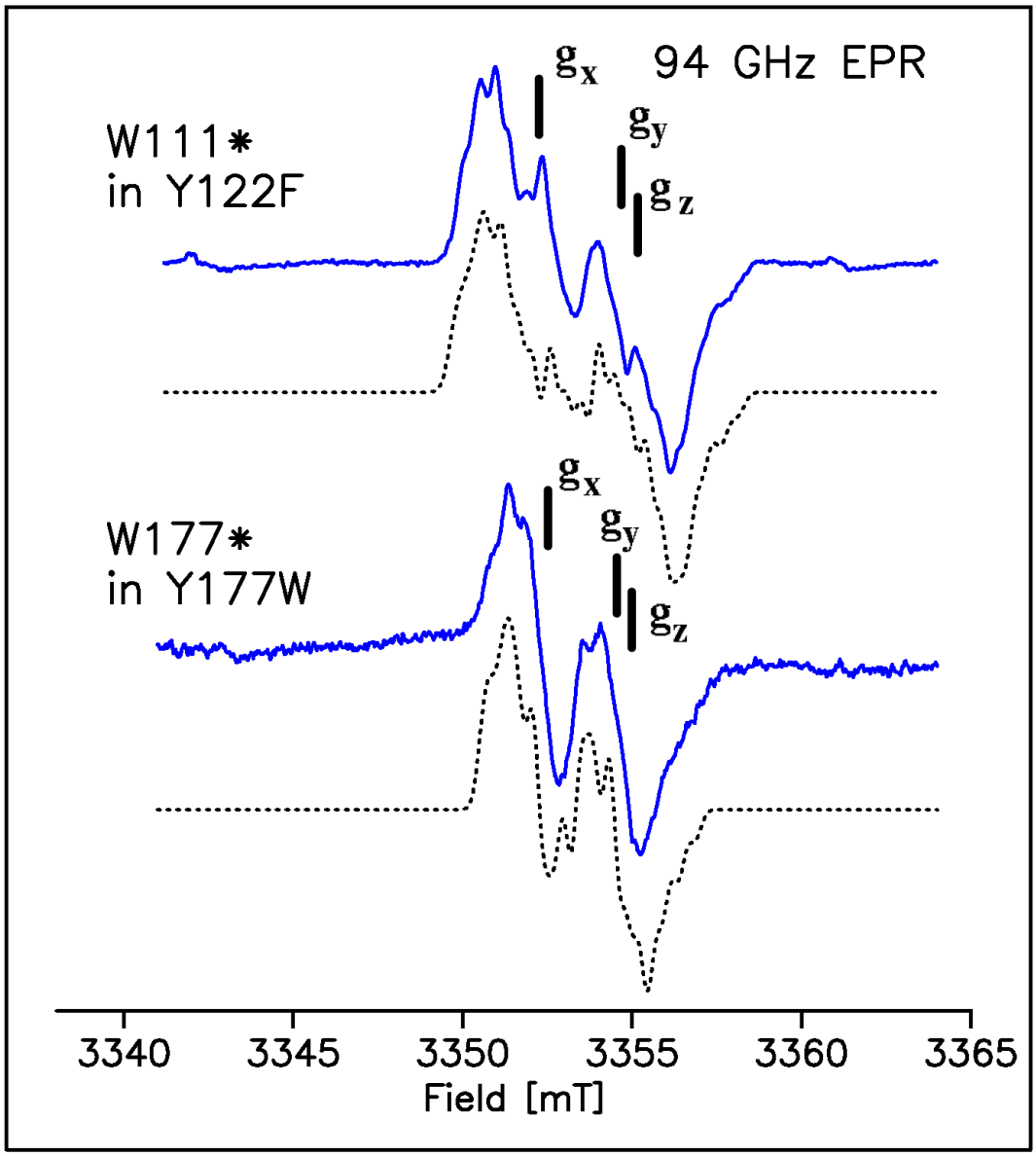

Figure 3.3: *High Field EPR Spectra (94 GHz) of W111• in mutant Y122F (Echerischia coli) and W177• in Y177W (mouse R2); The position of the g-tensor principal values is indicated. Experimental conditions: microwave power 2 μW, time constant 81 ms, modulation amplitude 1 G, modulation frequency of 100 kHz; W111• was recorded at 40 K, whereas W177• at 20 K. The dashed lines are simulations using the parameters given in Table 3.3.*

g-tensor principal values for the tryptophan radicals			
radical	g_x^a	g_y^a	g_z^a
W111•	2.0033(1)	2.0024(1)	2.0021(1)
W177•	2.0035(1)	2.0025(1)	2.0023(1)
hyperfine tensor principal values for W111• (mT)			
proton	A_x	A_y	A_z
H_{β_1}	2.83	2.83	2.83
H_{β_2}	1.38	1.38	1.38
$^{14}N^b$	0.08	0.08	1.05
$H^c_{(5)}$	-0.66	-0.03	-0.52
$H^d_{(7)}$	-0.03	-0.59	-0.46
hyperfine tensor principal values for W177• (mT)			
proton	A_x^b	A_y^b	A_z^b
H_{β_1}	2.25	2.25	2.25
$^{14}N^b$	0.07	0.07	0.94
$H^e_{(5)}$	-0.56	-0.09	-0.46
$H^f_{(7)}$	-0.63	-0.16	-0.52

Table 3.3: *g-tensor principal values and hyperfine tensor principal values used for the simulation of the tryptophan radicals shown in Figure 3.3.*

[a] The numbers in brackets denote errors in the last digit.

[b] A-tensor assumed to be collinear with the g-tensor.

[c] direction cosines with respect to the g-tensor axis:
$l_x = 0.982, l_y = 0.191, l_z = 0.$

[d] direction cosines with respect to the g-tensor axis:
$l_x = 0.500, l_y = 0.866, l_z = 0.$

[e] direction cosines with respect to the g-tensor axis:
$l_x = 0.978, l_y = 0.208, l_z = 0.$

[f] direction cosines with respect to the g-tensor axis:
$l_x = 0.985, l_y = -0.174, l_z = 0.$

Surprisingly, the hyperfine splittings of both tryptophan radicals look very different. An analysis of the spectra shows that W111• exhibits two large isotropic β proton couplings whereas W177• has only one large β proton hf-coupling. This is attributed to different side chain orientations, which strongly influence the magnitude of the β proton hf-couplings according to the McConnell relation (see equation 3.1). In this phenomenological relation (equation 3.1) the isotropic part of the β proton hyperfine coupling is related to the π spin density at the adjacent ring carbon atom and the dihedral angle θ between the axis of the respective ring carbon p_z orbital and the projected $C_\beta H_\beta$ bond. The dihedral angles have been determined for both cases, W111• and W177•: In W111• they are 13^o and 133^o [44], in W177• 90^o and -30^o [53] (the empirical constants were taken as: B_1=0, B_2=5 mT). An CH-bond lying in the plane of the ring gives a negligible overlap with the ring carbon p_z orbital and therefore yields a small, presumably unresolved β proton hyperfine coupling. This is the case for the 90^o H_β dihedral angle in W177•, while the -30^o H_β dihedral angle is expected to yield a large proton coupling. This explains that only one resolved coupling is observed, while for W111• none of the H_β lies in the ring plane and thus two large couplings are seen.

Figure 3.4 sketches the projection of the methylene H-bonds and the dihedral angles for both tryptophan radicals.

This pronounced effect in the spectra was used to assign the radical to specific tryptophan sites in the protein based on X-ray structure data [54]. For a good simulation of both spectra three additional couplings were necessary: One highly anisotropic coupling to the tryptophan nitrogen and two couplings deriving from ring protons (H_5 and H_7). The couplings as well as the respective spin densities at the nuclei have been determined in previous EPR and ENDOR studies at X-band [44, 53]. For the simulation of the W-band spectra the same values for the hf-tensor components are used as reported in these investigations. The simulations show a good agreement between the couplings reported previously and the spectra recorded in this work.

In Figure 3.5 the X-band and high field spectra of the tyrosine radical Y177• are compared directly with the tryptophan radical W177• in order to emphasize the differences in the g-anisotropy. Y177• and the tryptophan radical W177• occur at the same position in the protein and have therefore an equivalent chemical environment.

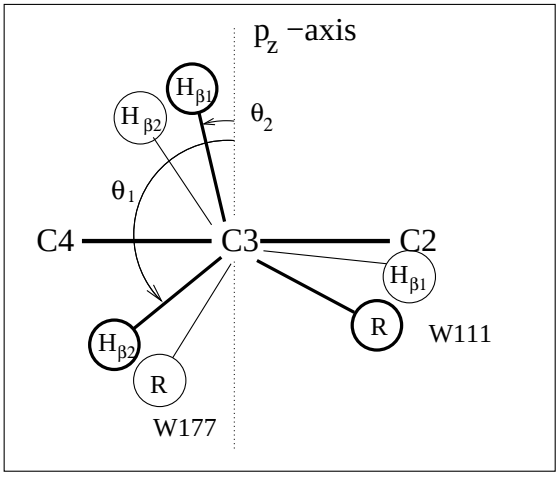

Figure 3.4: *The dihedral angle for the two β protons as calculated from the isotropic β proton coupling strength by the McConnell relation (see text) is sketched for both tryptophan radicals W111• and W177•.*

At X-band, both line shapes are dominated by the contribution of hyperfine splittings, especially the large, nearly isotropic coupling to one of the β protons. Obviously, Y177• and Y177• have the same side chain orientation, e.g. very similar β proton couplings. This leads to the two line pattern for both radicals. The g-anisotropy causes only a slight asymmetry between the two hyperfine splitted lines in the case of the Y177• tyrosine radical. The situation has changed at 94 GHz totally: The line shape of the tryptophan radical is still dominated by the β proton splitting and actually looks very similar to the spectrum taken at X-band frequency. The g-anisotropy is indicated by a slight anisotropy of the two hyperfine splitted lines, which is not seen at X-band. However, the spectrum of the tyrosine radical looks completely different in W-band, since it is dominated by the well resolved g-anisotropy. This shows the advantage of characterizing a radical at different frequency bands.

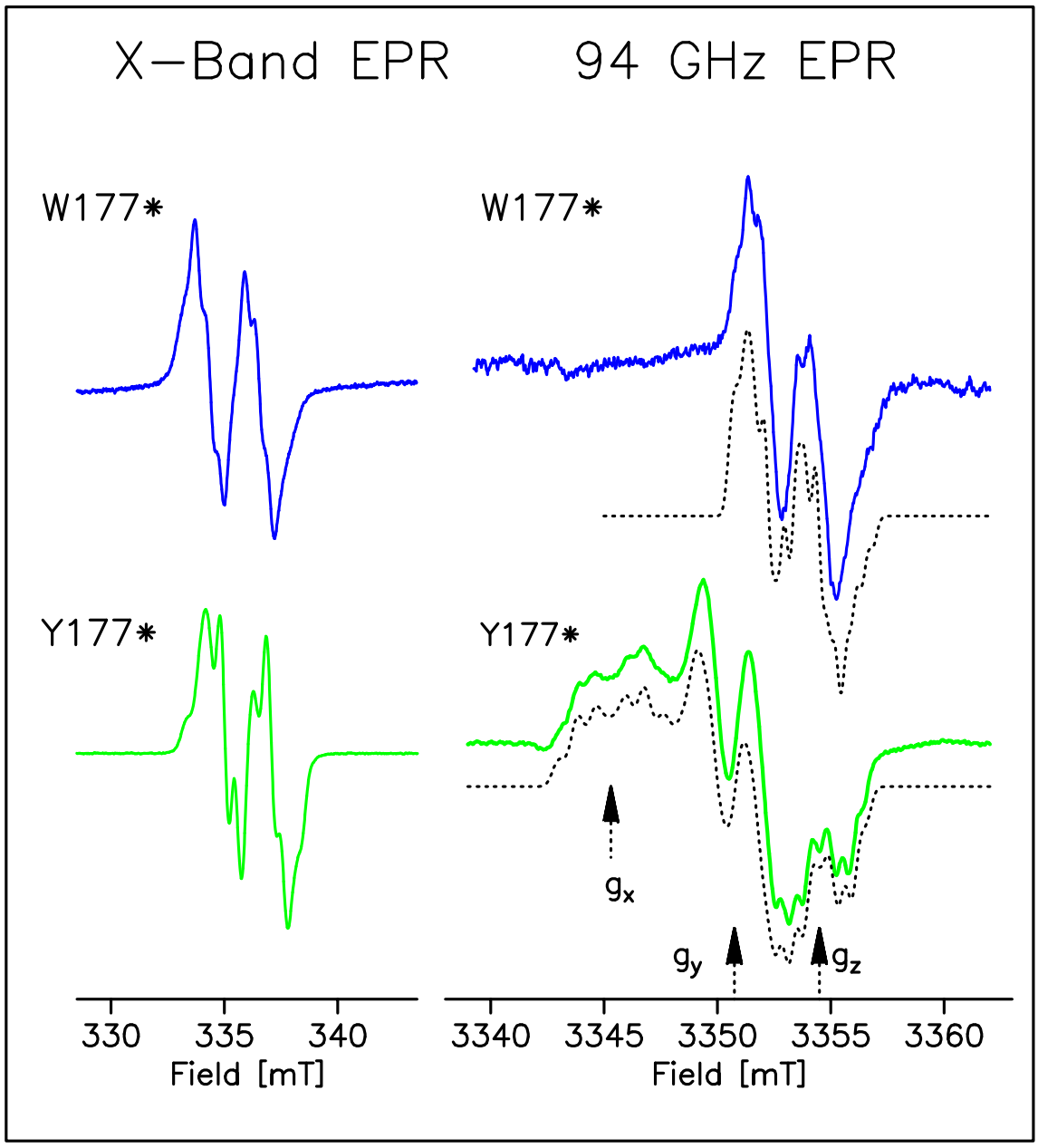

Figure 3.5: *X-band (A,B) and 94 GHz W-band spectra (C,D) of Y177• in wild type mouse R2 (B and D) and W177• in mutant Y177W (A and C); Experimental conditions: X-band: temperature 20 K, microwave power 10 μW, time constant 40 ms, modulation amplitude 1 G, modulation frequency 12.5 kHz. W-band: see Figure 3.2 and 3.3*

3.2 CW-EPR on R2 Y122H Frozen Solution Samples

3.2.1 Measurements at X-band

The protein Y122H contains an EPR sensitive paramagnetic species [108], which is formed spontanously at protein preparation and is very stable (life time at least several days at room temperature). At X-band frequency it shows a singlet Gaussian EPR line of 2.2 mT width. Neither the g-tensor nor hyperfine couplings are resolved. The second part of this thesis will deal with the identification of this so-called center H.

The preparation of the samples was done by Matthias Kolberg [107, 109] and, for the older samples, by Dr. Stephan Pötsch. Hereby, *Escherichia coli* cells carrying the plasmid for overexpression of the mutant Y122H were grown as described in [27]. The purification of the protein was done applying standard methods as described elsewhere [107].
120 μl purified Y122H protein from cells grown in LB medium was filled in a X-band Quartz EPR sample tube of 4 mm diameter.
X-band measurements below 40 K show an isotropic singlet at g=2.0029 with a nearly Gaussian line shape and a line width of 2.2 mT (measured peak-to-peak of the derivative signal). A saturation curve taken at 30 K revealed that the center is not saturable at 30 K up to a microwave power of 200 mW (maximum output of the bridge).
In order to determine the stoichiometry of the center responsible for the EPR signal a spin quantification was undertaken and the result was compared with the protein concentration determined from the UV-Vis spectrum.

As spin standard a 0.2 mM Cu^{2+} complex was prepared by dissolving 2 mM $CuSO_4$ in 100 ml 2 M $NaClO_4$ solution at pH 1.5 (adjusted with HCl). The resulting Cu^{2+} complex exhibits an easily integratable Gaussian shaped $S = 1/2$ EPR signal of 800 G range. The Y122H sample and the standard were measured at 30 K under exactly the same conditions and at 0.1 mW microwave power where both lines were not saturating. The spectra were integrated twice and the areas A of the absorption lines were compared. It came out that only around 3% of the protein contributes to the observed EPR spectrum. Different preparations of Y122H gave contents of the species from $0.8 - 3.0\%$.

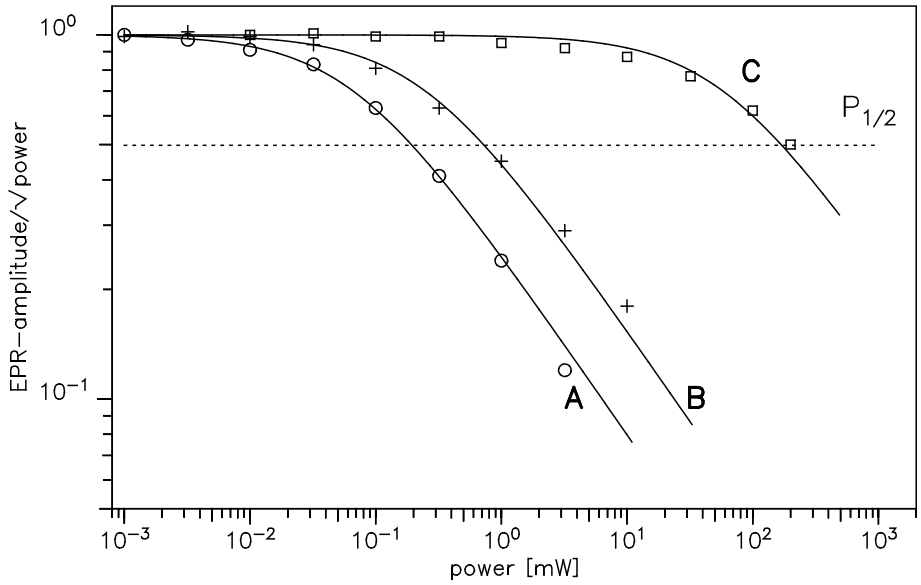

Figure 3.6: *The intensity of the EPR transition devided by $\sqrt{power}$ is plotted versus power double-logarithmically for center H in Y122H (C), intermediate X in mutant Y122F (B), Y122• (A). The center begins to saturate, when the curve starts decreasing. The temperature is 20 K. The phenomenological relation employed is explained in chapter 2.3*

Furtheron, all Y122H samples exhibit a small signal from wild type $Y122\bullet$. This probably derives from content of wild type protein in the cell which could not be removed during the purification. The EPR signal of $Y122\bullet$ overlaps with the new signal. Quantification yielded a tyrosine radical content of around 1%. The tyrosine radical of the wild type contamination, however, could easily be removed upon treating the samples with 10 mM (final concentration) hydroxyurea which scavenges the tyrosyl radical [113]. This procedure keeps the new paramagnetic species intact [108].

In Figure 3.6 the saturation curve at 20 K of the species in Y122H, Y122• in wild type protein, and intermediate X (Fe(III)Fe(IV)) in Y122F is shown. For Y122• a $P_{\frac{1}{2}}$ of about 0.2 mW was determined, for intermediate X $P_{\frac{1}{2}}$ is 0.8 mW and for center H 200 mW at 20 K. The saturation of Y122• is affected by the excited paramagnetic states of the neighbouring diferric iron complex via a small exchange interaction [80], which results in a - for an organic radical - relatively fast spin relaxation. The center H in Y122H, however, is even harder to saturate than the metal centered paramagnetic species intermediate X.

This strongly suggests that we indeed deal with a metal centered species and not

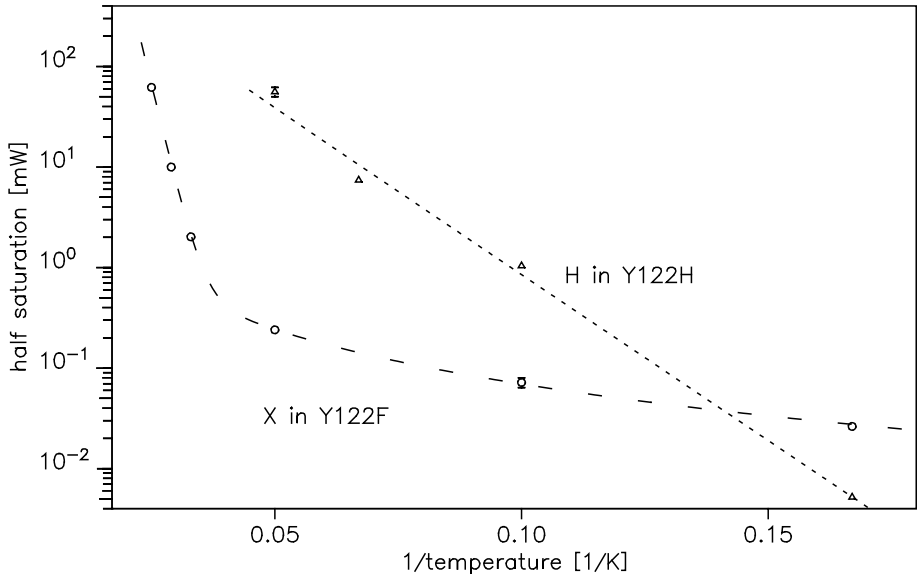

Figure 3.7: *The half power saturation of intermediate X in Y122F and center H in Y122H is plotted versus temperature.* $P_{1/2}$ *was determined from a fit to the saturation points at each temperature employing a phenomenological relation as explained in chapter 2.3. The error is indicated by error bars in case it is larger as the size of the symbols.*

an organic radical interacting with a nearby metal center as is the case for the tyrosine radical. It seemed instructive to determine the saturation behaviour over a larger temperature range for center H. In Figure 3.7 the half saturation power for H and X in Y122F is plotted as a function of the inverse temperature. For these measurements, the temperature at the position of the sample was carefully calibrated using a Au 0.03At%/NiCr thermocouple. In case of the Fe(III)Fe(IV) complex in X an analysis of the saturation behaviour observed yields two distinct temperature ranges which are presumably dominated by different relaxation mechanisms:

Above 20 K a new relaxation mechanism, supposedly an Orbach process [59], becomes dominant resulting in a rapid increase of the half saturation power with temperature. This behaviour has been reported for other metal centers as well, especially copper complexes [59]. For the center in Y122H one cannot see a bend in the relaxation behaviour for the temperature range observed, but the half saturation power increases with temperature approximately $\sim e^{-\Delta/kT}$, since the curve in 3.7 can be fitted with a constant gradient. Δ is here the energy between the ground state and the lowest excited state. The gradient of the half saturation power with inverse temperature can be used to determine the energetic distance to the next

excited state for the iron center according to the equation [114]:

$$lnP_{1/2} = -\Delta/kT + const. \tag{3.3}$$

This equation is only valid, if Orbach processes are dominating the relaxation behaviour in the specified temperature range [59]. For X the gradient between 30 K and 50 K was used (see Figure 3.7), where Orbach relaxation is supposed to dominate. We receive:

$$\Delta_{centerH} = 75 \pm 10\ K$$

$$\Delta_{intermediateX} = 255 \pm 40\ K$$

In the case of the Fe(III)Fe(IV) complex X the exchange coupling constant can be derived from Δ [114, 115]:

$$J = 1/3\Delta = 85 \pm 13\ K$$

The exchange couplings for several protein-associated Fe(II)Fe(III) complexes have previously been determined by EPR power saturation measurements assuming that the relaxation behaviour of the species is dominated by Orbach processes in a certain temperature regime [92]. They exhibit values between $15 - 17\ cm^{-1}$ [92, 93].

In another experiment the Curie law behaviour of the new species was checked: For a single paramagnetic center the product χT, where the magnetic susceptibility χ is proportional to the area under the EPR absorption line, remaines independent of the temperature T. In the case of an EPR signal derived from an excited paramagnetic state, χT will decrease, since for $T \rightarrow 0\ K$ the ground state gets more populated. On the other hand, when χT starts to decrease with temperature from a certain point T_0, it is an indication that nearby excited states ($\sim kT_0$ apart), which are not contributing to the observed EPR transition, become populated [76]. The double integral of the signals for X and H times T were calculated from spectra taken well in the non-saturating domain from 6 K up to around 100 K and their relative magnitude was plotted versus temperature in Figure 3.8.

Y122H shows a Curie-like behaviour from 6 K to 25 K and X from 6 K to around 30 K. Above this temperature range the product χT decreases for both centers suggesting the population of nearby excited spin states. Excited states lying so close to the ground state are particularly observed in metal centered species. In the case of X it is supposed to be the $S = 3/2$ state which starts to become populated at approximately 30 K.

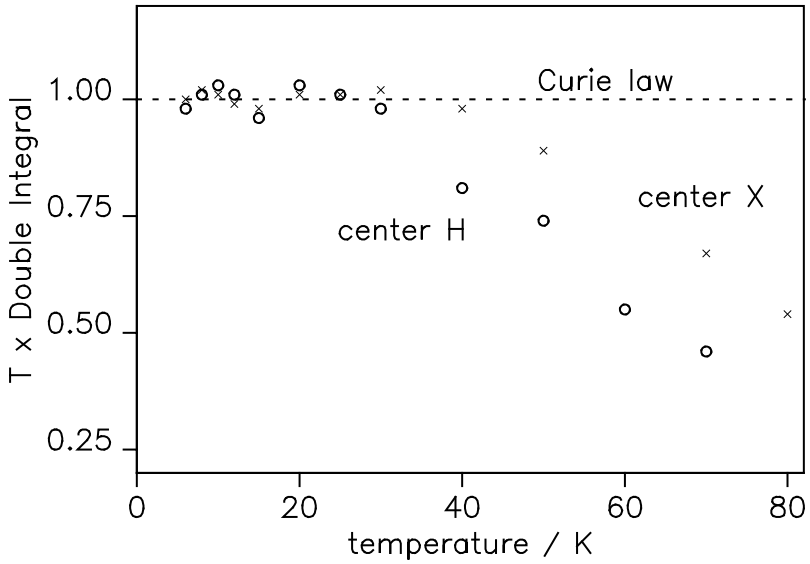

Figure 3.8: *The double integral of the EPR line of center H and X at different temperatures under non-saturating conditions times the temperature T is plotted versus the temperature T in order to check the Curie law behaviour of X in Y122F (crosses) and the new species H (circles).*

3.2.2 ^{57}Fe substituted Y122H

Due to the saturation behaviour of center H, which indicates a metal centered species it is tempting to postulate that the center H derives from an iron cluster. In order to test this hypothesis, ^{57}Fe labelled protein Y122H was prepared by M. Kolberg: $FeCl_3$ containing 95.85% ^{57}Fe was added to the minimal growth medium for the *E. coli* bacteria replacing the other trace metals in [27]. Simultanuously, protein for a control sample was prepared under the same conditions, but adding ^{56}Fe instead of ^{57}Fe to the medium [108]. The iron isotope ^{57}Fe possesses a nuclear spin of 1/2, and therefore it is expected to exhibit a hyperfine interaction with the electron spin of iron in contrast to ^{56}Fe which has $I = 0$. A X-band EPR sample from the ^{57}Fe protein and a sample from the ^{56}Fe protein were made, both were treated with hydroxyurea to quench the tyrosyl radical of the wild type R2 protein contamination and measured at 30 K.

In Figure 3.9 the spectra for ^{56}Fe and ^{57}Fe Y122H are displayed and compared with the corresponding spectra of the paramagnetic center intermediate X (Fe(III)Fe(IV)), where an isotope effect has already been reported [84]. The ^{57}Fe sample exhibits a broadened EPR line of Non-Gaussian shape with a line width of 4.3 mT (^{56}Fe spectrum: 2.2 mT). This clear positive isotope effect confirmed that ^{57}Fe was built into the protein successfully and there is significant spin density on the iron.

Whereas intermediate X contains at least one resolved ^{57}Fe hyperfine coupling in X-band, in center H of Y122H the ^{57}Fe couplings are not resolved and lead only to a considerable broadening of the EPR line. In order to simulate this spectrum starting with 2.2 mT line width it proved necessary to assume at least two iron hyperfine couplings. This will be confirmed in section 3.2.2 by applying ENDOR techniques. With ENDOR it will be possible to resolve the couplings hidden under the broad line width in the CW-EPR spectrum, in order to decide how many iron nuclei are involved in the hfs, and to determine the individual hfs tensors.

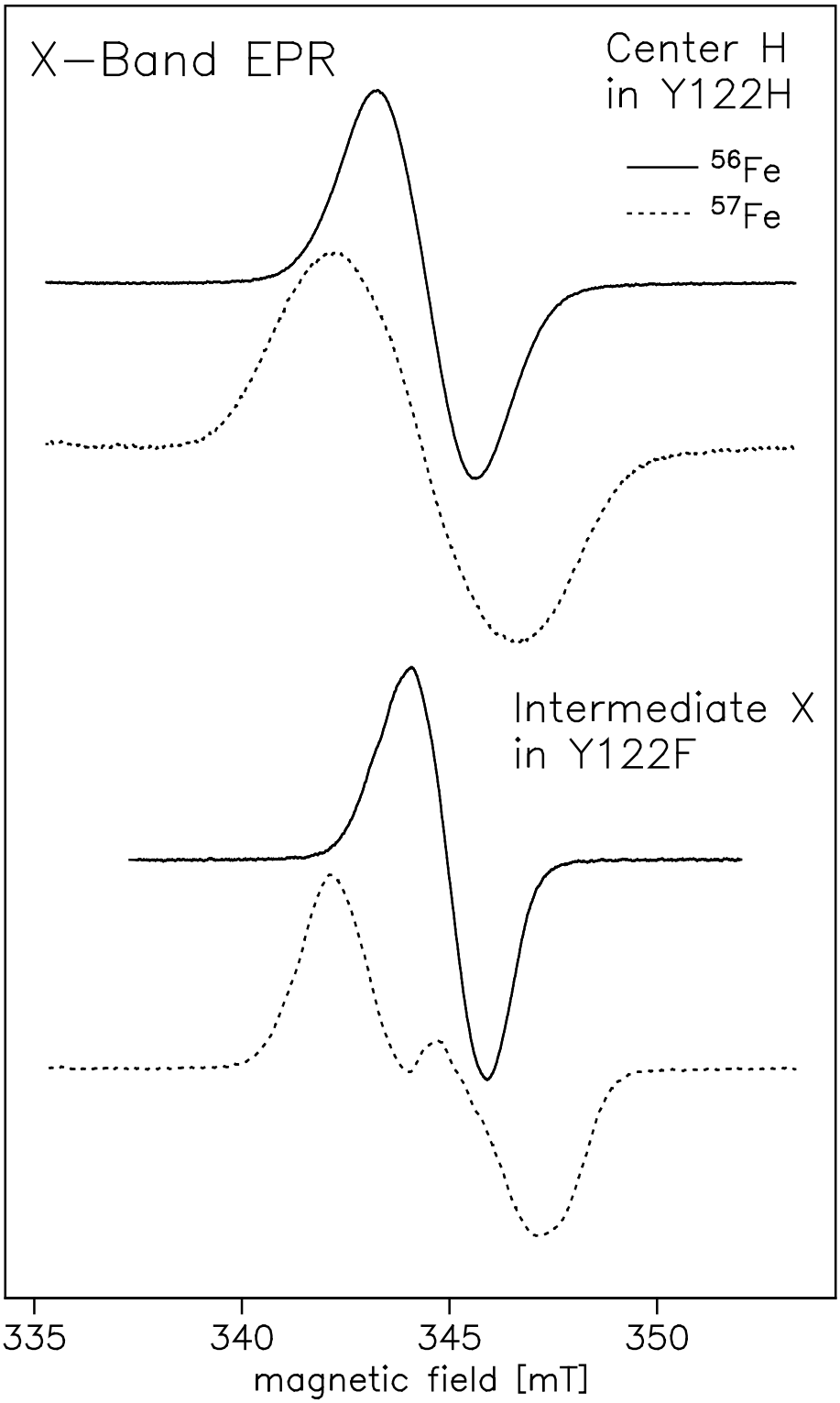

Figure 3.9: *X-band (9.7 GHz) spectra for 1.0 mM center H in ^{56}Fe-Y122H and 0.9 mM ^{57}Fe-Y122H, respectively, were recorded at 30 K, 1 mW microwave power, 12.5 kHz modulation frequency and 0.7 mT modulation amplitude.*
X-band (9.7 GHz) spectra for X trapped by freeze-quenching at 300 ms after treatment of apo-Y122F with $^{56}Fe(II)$ and $^{57}Fe(II)$ (dashed line), respectively, were recorded at 35 K, 1 mW microwave power, 12.5 kHz modulation frequency and 0.2 mT modulation amplitude.

3.2.3 Measurements of Y122H at Q-band and W-band Frequencies

High field EPR is used in order to resolve the g-anisotropy of center H in R2-Y122H, which shows in X-band only a broad single line (see Figure 3.10 A). For the measurements at higher frequency bands samples of the 2 mM Y122H LB solution were filled into a quartz tube of 3 mm diameter (for measurements at Q-band frequency (35 GHz)) and into a quartz tube of 0.7 mm inner diameter, 0.9 mm outer diameter (for measurements at 94 GHz W-band frequency). Both samples were frozen and kept at 77 K liquid nitrogen temperature. At Q-band, spectra were recorded in a temperature range from 20 K to 70 K; at 20 K the g-anisotropy is partially resolved. The high field component (g_z) is separated (see Figure 3.10 B). Towards higher temperature (up to 70 K) the signal gets reversibly broadened and distorted (spectra not shown).

The W-band spectrum in Figure 3.10 C clearly shows that the g-anisotropy of center H is fully resolved at this frequency. A simulation, applying a program which simulates and fits EPR spectra of frozen solution with the g-values as parameters written by Kai Schäfer [112, 162], yielded the g-tensor principal values

$$g_x = 2.0088(1),$$

$$g_y = 2.0040(1),$$

$$g_z = 1.9960(1).$$

The parentheses indicate the error in the last digit. The error was determined by varying the parameter for the simulation until the peaks of simulated and experimental spectra coincide. For the simulation a line width of 2.2 mT (X-band and Q-band) and 3 mT (W-band) and a purely Gaussian line shape was used. The error of the g-values can mainly be attributed to the large line width (3 mT); the error caused by a uncertainty of the frequency or field axis after the calibration procedure is much lower: It lies in the order of 1×10^{-5}. Using the same g-tensor principal values the spectra taken in Q-band could be simulated very well (as shown in Figure 3.10).

The feature at the high-field site of the g_y component of the W-band spectrum of center H is not reproduced by the simulation. It shows the same saturation behaviour as the rest of the spectrum. One possible explanation for this feature is

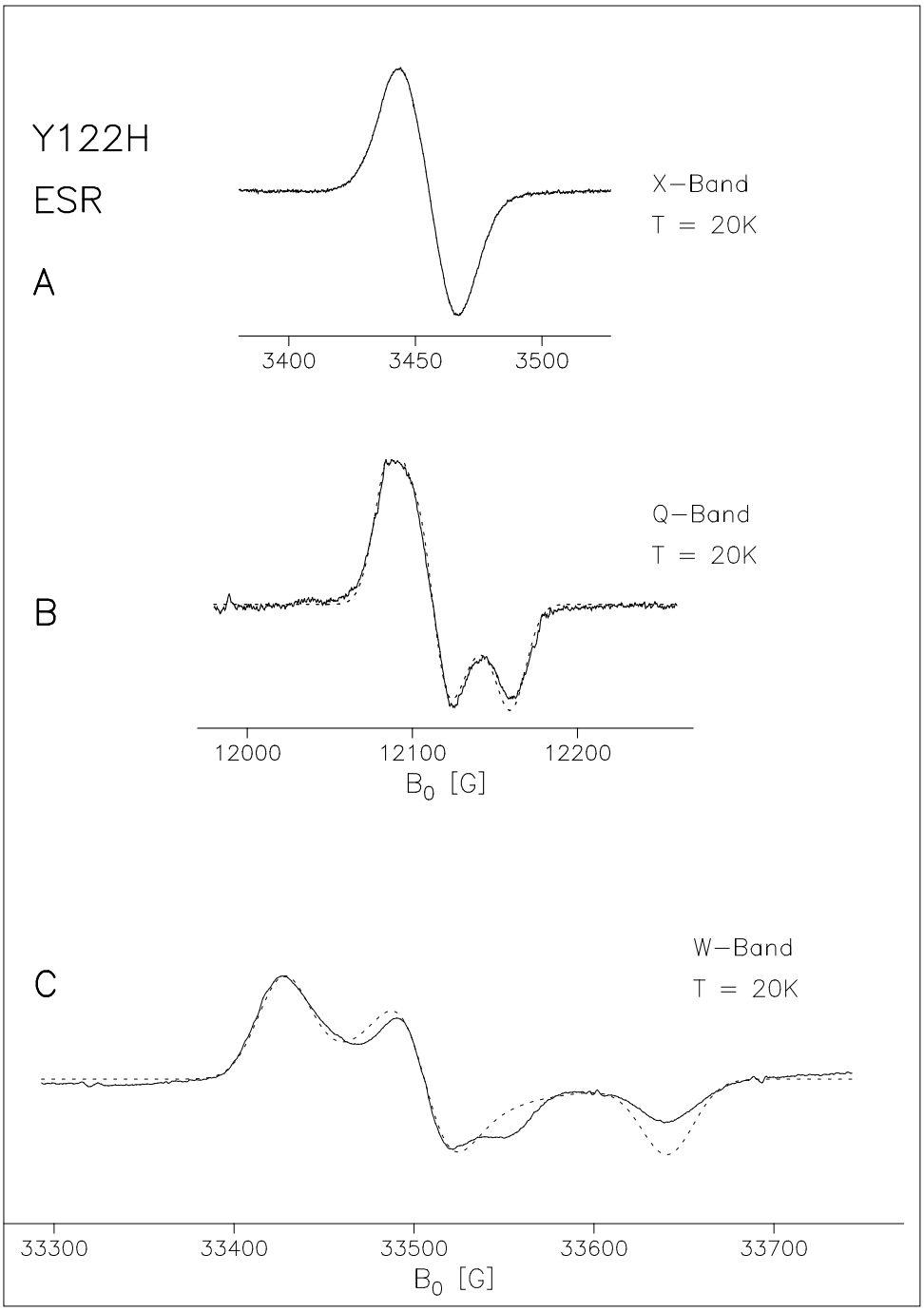

Figure 3.10: *EPR spectra of paramagnetic center H in E. coli R2-Y122H,*
A*: at X-band, 9.7 GHz, 30 K, microwave power: 169 μW, modulation amplitude: 0.2 mT, modulation frequency: 12.5 kHz*
B*: at Q-band, 34 GHz, 20 K, microwave power: 20 μW, modulation amplitude: 0.4 mT, modulation frequency: 12.5 kHz*
C*: at W-band, 94 GHz, 20 K, microwave power: 1.58 mW, modulation amplitude: 0.6 mT, modulation frequency: 100 kHz*
Dashed lines: Simulations;

that a certain percentage of the paramagnetic species center H exhibits a higher g_z value of around 2.000. On basis of this suggestion simulations have been made, which reproduce this feature very well (not shown). In this work, however, this feature is not investigated further.

The W-band spectra were recorded at 20 K. The calibration of the field axis was done by means of a Li:LiF standard sample employing a procedure which is described in section 3.4 of this work. During this procedure the spectra are converted to a 94 GHz field axis. Due to contaminations with traces of manganese(II) in the cavity or the sample, which exhibit EPR transitions around g=2.000 and show 6 hfs peaks 9 mT distant from each other and therefore are overlapping with the signal of center H, a background sweep was done with a sample merely containing buffer without protein Y122H under the same conditions and both spectra were subtracted prior to analysis.
The lowest g-value lies clearly below the free electron $g_e = 2.0023$ and therefore gives a further hint to a metal centered species since organic radicals exhibit g tensor components which are above g_e.
In an analysis of the g-tensor principal values they were compared with g-values reported for other di-iron centers (see Table 3.4): The $S = 1/2$ ground state of intermediate X in the mutant Y122F, a mixed valence Fe(III)Fe(IV) center, exhibits an isotropic singlet of 1.8 mT width in X-band. Q-band spectra, however, reveal a slight g-factor anisotropy with the g-tensor principal values 2.007, 1.999 and 1.994 [84]. In the case of R2, Fe(II)Fe(III) centers have been observed and characterized after γ-irradiation at 77 K of *E. coli* metR2 [92] and after chemical reduction of mouse and Herpes Simplex Virus HSV I protein by treatment with phenazine methosulfate (PMS)/dithionite or, alternatively, hydrazine [93]. The g-values are listed in Table 3.4; they show a larger anisotropy than for the Fe(III)Fe(IV) complex and lie all below 2. This seems to be very characteristic for this type of dimetallic center since the same behaviour is reported from equivalent centers in MMO [83] and different model systems [94], and is confirmed by theoretical calculations [79]. Interestingly, annealing to higher temperature often leads to conformational changes in the metal site of these Fe(II)Fe(III) centers which is reflected in a deviation of the g-values and often also the flip to a $S = 9/2$ ferromagnetic ground state occurs [95, 98].

compound Fe(II)Fe(III)	$\mathbf{g_x}$	$\mathbf{g_y}$	$\mathbf{g_z}$
R2 *E. coli* [92]	1.936	1.818	1.818
R2 mouse [93]	1.92	1.73	1.60
R2 HSV I [93]	1.93	1.75	1.63
MMO in *M. capsulatus* [83]	1.94	1.86	1.74
MMO in *M. trichosporium* [83]	1.95	1.86	1.79
compound Fe(III)Fe(IV)	$\mathbf{g_x}$	$\mathbf{g_y}$	$\mathbf{g_z}$
X in Y122F [84]	2.007	1.999	1.994

Table 3.4: *List of experimentally determined g-tensor principal values for different Fe(II)Fe(III) and Fe(III)Fe(IV) mixed valence di-iron centers.*

Since for Fe(II)Fe(III) centers the components of the g-tensor are typically found below 2 and exhibit a larger anisotropy, they show a different behaviour as observed in center H. Better agreement is achieved in a comparison with the g-tensor of the Fe(III)Fe(IV) species: Its components behave more isotropic than the corresponding components in Fe(II)Fe(III): They show an unresolved singlet at X-band frequency [88, 90, 116, 117] around g=2.000. The respective tensor components measured at higher frequency where they can be resolved are similar to the ones determined for center H. The largest difference is found for g_y which reaches below g_e in X and also the models studied, but remains above the free electron value in the species in Y122H.

Thanks to a cooperation with the research group of Prof. Lawrence Que Jr. in Minneapolis it was possible to investigate another Fe(III)Fe(IV) model complex in our laboratory at high field EPR: The preparation of the Fe(III)Fe(IV) model complex was done by V. L. MacMurdo via an oxidation of $[Fe_2(\mu\text{-}OH)_2[tris(6\text{-}methyl\text{-}2\text{-}pyridylmethyl)amine]_2](ClO_4)_2$ as described in reference [117]. In [117] also an X-band spectrum of the center is reported with an unresolved isotropic g-

tensor. The spectrum (plus simulation) of a sample of this model complex at 94 GHz is shown in Figure 3.11 B in comparison with the spectrum of center H. The field axis is the same for both spectra.

Though the g-tensor of the model complex looks axial, a simulation reveals a slight rhombicity:

$$g_x = 2.00049(5),$$

$$g_y = 1.99865(5),$$

$$g_z = 1.99211(5).$$

g_{iso} is 1.997. In contrast to center H, all g-tensor principal values lie below the free electron value.
By comparing the g-tensors of center H, intermediate X and the model complex, the following points are noticed:

- The range of the g-tensor anisotropy g_x-g_z is 8×10^{-3} for the model complex, 13×10^{-3} for center H and about 13×10^{-3} for intermediate X. For all three centers the range lies therefore in the same order of magnitude.
- The nearly axial behaviour of the tensor in the model complex presumably indicates a more symmetric ligand sphere compared with the tensors of the di-iron centers in proteins. The smaller anisotropy may be attributed to this nearly axial behaviour.
- The most significant and yet unexplained difference between the three tensors is g_{iso} (the center of the spectrum).

Summarizing the discussion, it seems, that the g-tensor of center H is closer to the one exhibited by Fe(III)Fe(IV) complexes than the ones exhibited by Fe(II)Fe(III) centers. ^{57}Fe ENDOR will elucidate the situation more clearly in section 3.3.2.

Another interesting point is the determination of the Gaussian line width for each g-component in the W-band spectrum of center H:
For g_x and g_z a width of 3.0 ± 0.2 mT and 4.0 ± 0.3 mT, respectively, were determined by taking the width at half height for both peaks, whereas the g_y component exhibits a 3.0 ± 0.2 mT peak-to-peak line width. There is not only a clear broadening observed compared with the line width at X-band frequency of 2.2 mT, but

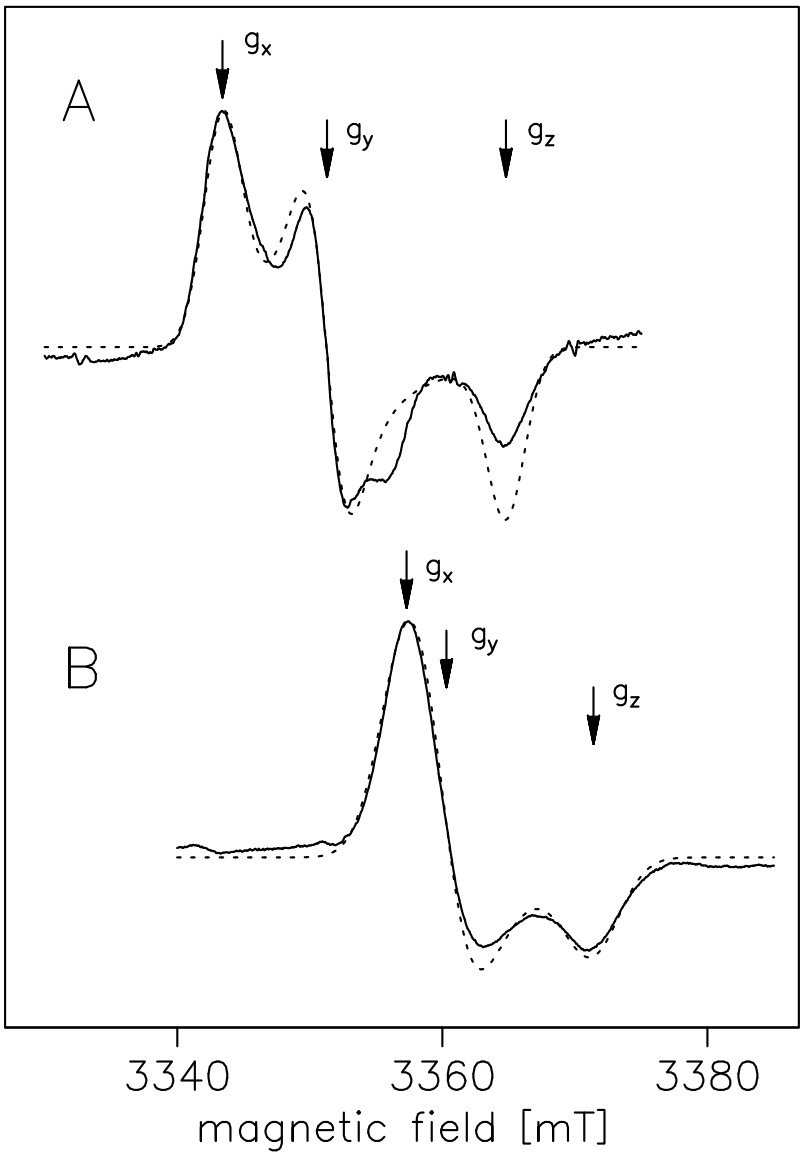

Figure 3.11: *A: W-band (94 GHz) Spectra for center H in R2-Y122H; Experimental conditions: see Figure 3.10*
B: Fe(III)Fe(IV) model complex ($[Fe_2(\mu\text{-}OH)_2[tris(6\text{-}methyl\text{-}2\text{-}pyridylmethyl)amine]_2](ClO_4)_2$) [117]; Experimental conditions: 20 K, 5 μW microwave power, 100 kHz modulation frequency and 0.6 mT modulation amplitude.
The dashed lines show simulations (parameters see text). The g-tensor principal values from the simulation are marked by arrows for both species.

also a pronounced dependence on the orientation. Since hyperfine couplings do not scale with the external magnetic field, the best way to explain this is to assume g-strain, which means, there is a distribution of g-values in different molecules even for the same orientation [59]. As the Zeeman term scales with B_0, this leads to a broadening at higher frequency bands. Supposing that the line width at 94 GHz is solely due to this mechanism, one can expect a broadening at X-band frequency of 1/10 compared with the broadening at 94 GHz caused by g-strain. This would result in widths of 0.3 mT and 0.4 mT, respectively, far below 2.2 mT. Therefore, it is clear that the broadening seen in X-band is exclusively due to hyperfine interactions.

Since the g-anisotropy is resolved in W-band, it is tested in a next step if the unresolved additional broadening observed in the ^{57}Fe substituted sample shows a specific orientation dependence when observed on single g components. Therefore, a 3 mM W-band sample was prepared and measured at 94 GHz frequency. The spectrum is displayed in Figure 3.12. The ^{57}Fe isotope effect leads to a broadening of the g-components compared to the spectrum of ^{56}Fe and is clearly visible despite of g-strain. It could be simulated satisfactorily using the hyperfine couplings determined from ^{57}Fe ENDOR and the Gaussian EPR line width used for the simulation of the ^{56}Fe spectrum (3.0 mT).

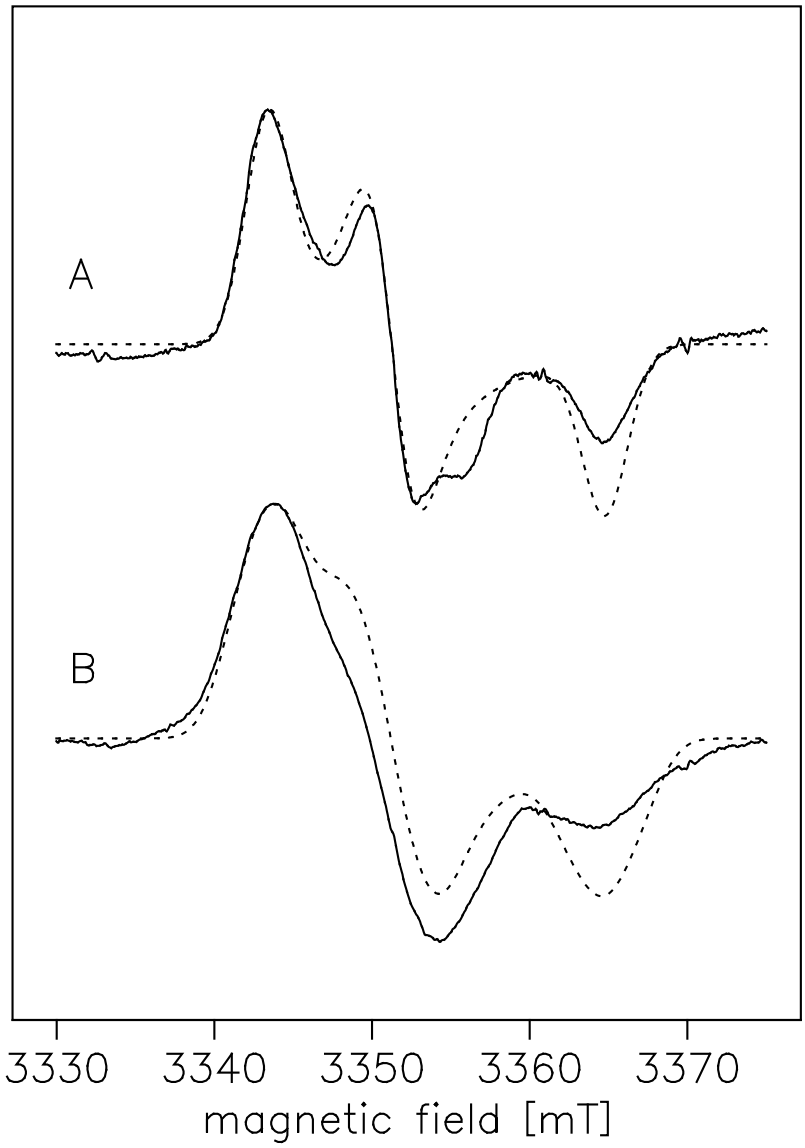

Figure 3.12: *W-band (94 GHz) Spectra for 3.6 mM ^{56}Fe-Y122H and 3.0 mM ^{57}Fe-Y122H were recorded at 20 K, 1.58 mW microwave power, 100 kHz modulation frequency and 0.6 mT modulation amplitude.*
The dashed lines show simulations, where in the case of ^{57}Fe-Y122H the hyperfine parameters for the simulation of the CW-ENDOR spectrum were used. The inhomogeneous EPR line width for the simulations is 3.0 mT for both cases. The line shape is Gaussian.

3.3 CW and Pulsed ENDOR Studies

3.3.1 Introduction

ENDOR techniques are frequently applied in order to resolve hyperfine coupling tensors from nuclear interactions with an electron spin. The NMR transitions are not detected directly, but via a change of the EPR absorption. The increase in spectral resolution can be up to three orders of magnitude compared with conventional EPR [156]. An accurate knowledge of the type of nucleus interacting with an electron spin as well as the strength and anisotropy of these interactions gives insight into the environment and structure of the paramagnetic center H studied here. There is important information on the nature of this center which can be revealed by ENDOR techniques:

- The isotropic Fermi contact part of the hyperfine tensor in general is proportional to the spin density at the corresponding nucleus and therefore yields information on the type of the paramagnetic species, the distribution of the electron wave function over a molecule and the near environment of a EPR active center. The spin density at the iron atoms is expected to provide information on the nature of center H, especially on the oxidation states, and spin state as well, of the iron atoms.

- The anisotropic part of the tensor gives information on the structure of the molecule, or - if the structure is known - on the type and, in the case of ^{57}Fe, oxidation state of the nucleus.

In this chapter ENDOR measurements are reported for center H in R2-Y122H. As discussed in the preceding chapter, the g-anisotropy is not resolved at X-band. Therefore it is not possible to detect an orientation selective X-band ENDOR over the g-tensor envelope. However, ^{57}Fe ENDOR will provide valuable information on the oxidation state of the iron nuclei, and thus on the type of the paramagnetic center. The ligand sphere is probed by the detection of nitrogen and proton ENDOR. Thus a detailed analysis of the electronic structure and the type of the paramagnetic center is provided.

3.3.2 ^{57}Fe Tensors in Di-iron Centers - Nature of Center H

Previous Work Done on Paramagnetic Di-iron Centers: Fe(III)Fe(IV) and Fe(II)Fe(III)

^{57}Fe ENDOR is expected to reveal valuable information on the electronic structure of center H. However, before the results of the measurements on center H are presented, a short review of similar studies on paramagnetic di-iron centers previously reported is given. It will be important to compare these measurements with the results for center H.

The $S = 1/2$ ground state of intermediate X in the mutant R2-Y122F exhibits an isotropic singlet of 1.8 mT width in X-band EPR. Q-band spectra, however, reveal a slight g-factor anisotropy with the principal values 2.007, 1.999 and 1.994 [84]. Reconstitution in ^{57}Fe results in one clearly resolved ^{57}Fe hyperfine coupling at X-band, while orientation selective pulsed Q-band ENDOR made it possible to identify two ^{57}Fe tensors, one nearly isotropic around 73 MHz and another axial tensor with $A_\perp = 36.8$ and $A_\parallel = 27.5$ MHz [84]. Since the spherically symmetric ^6S ground state of Fe(III) is expected to cause a rather isotropic coupling, the axial tensor is assigned to the Fe(IV) ion. The intrinsic couplings have been calculated, which are related to the measured coupling by:

$$A_{Fe(III)} = -\frac{4}{3}A_{in},$$

$$A_{Fe(IV)} = \frac{7}{3}A_{in}$$

The intrinsic couplings A_{in} have been compared with known couplings of similarly ligated mononuclear iron ions, which yielded a good agreement, and thus supports the model of a mixed-valence Fe(III)Fe(IV) site [84]. $^{1,2}H$ Q-band ENDOR in combination with D_2O exchange, as well as ^{17}O Q-band ENDOR after reconstitution with $^{17}O_2$ and/or $H_2^{17}O$ have been applied to X revealing an exchangable H_2O ligand and a single μ-oxo bridge both derived from dioxygen during the reconstitution reaction [68, 85, 86]. In an EXAFS study a very short Fe-Fe distance of 2.5 Å was detected (for comparison: Fe-Fe = 3.3 Å in the diferric cluster) suggesting at least three bridging ligands between the iron atoms [87]. Several model Fe(III)Fe(IV) compounds have been investigated by rapid freeze quench (RFQ)-EPR , ^{57}Fe ENDOR and Mössbauer spectroscopy exhibiting all g values and ^{57}Fe couplings similar

compound	$\mathbf{A_{Fe(III)}}$ (MHz)	$\mathbf{A_{Fe(IV)/Fe(II)}}$ (MHz)
Fe(III)Fe(IV) type		
X in Y122F [84]	-74.2	36.8
	-73.2	36.8
	-74.2	27.5
$Fe_2(O_2)(6MeTPA)_2$ [88, 89]	-64.5	36.5
		36.5
		20
Fe(II)Fe(III) type		
Q in MMO [91]	-75	30
	-75	32
	-70	26
MMO in	62	38
M. capsulatus [83]	68	38
	76	-

Table 3.5: *List of experimentally determined ^{57}Fe hyperfine coupling tensor principal values for different Fe(III)Fe(IV) and Fe(II)Fe(III) centers in proteins and model systems.*

to the ones found for X (see Table 3.5) [88–91].

Another type of mixed-valence di-iron center, the Fe(II)Fe(III) center in the hydroxylase component of MMO, has been characterized very well employing orientation selective ^{14}N, ^{15}N, $^{1,2}H$, and ^{57}Fe ENDOR [83, 96, 97]. The ^{57}Fe tensors behave characteristically for Fe(II)Fe(III) type mixed valence di-iron centers: Fe(II) exhibits an axial tensor due to its non-spherical spin distribution. The spin projection coefficients, however, are the same for Fe(II)Fe(III) and Fe(III)Fe(IV) (see chapter 2.7).

Summarizing, it is evident, that there is a lot of information one can extract from ^{57}Fe-ENDOR about the electronic structure of a paramagnetic di-iron center:

- First of all, the nature of the paramagnetic center can be confirmed as well as

the number of iron nuclei involved by testing the spin distribution at the iron nuclei via the isotropic hyperfine interaction.

- Secondly, the degree of anisotropy of the ^{57}Fe hyperfine coupling tensor as well as the spin projection coefficients derivable from the isotropic tensor components in case of dinuclear iron centers give insight into the valency state of the iron atoms involved [134]: While Fe(III) typically exhibits a nearly isotropic hyperfine coupling tensor due to the spherical charge distribution of the ^6S ground state, Fe(II) and Fe(IV) coupling tensors are expected to show an axial anisotropy [118, 135].

- The spin projection coefficients for the hyperfine values yield insight into the coupling scheme between the atoms of the iron cluster [135]. ^{57}Fe ENDOR information is very helpful for determining these coefficients and thus the spin density distribution within the cluster. It has been applied previously to gain insight into the structure of di- and polynuclear Fe clusters [84, 136].

Own Experiments on the Fe(III)Fe(IV) Center Intermediate X in R2-Y122F

For comparison with center H, intermediate X was investigated in this work using the same experimental techniques of CW-ENDOR in X-band. The ^{57}Fe hyperfine coupling tensor was recorded for X in a sample of mutant Y122F freeze quenched at a time of 300 ms after providing it with $^{57}Fe^{2+}$ ascorbate for the reconstitution reaction. At conventional X-band EPR one nearly isotropic hyperfine coupling of around 0.2 mT is resolved and leads to a splitting of the line, whereas another smaller hyperfine coupling only causes an asymmetric line broadening (see Figure 3.9).

The technique used was CW ENDOR at a temperature of 9 K and at a microwave power of 8 mW in the saturation region, which is required for the ENDOR effect (see chapter 2). ^{57}Fe iron nuclei exhibit I=1/2 and a rather small nuclear g-factor of 0.1806 which causes a line splitting of around 0.9 MHz at X-band frequencies ($=2\nu_{Zeeman}$). Large couplings therefore appear centered around the position of A/2, as explained in chapter 2.

Figure 3.13 displays the ENDOR spectrum for an X-band sample of intermediate X

in R2-Y122F reconstituted with ^{57}Fe. Around 37 MHz, ENDOR lines are observed, which belong to a ^{57}Fe coupling. Its fairly isotropic coupling around 70 MHz corresponds to the larger coupling responsible for the splitting observed in the CW EPR spectrum. The tensor components of this coupling are resolved well. The second, anisotropic coupling, is mainly hidden under the proton matrix. A simulation for the large coupling is shown in 3.13. The parameters are given in Table 3.6.

For the simulation of the powder ENDOR spectra the program SPLEEN was employed. The algorithm is described in reference [137]. The program calculates EPR transitions up to second order perturbation theory for each orientation and the corresponding ENDOR frequencies of the coupled nuclei. The orientations which contribute to the EPR absorption at the given field point are determined and convoluted with the EPR line shape and line width. The ENDOR transition frequencies are calculated for these orientations. A weighted convolution of these transitions with the ENDOR line width yields the simulated spectrum. An arbitrary number of hyperfine tensors may be included for simulation, for each of them 6 parameters can be provided in the input files, the three tensor principal components and three Euler angles relating the axes sytem in which the hf-tensor is diagonal to the axes system of the g-tensor. For center X, the best simulation is achieved when the hyperfine tensor axes system is chosen collinear with the g-tensor system with the orientation of the A tensor principal axes as proposed in reference [84]. The large, well resolved ^{57}Fe tensor (Fe_A) was simulated to fit the CW-ENDOR spectrum, for the smaller, axial tensor (Fe_B) numbers already published by the group of Brian Hoffman were used [84]. The smaller coupling assigned to Fe(IV) is mostly hidden under the hydrogen transitions centered around 13.9 MHz and thus could not be satisfactorily simulated, though it previously could be fully resolved by Q-band pulsed ENDOR due to the shift in the Zeeman frequencies at different frequency bands. The hyperfine components for the large coupling assigned to Fe(III) coincide sufficiently with the ones found by Q-band ENDOR [84]. Both are listed in the Table 3.6.

^{57}Fe ENDOR Experiments on Center H in R2-Y122H

After the measurements on intermediate X a 2.1 mM sample ^{57}Fe Y122H and 1.5 mM ^{56}Fe Y122H was investigated by CW- and pulsed ENDOR measurements [107]. The CW-ENDOR parameters have thoroughly been adjusted to 8 mW mi-

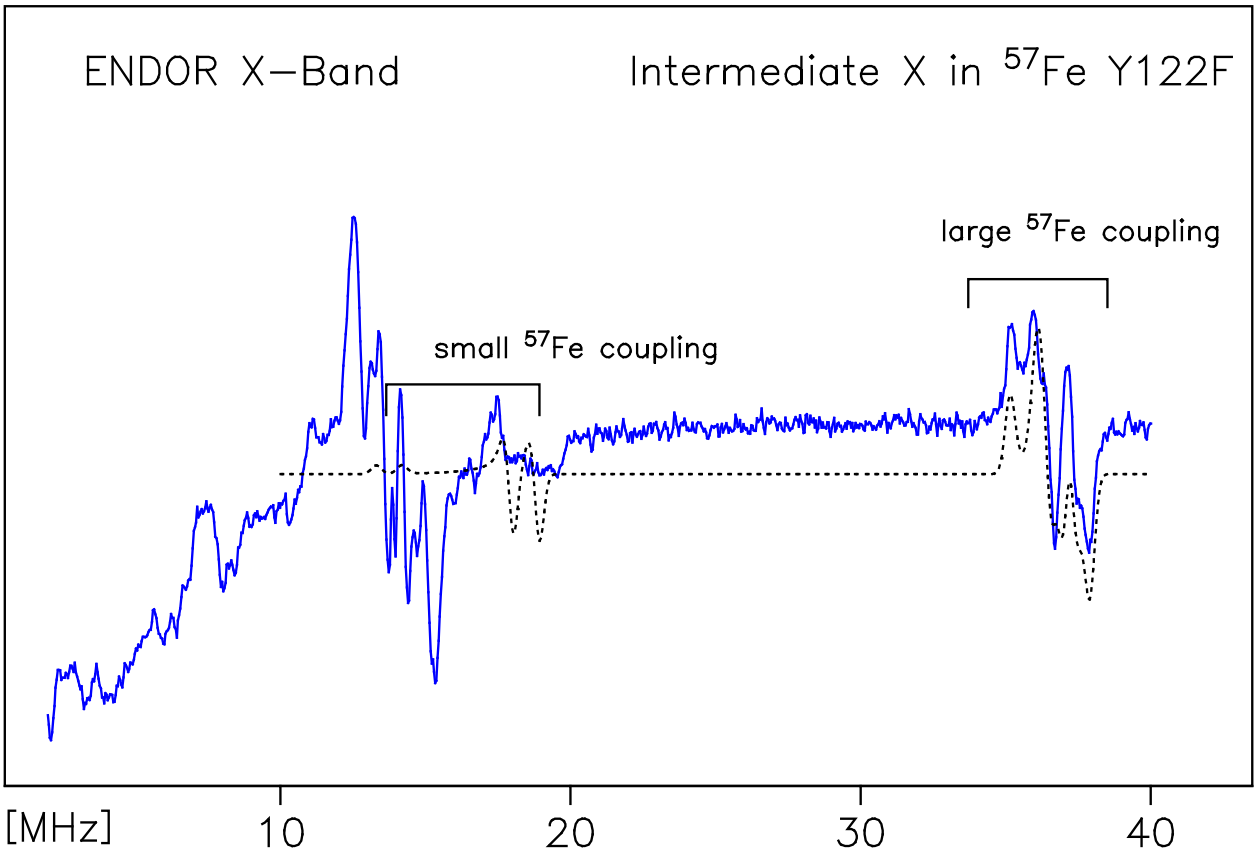

Figure 3.13: *X-band CW-ENDOR of the Fe(III)Fe(IV) center in intermediate X in E. coli RNR R2-Y122F reconstituted in ^{57}Fe ascorbate and freeze quenched at 300 ms. The ^{57}Fe transitions are marked. The transitions of the smaller ^{57}Fe coupling are mainly hidden under the proton resonances at the left side of the figure. The simulation of the respective tensor for this coupling therefore is based on literature data [84].*
Experimental conditions: microwave power: 8 mW; radiofrequency power: 100-150 W, modulation amplitude: ± 140 kHz, total accumulation time: 4.5 h;
The dashed line displays the best simulation of the large ^{57}Fe hyperfine tensor obtained by SPLEEN (see text).

crowave power, where the center already saturates at temperatures around 10 K. The optimal ENDOR signal amplitudes were found at a temperature of 9 K. Spectra were measured in a range of 0.5 to 50.5 MHz at a microwave frequency of 9.1 GHz. The static magnetic field was set to the maximum of the absorption EPR line. For the pulse sequence in the pulsed ENDOR experiments the Davies technique was chosen. For the repetition rate of the pulse sequence, T_1 is to be taken into account. A value of 100 Hz yielded the best signal-to-noise ratio in a given accumulation time interval at 9 K.

Figure 3.14 shows the pulsed ENDOR spectra of center H in ^{56}Fe (B) and ^{57}Fe Y122H (A). The spectrum of wild type R2 containing Y122• has been measured under the same conditions and is shown in Figure 3.14 (C). Both spectra, Figure 3.14 A and B show resonances from proton (12-18 MHz) and ^{14}N (4-10 MHz) nuclei. The broad features near 26 MHz and 42 MHz in the spectrum of ^{56}Fe R2-Y122H are attributed to the tyrosyl radical from residual wild type R2: This is verfied by comparison with the spectrum of wild type R2 in Figure 3.14 C. In the CW and pulsed ENDOR spectra of ^{57}Fe Y122H (Figure 3.14 a and A), however, two additional resonances appear around 25 MHz and 35 MHz, which are absent in the spectra for ^{56}Fe R2-Y122H (3.14 b and B). They belong to two different iron nuclei with slightly anisotropic hyperfine coupling tensors. The tensor components are fully resolved in the first derivative CW-ENDOR spectrum.

The CW ENDOR spectrum, in which the details of the tensor components are better resolved than in the pulsed ENDOR spectra, was simulated using the SPLEEN program. The Table 3.6 lists the parameters for a simulation of both hyperfine coupling tensors. In the simulation only absolute values were used for the tensor components since the ordinary CW ENDOR technique cannot discriminate between negative and positive polarization.

The tensor components are each split by 2ν ^{57}Fe, which at X-band frequency is 0.9 MHz (see equation 2.12 in section 2.4). The two ^{57}Fe hyperfine couplings confirm that H is a di-iron cluster similar to intermediate X. The spins on the two iron atoms couple to $S = 1/2$. The comparison of the g-values and ^{57}Fe hf tensors from center H with respective data for other mixed valence di-iron centers, as reviewed earlier in this section, leads to important differences: The larger ^{57}Fe hf tensors of H has components comparable in size to the ones reported for Fe(III) in Fe(III)Fe(IV) as

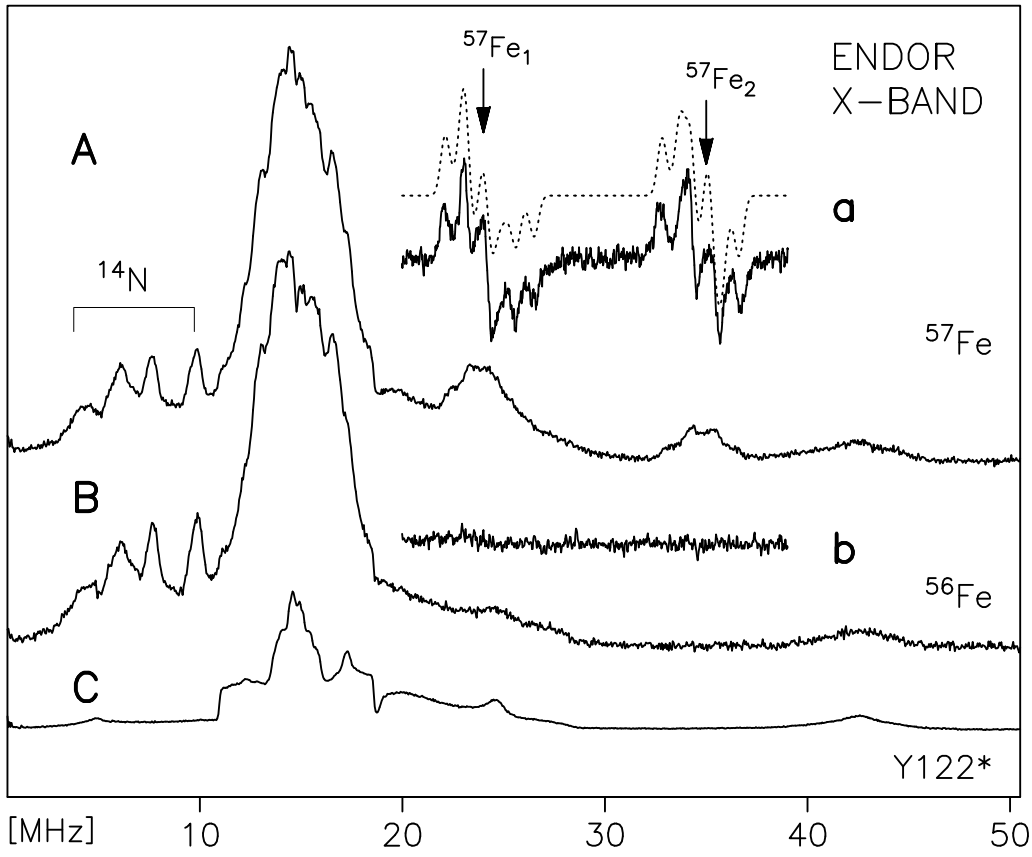

Figure 3.14: *X-band pulsed Davies ENDOR at T=10 K of center H in E. coli RNR R2-Y122H;* **A***:* ^{57}*Fe-Y122H (2.1 mM),* **B***:* ^{56}*Fe-Y122H (1.5 mM),* **C***: Y122• in wild type R2 (1.0 mM);*

Experimental conditions: microwave pulses: 192, 96, 192 ns, rf pulse: 8 µs, accumulation time: 10 h (A,B), 0.5 h (C);

Inserts: X-band CW-ENDOR spectra at T=8 K, **a***:* ^{57}*Fe-Y122H (2.1 mM),* **b***:* ^{56}*Fe-Y122H (1.5 mM);*

Experimental conditions: microwave power: 8 mW; radiofrequency power: 100-150 W, modulation frequency: 12.5 kHz, modulation amplitude: ± 150 kHz, total accumulation time: 3 h;

The dotted spectra show simulations of the ^{57}*Fe-ENDOR signal (see text).*

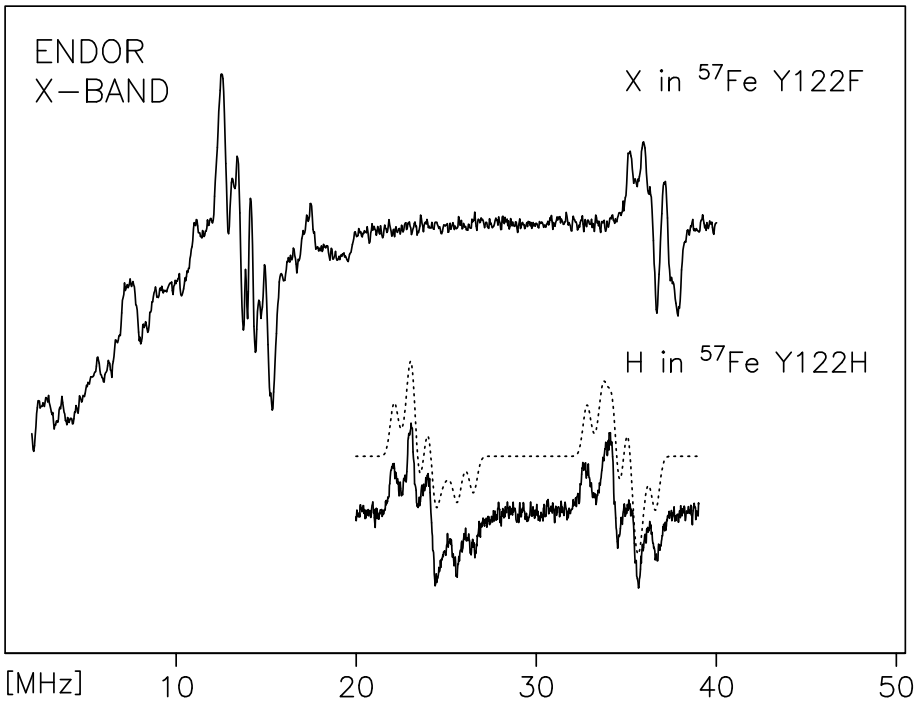

Figure 3.15: *X-band CW-ENDOR spectra of intermediate X in E. coli RNR R2-Y122F reconstituted with ^{57}Fe ascorbate and freeze quenched at 300 ms, and center H in mutant R2-Y122H from cells grown in ^{57}Fe medium.*
Experimental conditions: see Figure 3.13 and 3.14 of this section;

well as Fe(III)Fe(II). The smaller ^{57}Fe hf tensor in H, however, behaves much more isotropic than the corresponding tensor measured for the Fe(IV) in intermediate X. But also the isotropic part of this tensor in H is significantly larger than the one that was measured for center X or other mixed valence di-iron clusters [108] (see preceding sections). The g-tensor components, on the other hand, as was discusssed earlier in this thesis, resemble much more a Fe(III)Fe(IV) center [108] rather than a Fe(III)Fe(II) center.

Proposal for the Type of the Paramagnetic Di-iron Site in Center H

The isotropic parts due to the Fermi contact interaction for both ^{57}Fe tensors in center H are:

$$Fe_A: \quad a_{iso} = 69.6\, MHz$$

$$Fe_B: \quad a_{iso} = 48.3\, MHz$$

Hyperfine coupling tensor components (in MHz) used for the simulation of ^{57}Fe CW ENDOR spectrum of H in Y122H and intermediate X			
		Center H[c]	Intermediate X[b]
Fe_1	A_{xx}	72.5 ± 0.1	-74.5 ± 0.1
	A_{yy}	69.7 ± 0.1	-71.3 ± 0.1
	A_{zz}	66.6 ± 0.1	-73.7 ± 0.2
Fe_2	A_{xx}	52.1 ± 0.1	27.5^a
	A_{yy}	47.6 ± 0.1	36.8^a
	A_{zz}	45.1 ± 0.1	36.8^a

Table 3.6: *^{57}Fe hyperfine coupling tensors from the simulation of the ENDOR spectra of center H (mutant R2-Y122H) and intermediate X (in mutant Y122F). A Gaussian line shape was used for the simulation with a ENDOR line width of 0.3 MHz for center H and 0.3 MHz for intermediate X*

[a] The values are taken from reference [84].

[b] The hyperfine tensor axis system of both ^{57}Fe tensors is collinear with the g-tensor. The information about the orientation and sign of the tensor components is taken from reference [84].

[c] The tensor components are absolute values and ordered with decreasing value. No correspondence between A_{ii} and G_{ii} (i=x,y,z) could be obtained from the experiments performed at X-band. The measurement yielded no information concerning sign and orientation of the components.

Postulating an Fe(III)Fe(IV) di-iron complex, the following equations are applied $\mathbf{A}(Fe^{III}) = 7/3\mathbf{a}_{in}$ (Fe^{III}) and $\mathbf{A}(Fe^{IV}) = -4/3\mathbf{a}_{in}$ (Fe^{IV}), where $\mathbf{a}_{in}$ are the intrinsic couplings and the appropriate spin projection coefficients -4/3 and 7/3 are used (see chapter 2.7). The intrinsic couplings then become:

$$a_{in}(Fe^{III}) = 29.8\,MHz,$$

$$a_{in}(Fe^{IV}) = 36.2\,MHz$$

For the isotropic Fermi contact term of mononuclear octahedral Fe(III) a theoretical value of around -22 T $\times g_n\beta_n$ is reported and also confirmed by experimental results [138–140]. The intrinsic value for the proposed Fe(III) site lies in the same order of magnitude. The intrinsic coupling for the Fe_2 site, however, differs considerably from the values calculated for intermediate X (-25.3 MHz) and a Fe(III)Fe(IV) model compound (-23.2 MHz) [88].

The anisotropies of the Fe(IV) tensor which were measured in intermediate X [84] and model compounds [88] are attributed mainly to magnetic dipolar couplings [84](see chapter 2.7). In center H the Fe_1 site (definitions of the site see Table 3.6) exhibits anisotropy of 4%, the Fe_2 site of 8%, respectively. For comparison, the Fe_1 tensor in intermediate X has 3% anisotropy, whereas the axially symmetric tensor of the Fe_2 site exhibits 18% anisotropy, considerably larger than the Fe_2 site in H. Due to the spherical charge and spin distribution of a half filled d shell where every d orbital is singly occupied, the tensor for an Fe(III) oxidation state is expected to be almost isotropic, while Fe(II) and Fe(IV) either miss an electron in the d shell or possess an additional one, therefore exhibiting a non-spherical ground state spin distribution. The hyperfine tensors are then expected to exhibit rather large anisotropy [88]. Magnetic resonance as well as Mössbauer measurements on mixed valence di-iron centers confirm this behaviour (see Table 3.5). The anisotropy of the ^{57}Fe hf-tensor of Fe(IV) in the model compounds is even larger than found for X which led to the assumption of an additional delocalization of the spin in intermediate X over the ligands [84]. For center H, we would have to postulate a considerably higher degree of delocalization in order to hold the model Fe(III)Fe(IV). Considering this, it becomes difficult to assign site 1 in center H to a pure Fe(IV) oxidation state. The anisotropy at this site fits a Fe(III) formal oxidation state much better.

Therefore, another type of center, which was originally proposed also for X [142], is considered here. It consists of three exchange-coupled spins, two $S_1 = 5/2$, $S_2 = 5/2$ at two Fe(III) atoms and a further spin $S_3 = 1/2$, which is expected to sit on an amino acid ligand.

Three spins in the strong exchange limit (which means that the exchange interaction between the spins is considerably larger than the dipolar interaction, see section 2.7.2) are commonly described by a theoretical three spin coupling model [135, 142]. The outline of this model given here is based on reference [141]: Two spins S_2 and S_3 are coupled to an intermediate spin S_{23}, which then builds the final state when coupled to S_1 according to the rules of angular momentum addition. There exist two different intermediate spin states $|S_{23}; SM >$ which both couple with $|S_1 >$ to a $S = 1/2$ ground state: $|2; 1/2, 1/2 >$ represents an antiferromagnetic coupling between the radical and the adjacent iron spin, $|3; 1/2, 1/2 >$ a ferromagnetic coupling. In chapter 2.7 a spin coupling model for two spins was introduced and formula for the respective spin projection coefficients have been given. In the three spin coupling model this coupling scheme is applied twice, once to couple S_2 and S_3 and finally to couple S_{23} and S_1. The formula for the spin projection coefficients for the first coupling is (at the example of the antiferromagnetic case) [77]:

$$\begin{aligned} c_{23,1} &= \frac{S_{23}(S_{23}+1) - S_3(S_3+1) + S_2(S_2+1)}{2S_{23}(S_{23}+1)} \\ c_{23,2} &= \frac{S_{23}(S_{23}+1) + S_3(S_3+1) - S_2(S_2+1)}{2S_{23}(S_{23}+1)} \end{aligned} \tag{3.4}$$

and for the second coupling:

$$\begin{aligned} c_1 &= \frac{S(S+1) - S_{23}(S_{23}+1) + S_1(S_1+1)}{2S(S+1)} \\ c_2 &= c_{23,1}\frac{S(S+1) + S_{23}(S_{23}+1) - S_1(S_1+1)}{2S(S+1)} \\ c_3 &= c_{23,2}\frac{S(S+1) + S_{23}(S_{23}+1) - S_1(S_1+1)}{2S(S+1)} \end{aligned} \tag{3.5}$$

The formulas for the ferromagnetic case are similar. In the case of antiferromagnetic coupling S_{23}=2 and the spin projection coefficients are:

$$c_1 = 7/3, \quad c_2 = -14/9, \quad c_3 = 2/9.$$

In the case of ferromagnetic coupling (S_{23}=3):

$$c_1 = -5/3, \quad c_2 = 20/9, \quad c_3 = 4/9.$$

In the general case, however, the final ground state consists of an admixture out of these two states:

$$|\psi >= \sqrt{1-\alpha^2}\ |2;1/2,1/2> -\alpha\ |3;1/2,1/2> \tag{3.6}$$

The so-called mixing coefficient α has values between -1 and 1 and depends upon the exchange coupling constants J_{12}, J_{23} and J_{13} connecting the three spins. $|\psi >$ has to be normalized, which is guaranteed by the coefficients in the sum of equation 3.6 as long as $|2;1/2,1/2>$ and $|3;1/2,1/2>$ are normalized. The measured isotropic hyperfine coupling constants A_i depend on their intrinsic values a_i and the spin projection coefficients $<\psi|S_{iz}|\psi>$, $i = 1, 2, 3$:

$$A_i = 2a_i <\psi|S_{iz}|\psi> \tag{3.7}$$

The spin projection coefficients are the expectation values taken between the S_z operator for the three different spins and the ground state $|\psi >$. Using equation 3.6 and the formulas for the spin projection coefficients from equations 3.4 and 3.5, a general expression for the spin projection coefficients as a function of α is obtained [141]:

$$<\psi|S_{1z}|\psi >= 7/6 - 2\alpha^2, \tag{3.8}$$

$$<\psi|S_{2z}|\psi >= 1/9(17\alpha^2 + \sqrt{35}\alpha\sqrt{1-\alpha^2} - 7), \tag{3.9}$$

$$<\psi|S_{3z}|\psi >= 1/9(\alpha^2 - \sqrt{35}\alpha\sqrt{1-\alpha^2} + 1) \tag{3.10}$$

For the case of center H the three spin projection coefficients were plotted versus the mixing coefficient α for intrinsic hyperfine coupling constants chosen in a range from -30 to -35 MHz. A possible plot with $a_{in,1}$=-31.5 MHz and $a_{in,2}$=-34.5 MHz is shown in 3.16. For $\alpha = 1$ the coupling is ferromagnetic (the same applies for α = -1, which differs from $\alpha = 1$ only in a phase factor (see equation 3.6) and therefore is not considered here any more), while at $\alpha = 0$ antiferromagnetic coupling is obtained. The expectation values are not symmetric around $\alpha = 0$. In particular, $<\psi|S_{3z}|\psi >$ changes its sign. Both isotropic ^{57}Fe hyperfine couplings are indicated in the plot.

The measured isotropic values are in the range of the couplings predicted by the model at α=0 (antiferromagnetic coupling) and α=1 (ferromagnetic coupling).

Interestingly, the isotropic couplings are exchanged between the two Fe(III) for the ferromagnetic solution compared with the antiferromagnetic solution. The model gives the following isotropic couplings for the two iron atoms:
Antiferromagnetic coupling ($\alpha = 0$):

$$A_{iso,Fe(III)_1} = 69\ MHz,\ A_{iso,Fe(III)_2} = 48\ MHz$$

Ferromagnetic coupling ($\alpha = 1$):

$$A_{iso,Fe(III)_1} = 69\ MHz,\ A_{iso,Fe(III)_2} = 52\ MHz$$

Considering the roughness of this model in which the dipolar interactions between the spins are neglected, both values are in good agreement with the isotropic couplings for center H from the ^{57}Fe ENDOR measurements.

Summary

Finally summarizing, two models were discussed for center H: A Fe(III)Fe(IV) di-iron cluster may very well explain the range of the measured g-tensor principal values, and also the behaviour of the isotropic part of the ^{57}Fe coupling tensor. However, it predicts a considerable anisotropy for the hyperfine coupling to the ferryl iron in contradiction to the measured data for center H. In the three spin model both ^{57}Fe couplings can be considered as fairly isotropic due to the +III oxidation state for the iron atoms. The absolute sizes of the couplings can be reproduced by the model as well.

The next question is the explanation of the third paramagnetic species needed for this model. Since the coupling to the iron center has to be large, its site has to be very close to the two irons. The postulation of a ligand radical therefore is reasonable. The possible position of this ligand radical needs to be discussed, however [108].

Most support can be found for the proposal of the phenylalanine residue F208, which is close to the di-iron site [109], as site of the ligand radical for the following reasons:

- Reference [132] reports the generation and characterization of relatively stable (around 1 hour) phenoxyl radical analogues ligated to a mononuclear iron(III) in an octahedral Tris(phenolato)iron(III) complex therefore giving evidence of the high stability of such a configuration.

- A hydroxylation of residue F208 to a tyrosine and subsequent iron ligation has been observed in R2 double mutant Y122F/E238A [131].
- In mutant R2-F208Y, where the phenylalanine is substituted by tyrosine, a paramagnetic species occurs, which exhibits features surprisingly similar to center H in R2-Y122H [133]. Aditionally, it was shown by growing the cells with $\beta - H^2$ labelled tyrosine, that a decrease in line width occurs. This is attributed to a H_β coupling from Y208 and suggests considerable spin density on residue Y208 [133].

Therefore the most favoured position for the ligand radical postulated in the three spin model is residue Phe208, where an oxidation and subsequent ligation to the nearest iron atom is proposed [108]. However, evidence for the hydroxylation and the spin density on the phenyl ring of F208 in R2-Y122H is still missing. The final identification of spin density on F208 in R2-Y122H by ENDOR on deuterated Phe-Y122H will be the subject of a subsequent work [107].
A remark has to be made concerning the magnitude of the spin density to be expected: The three spin coupling model predicts in both cases, the ferromagnetic and the antiferromagnetic, a fairly low spin projection coefficient for the third, S=1/2 spin (2/9 and 4/9, respectively). This is also evident from the plot in Figure 3.16. Therefore, hyperfine couplings to the H_α and H_β in the phenyl ring are expected to be in the order of 2/9 (4/9) times the coupling strengths found for ordinary phenolate radicals.

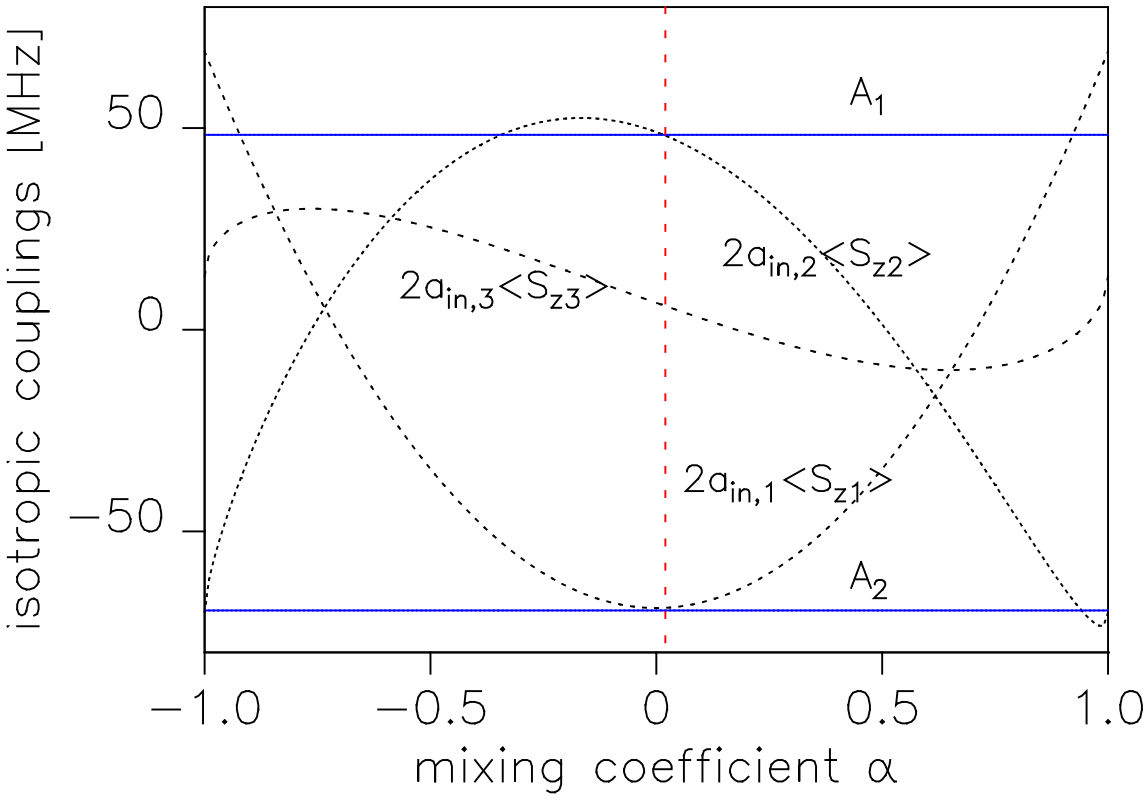

Figure 3.16: *The predicted hyperfine couplings from equation 3.7 are plotted versus the ground state mixing coefficient α for the case of three spins S_1=5/2, S_2=5/2 and S_3=1/2 according to the three spin coupling model (see text). For the calculation of the spin projection coefficients equations 3.8-3.10 are employed. The experimental values for the ^{57}Fe hyperfine couplings are shown by the solid lines. The dashed vertical line indicates the antiferromagnetic solution for the mixing coefficient, where the isotropic coupling constants predicted by the model approach the measured ones for center H (see text for further explanation).*

3.3.3 $^{14,15}N$ ENDOR on Center H in Mutant Y122H

Introduction

ENDOR techniques prove as adequate methods for getting information about the close ligand sphere of a paramagnetic metal center by detecting strength and anisotropy of the hyperfine coupling interaction of nuclei of ligands. Of particular interest in the case of metal centers are nitrogen nuclei:
In biological metal centers histidines are frequent and well-known strong ligating agents via the lone pairs of their nitrogen atoms. Nitrogen nuclei of the naturally abundant isotope ^{14}N exhibit a nuclear spin of one, thus capable of interacting with nearby electronic spins via a hyperfine interaction. Nuclear spins larger than 1/2 give rise to a quadrupole interaction: An electric field gradient at the site of the nucleus caused by a non-spherical distribution of the charge density due to the surrounding electrons leads to a splitting in the nuclear spin energy levels, if the nuclear charge distribution is non-spherical as well (as is the case for I > 1/2) [144]. For this interaction the following term needs to be added to the Hamiltonian (in frequency units)[156]:

$$H_{quadrupole} = \frac{e^2qQ}{4I(2I-1)h}(3\mathbf{I}_z^2 - I(I+1) + \eta(\mathbf{I}_x^2 - \mathbf{I}_y^2)) \tag{3.11}$$

where I refers to the nuclear spin, $\mathbf{I}_z$, $\mathbf{I}_x$, $\mathbf{I}_y$ are the corresponding spin operators, Q is the nuclear quadrupole moment, e^2qQ/h the quadrupole coupling constant and η the asymmetry parameter. The quadrupole interaction is fully described by a second rank tensor of zero trace (which means there is no isotropic part in this interaction) with principal components chosen $|V_{xx}| \leq |V_{yy}| \leq |V_{zz}|$ by convention. The requirement of zero trace actually reduces the parameter from three to two, the quadrupole constant and the asymmetry parameter, respectively:

$$\frac{e^2qQ}{h} = 2|V_{zz}|, \tag{3.12}$$

$$\eta = \frac{V_{xx} - V_{yy}}{V_{zz}} \tag{3.13}$$

Oxygen, also a well-known ligating atom, exhibits in its naturally abundant isotope ^{16}O zero nuclear spin and is therefore not detectable with magnetic resonance techniques.

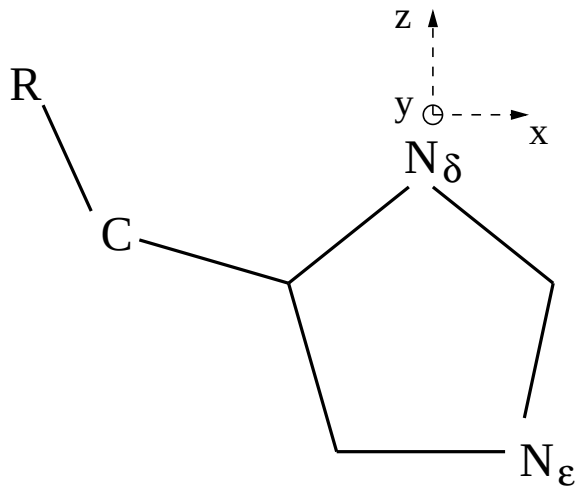

Figure 3.17: *Molecular structure of histidine. The positions of the nitrogen atoms N_δ and N_ϵ are indicated.*

Another nitrogen isotope, ^{15}N, carries a nuclear spin 1/2. It therefore also exhibits a hyperfine interaction with a nearby electron spin. The quadrupole interaction, however, is missing. The nitrogen atoms in histidines or other ligating molecules can be selectively exchanged from ^{14}N to ^{15}N. This can provide additional information on the site of the nuclear spin, since the nuclear g-factors of ^{14}N and ^{15}N differ from each other: $\frac{g(^{15}N)}{g(^{14}N)} = -1.403$. This leads to a different coupling strength, which is directly proportional to the deviation in the nuclear g-factors [143]:

$$\frac{A(^{15}N)}{A(^{14}N)} = \frac{g(^{15}N)}{g(^{14}N)} = -1.403$$

The strength of the quadrupole parameters and their orientation is characteristic for nitrogen atoms in certain environments. Histidines have two nitrogen atoms in the imidazole ring. They are labelled N_δ and N_ϵ by convention. They are shown in Figure 3.17.

In the case of center H in mutant Y122H, two large nitrogen couplings are expected, provided that the assumption is true that center H has a similar environment as the Fe(III)Fe(III) center of the 97% Y122H protein studied by X-ray: Both couplings then derive from ligating histidine N_δ nitrogens, belonging to H118 and H241, respectively (see Figure 3.32).

Intensive ESEEM and ENDOR studies have been reported in the literature, which investigated the typical range of quadrupole parameters exhibited by the two nitrogen atoms in histidines:

- ENDOR and pulsed EPR studies on the quinone anion radicals in the bacterial photosynthetic reaction center revealed the quadrupole parameters for ligating histidine N_δ and even backbone nitrogen [149].
- An investigation of the direct and distant ligation sphere of the copper center in azurin crystals by means of W-band ENDOR and W-band ESEEM measurements also revealed the quadrupole parameters and the orientation of the quadrupole tensor for ligating N_δ and non-ligating N_ϵ, as well as backbone nitrogen [147, 148].
- The quadrupole parameters of imidazole N_ϵ ligated to iron in heme complexes and proteins are well-known thanks to intensive studies [153, 154]

Also the hyperfine coupling strength and the orientation of the corresponding tensors for directly coordinating and non-coordinating nitrogen atoms were reported in these studies. In most cases of metal centers in proteins, N_δ of histidine is coordinated to the metal center [83, 143, 147, 148]. However, there exist reports on a direct coordination of backbone nitrogens, for example in the case of cupric peptide complexes [152]. Also coordinations of the N_ϵ nitrogen are reported [149].

^{14}N ENDOR on Center H in Y122H

X-band CW ENDOR spectra have been taken for a 2 mM sample Y122H protein from cells grown in LB medium. The ENDOR parameters have thoroughly been adjusted to 8 mW microwave power, where the center H saturates at temperatures around 10 K. The optimal relaxation behaviour for a large ENDOR signal was found for a temperature of 9 K. Spectra were measured in a range of 0.5 to 30.5 MHz at a microwave frequency of 9.1 GHz. The static magnetic field was set to the maximum of the EPR absorption line. The obtained ENDOR spectrum is shown in Figure 3.18 A. Around 13.9 MHz, the Zeeman frequency of hydrogen nuclei at 9.1 GHz, one clearly sees a proton matrix line and several small proton couplings, all of them smaller than 7 MHz. They will be discussed in the next section. At an rf frequency range below 10 MHz, however, altogether 4 ENDOR lines are resolved.
Nitrogen nuclei exhibit a smaller Zeeman splitting than hydrogen protons: Their

Zeeman frequency $\nu_{N_{14}}$ becomes 1 MHz at X-band frequency. For large hyperfine coupling constants A the resonance positions then occur symmetric around A/2 separated by $2\nu_{N_{14}}$=2 MHz (see equation 2.12). The four lines in the low frequency region, between 4-10 MHz, indeed exhibit a pairwise distance of 2 MHz.
To make sure, however, that the resonances belong to nitrogen atoms, spectra were taken in two different ENDOR cavities exhibiting a slightly different microwave resonance frequency. The strength of the Zeeman interaction increases proportionally to the microwave frequency, the hyperfine splittings, however, do not depend upon this frequency (to first order). Thus proton lines which are centered around ν_H will shift, while the center of the nitrogen resonances will not be effected. The splitting of the nitrogen lines, however, which is proportional to $\nu_{N_{14}}$, will change with the different microwave frequency. This shift is by a factor $\nu_{N_{14}}/\nu_H \approx 1/14$ smaller than the shift of the proton transitions and the shifts of the proton and the nitrogen resonances can be clearly distinguished from each other.

The spectra in Figure 3.18 show a positive result: Indeed, the shift of the four resonances at 9.9, 7.9, 6.1 and 4.1 MHz, respectively, can be neglected compared to the shift of the proton ENDOR lines around 13.9 MHz. They therefore belong to nitrogens. The lines at 9.9 and 7.9 MHz are attributed to one nitrogen atom with a approximate coupling constant of 2×8.9 MHz = 17.8 MHz (N_1) and the lines at 6.1 and 4.1 MHz to another nitrogen atom with a coupling constant around 2×5.1 MHz = 10.2 MHz (N_2). More exact values for the hf coupling tensor of the nitrogen atoms are achieved by simulations, which include the effects of the quadrupole interaction. They are reported below.

It is instructive to compare the spectra with measurements for a similar center, for example X. Thus, CW ENDOR spectra were taken for both intermediate X of mutant *E. coli* R2-Y122F, and mutant mouse protein Y177C. The spectra are shown in Figure 3.19 together with the one for center H.

As indicated by the arrows in Figure 3.19 one nitrogen coupling is resolved for intermediate X. (Two nitrogen couplings are expected for X, but the second coupling could not be resolved in the ENDOR measurements). Despite of the bad signal/noise ratio of the Y177C sample due to a rather low concentration of X, it is evident that X in mouse as well as *E. coli* R2-Y122F exhibit nearly identical nitrogen couplings of approximately 13 MHz, which indicates the strong similarity of the coordination

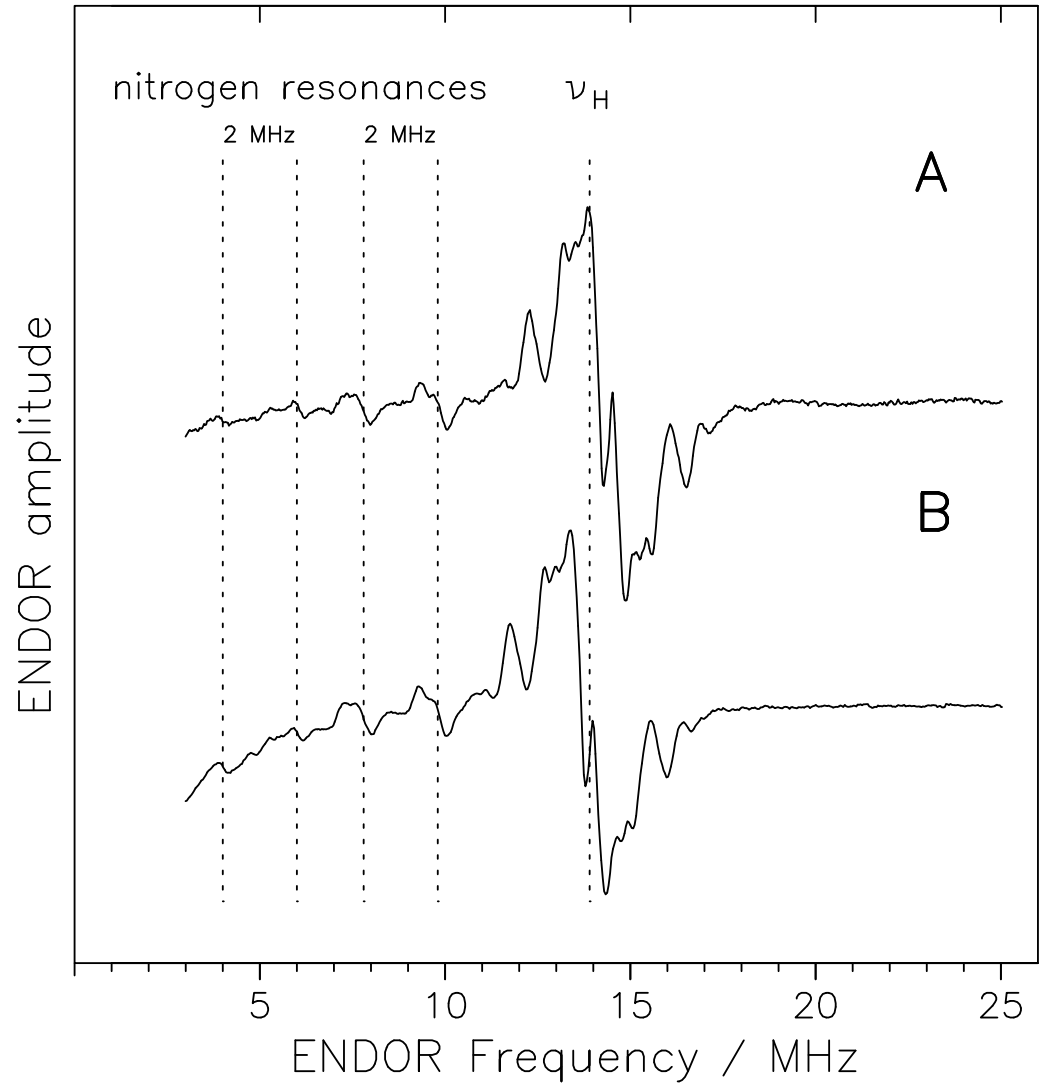

Figure 3.18: *X-band ENDOR spectra at 8 K of paramagnetic center H in E. coli R2-Y122H (2 mM)*
A: *ν=9.55 GHz*
B: *ν=9.15 GHz*
Experimental conditions: microwave power: 8 mW, radiofrequency power: 100-150 W, modulation frequency: 12.5 kHz, modulation amplitude: ±140 kHz, total accumulation time: 10 h (A), 1.5 h (B)

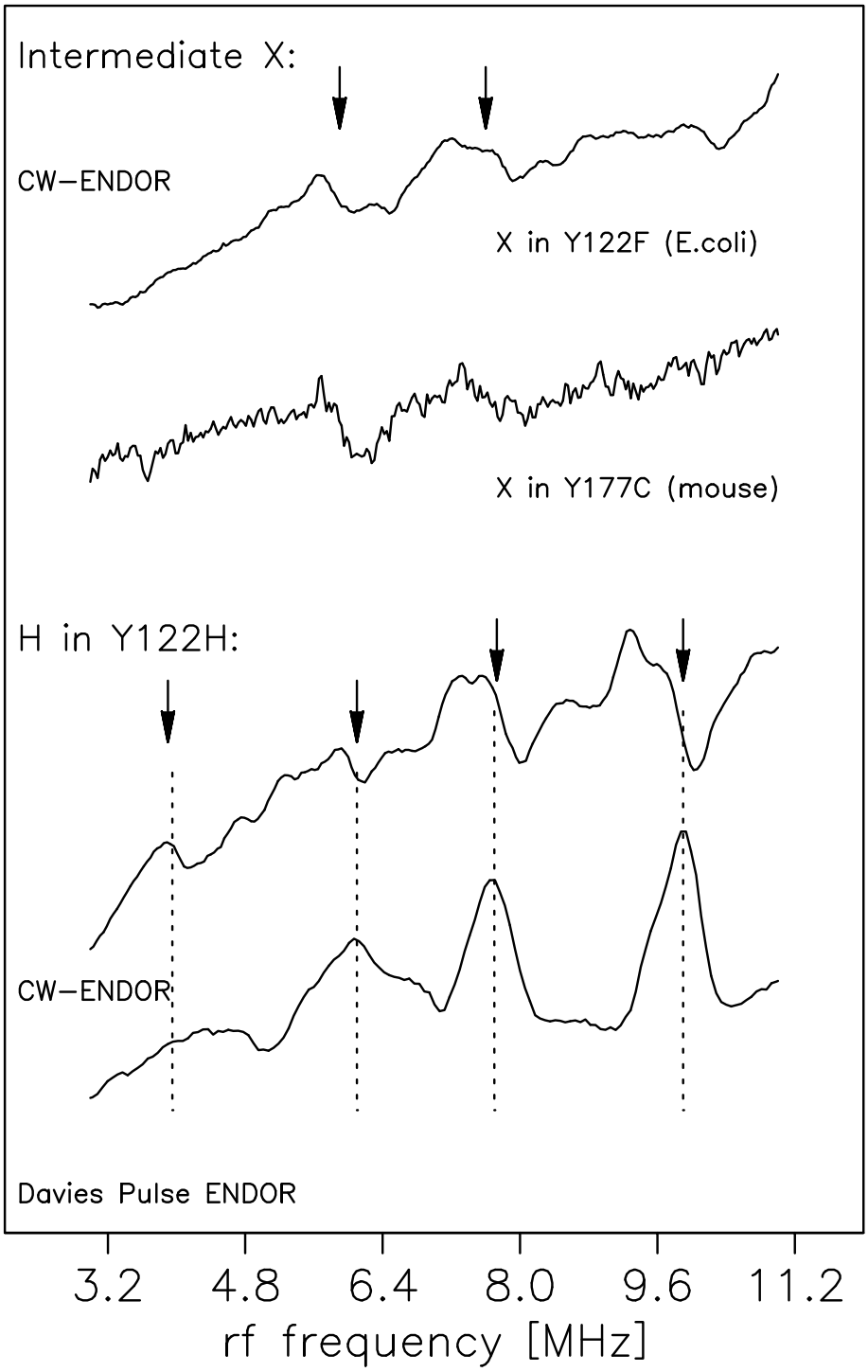

Figure 3.19: *^{14}N ENDOR resonances for X in Y122F (1 mM) freeze quenched at 300 ms, X in Y177C (0.2 mM) and H in Y122H (2 mM). Experimental conditions for all CW ENDOR spectra: temperature 9 K, microwave power: 8 mW, radiofrequency power: 100-150 W, modulation frequency: 12.5 kHz, modulation amplitude: ±140 kHz*
Davies pulsed ENDOR: temperature: 10 K, π MW pulse: 192 ns, RF pulse: 8 μs, center field: 3459 G, shot repetition time: 20.4 ms, accumulation time: 20 h

environment, as well as the spin density distribution, in both R2 mutants of different species. A similar ligation for both mutants is not self-evident, since it is known that the chemical stability of the di-iron centers in mouse and *E. coli* behaves quite different [93]. The resonance positions of the nitrogen nuclear transitions at around 5.6 and 7.6 MHz in intermediate X are in agreement with the ones shown in the Q-band ENDOR spectra of the same center taken by the group of Brian Hoffman [68].

Coordinating nitrogens typically exhibit anisotropies of around 10% [155]. Normally, even nearly isotropic ^{14}N couplings often appear - when measured in a powder sample with all possible orientations contributing - rather broad and badly resolved due to the purely anisotropic quadrupole interaction. The resonances due to the larger hyperfine coupling in center H, however, appear relatively narrow despite of the well resolved structure they show.

The pair of nitrogen resonances at low frequency in the spectrum for center H appears less well resolved in the CW ENDOR spectrum, probably due to a larger anisotropy of the hyperfine tensor components. Therefore, a pulsed ENDOR experiment for center H was undertaken. In pulsed ENDOR, the nuclear hyperfine transitions are detected in the absorption mode, thus, as explained in chapter 2, the resolution gets worse; for broader lines, however, the sensitivity is increased. Since we deal here with relatively large couplings ($>$ 8 MHz), a Davies ENDOR pulse sequence was chosen. The spectrum is shown in Figure 3.19. The shape of the low frequency nitrogen transitions is resolved better compared with the CW-ENDOR spectrum, as was expected.

^{15}N ENDOR on Center H in Y122H

In CW- as well as pulsed ENDOR studies, relatively narrow ^{14}N transitions are observed, suggesting a low hyperfine anisotropy and small quadrupole interactions. In order to separate and assign the contributions of hyperfine and quadrupole tensors to the observed nitrogen transitions, a study with ^{15}N labelled R2-Y122H was done, where the quadrupole interaction is missing and only the hyperfine interaction is contributing. The *E. coli* bacteria of R2-Y122H containing the plasmid for overexpression of Y122H protein were grown by M. Kolberg in a medium containing

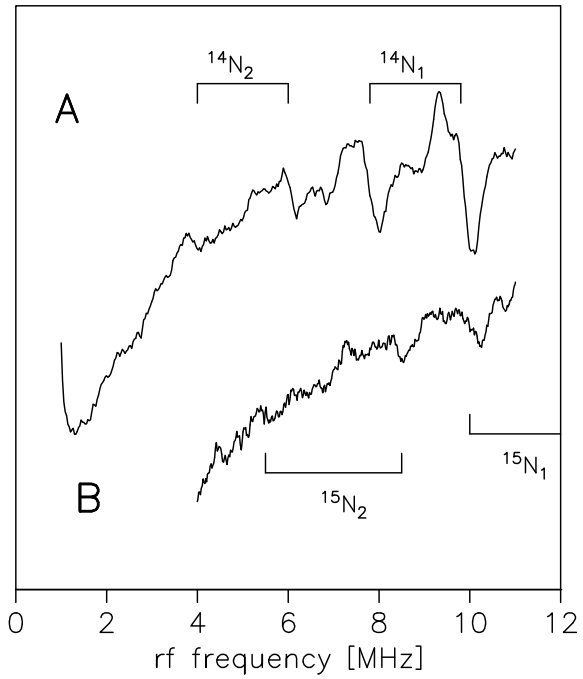

Figure 3.20: *Region of the nitrogen ENDOR transitions for*
A: ^{14}N labelled protein R2-Y122H (2 mM)
B: ^{15}N labelled protein R2-Y122H (1.3 mM)
as detected by CW-ENDOR. Resonances belonging to the same nucleus are indicated. Experimental conditions: microwave power: 8 mW; radiofrequency power: 100-150 W, modulation amplitude: ± 140 kHz, total accumulation time: 40 min (A), 9 h (B)

^{15}N labelled ammonium sulfate as the only source of nitrogen. After purification, a 1.3 mM sample of ^{15}N labelled protein Y122H was prepared and filled into X-band tubes. ENDOR spectra were taken under the same conditions as for the unlabelled ^{14}N sample. The CW ENDOR spectrum of the ^{15}N sample is shown in Figure 3.20 B and compared with the ENDOR spectrum of ^{14}N protein in 3.20 A. Despite of the low S/N ratio of the nitrogen transitions in the ^{15}N sample, it is clearly visible that the ^{14}N lines are missing and nitrogen transitions emerge at different positions.

^{15}N exhibits a different g_n as ^{14}N (1.403 larger and negative) and therefore the ENDOR transitions not only show a correspondingly larger Zeeman splitting (the line splitting is 2ν=2.9 MHz at the resonance frequency of 9.4 GHz), but also the hyperfine couplings increase by the same factor (this is evident, since g_n contributes linearly to the Fermi contact as well as the dipolar interaction; see section 2.2). The ν_+ transition (at A/2+ν_{Zeeman}) of $^{14}N_1$ is shifted from about 10 to 14 MHz for $^{15}N_1$ under the proton matrix lines and can therefore not be detected. The ν_-

Simulation parameter for the ^{15}N resonances measured for center H in Y122H by ENDOR techniques		
Hyperfine Tensor (MHz)		
	N_1	N_2
A_1	21.6 ± 0.8	12.9 ± 0.5
A_2	23.1 ± 0.8	14.0 ± 0.5
A_3	26.2 ± 1.0	14.9 ± 0.5

Table 3.7: Simulation parameters for the ^{15}N ENDOR on center H in fully ^{15}N labelled R2-Y122H protein. The line shape for the ENDOR simulations is Gaussian and the line width 0.25 MHz. The A-tensor axes were chosen parallel to the g-tensor axes. Simulations are shown in Figure 3.21.

transition of N_1, which is symmetric to ν_+, however, is observed very well. The Zeeman splitting of the lines corresponding to N_2, the nucleus with the smaller hyperfine coupling, is in good agreement with the calculated value.

^{14}N and ^{15}N ENDOR Simulations

In order to see, in what range the hyperfine and the quadrupole parameters fall and to identify, if they derive from N_δ, N_ϵ or even backbone histidine nitrogen, a simulation of the pattern was attempted. Herefore the simulation program MAGRES was applied. In this program, the resonance positions are calculated via an exact diagonalization of the spin Hamiltonian [146]. Beside the hyperfine tensor principal values, quadrupole parameters (for $I > 1/2$) and the Euler angles for each tensor with respect to the g-tensor of the electron spin are used by this program. The orientations of the hyperfine tensors were set collinear with the g-tensor for the simulation. Since the g-tensor is not resolved at X-band and the hyperfine anisotropies of the nitrogen lines are relatively small, this will only cause a negligible error.
First, the ^{15}N resonances as shown in the spectrum of Figure 3.20 were simulated, since the number of parameters is reduced to 3 for each nitrogen (the 3 components of the hyperfine tensor). The set of parameters yielding the best fit is listed in the Table 3.7.

The hyperfine parameter for the simulation of the ^{14}N spectrum were computed from the corresponding ^{15}N tensors. Additionally, two quadrupole tensors are used for a complete description of the ^{14}N ENDOR transitions. The hyperfine and quadrupole parameters which yielded the best simulation of the pattern are listed in Table 3.8. The orientation between quadrupole and hyperfine tensor was varied. The direction of the largest componenent of the quadrupole tensor was found to point with an error of $\pm 15^o$ into the direction of the lowest hyperfine tensor component for N_1 and the medium hyperfine tensor component for N_2. It is known from previous studies, that the largest component of the quadrupole tensor for ligating imidazoles lies in the molecular plane and points approximately in the direction of the z-axis (see Figure 3.17) [145]. The largest component of the hyperfine tensor of ligating nitrogen, however, is reported to lie orthogonal to the molecular plane [153]. This is in agreement with the orientation used for the simulations here.

The simulations for the CW ENDOR specta are shown in Figure 3.21, the simulation for the pulsed ENDOR spectrum in Figure 3.22. The errors in Table 3.7 indicate the parameter range within which the peaks for the simulated and the original spectrum can be regarded as coinciding.

The quadrupole parameters found for both nitrogen atoms are rather low. In reference [149–151] quadrupole parameters are reported for all three kinds of nitrogens, backbone nitrogen, histidine N_δ, and histidine N_ϵ: For the case of a backbone N-H ligating a quinone, quadrupole moments of $e^2qQ/h = 3.2$ MHz (Q_A in *Rps. viridis*) and $e^2qQ/h = 3.05$ MHz (Q_A in *Rps. sphaeroides*) are reported [149]. These values are much larger than the moments for the ligating nitrogens in center H.
Also for histidine N_ϵ a similarily high value of $e^2qQ/h = 3.36$ is reported in reference [150]. Measurements on heme irons yielded $e^2qQ/h = 2.3$ - 3.2 for ligating N_ϵ from imidazole [153, 154]. The quadrupole parameters for histidine N_δ (also N-H ligating a quinone) from references [149, 150] agree, however, very well with the values received for center H, since they lie in a range of $e^2qQ/h = 1.44$ - 1.65 and $\eta = 0.69$ - 0.91.
This suggests that the resonances indeed derive from two histidine N_δ.

It can also be excluded, that the couplings arise from non-coordinating, remote nitrogens, since it is known that for remote nitrogens the isotropic contact term of

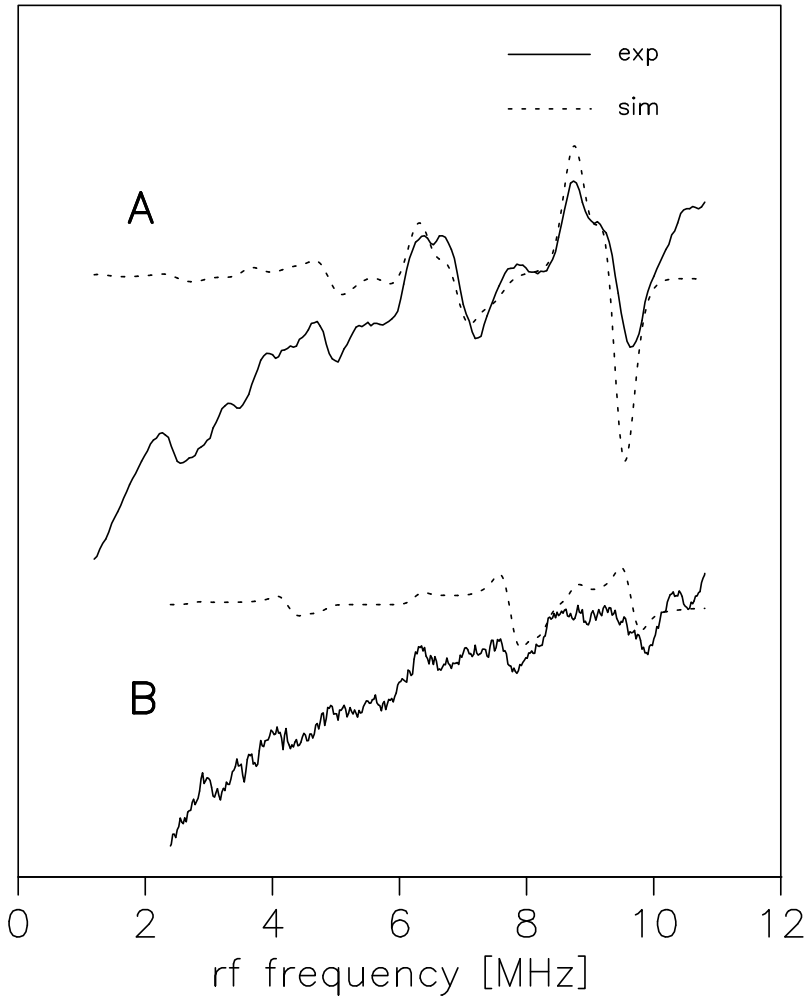

Figure 3.21: *The dashed line displays a simulation of the nitrogen ENDOR resonances in the CW spectrum of center H.*
A: ^{14}N
B: ^{15}N
These resonances are assigned to two coordinating nitrogen atoms from histidine ligands 3.32. For the simulation the program MAGRES was applied. The parameter are listed in the Table 3.8.

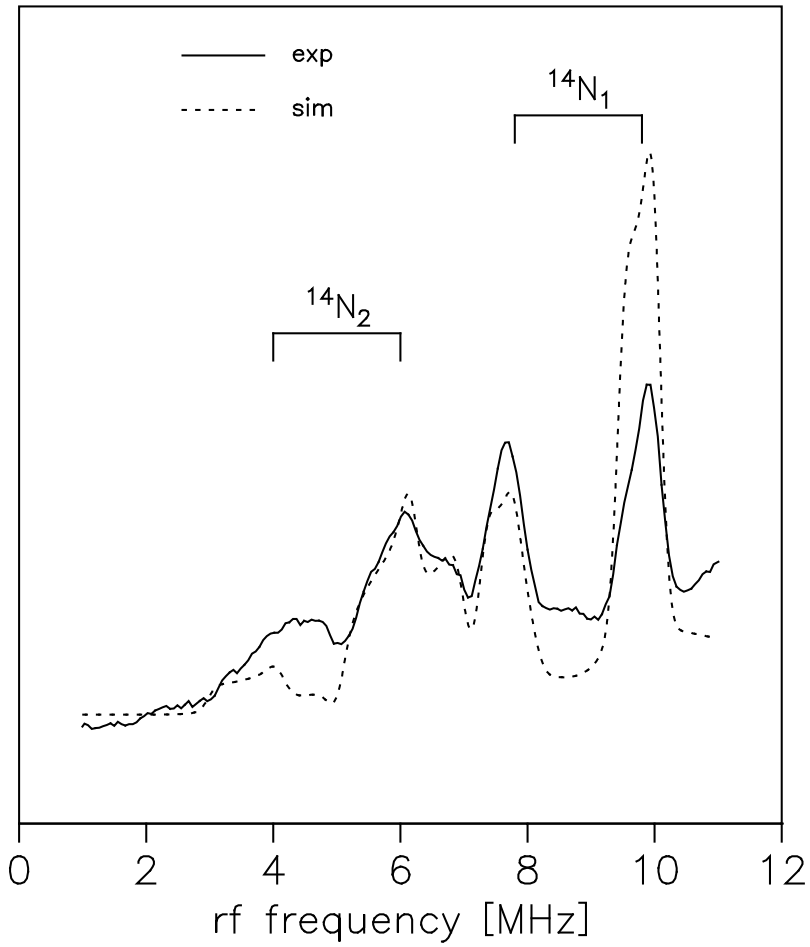

Figure 3.22: *The dashed line displays a simulation of the nitrogen ENDOR resonances in the pulsed ENDOR spectrum of center H. These resonances are assigned to two coordinating nitrogen atoms. For the simulation the program MAGRES was applied. The parameter are listed in the Table 3.8. The ENDOR line width used is 0.25 MHz and the line shape used is Gaussian*

Simulation parameter for the ^{14}N resonances measured for center H in Y122H by ENDOR techniques		
Quadrupole Parameters (MHz)		
	N_1	N_2
Q	1.6 ± 0.1	1.3 ± 0.1
η	0.9 ± 0.1	0.9 ± 0.1
Hyperfine Tensor (MHz)		
A_{xx}	15.4 ± 0.5	9.2 ± 0.4
A_{yy}	16.5 ± 0.5	10.0 ± 0.4
A_{zz}	18.7 ± 0.6	10.6 ± 0.5

Table 3.8: *Simulation parameters for the ^{14}N transitions in R2-Y122H protein. The ENDOR linewith for the simulations is 0.25 MHz and the shape is Gaussian.*

the hyperfine coupling lies around 1 MHz [157], thus far below the isotropic values of the hyperfine tensor observed in our case. They are 16.9 MHz and 9.9 MHz, respectively.
Therefore we assign both couplings to ligating histidine N_δ. This supports a model, where the di-iron center H is coordinated similarely as the diamagnetic Fe(III)Fe(III) center seen in the crystal structure of Y122H (see Figure 3.32).

Further Discussion

An interesting point is the calculation of the intrinsic couplings for each nitrogen atom.

As discussed in chapter 2 for mixed valence di-iron centers of type Fe(II)Fe(III) as well as Fe(III)Fe(IV) the couplings of hyperfine sensitive nuclei can be related to the expected couplings of equivalent mononuclear species via their spin projection coefficients. Brian Hoffman's group applied this technique in order to get information about the intrinsic couplings for two ligating nitrogens of the Fe(II)Fe(III) cluster in methane monooxygenases [83]. In the case of a nitrogen coordinated to the ferric iron of a Fe(II)Fe(III) or Fe(III)Fe(IV) center the formula:

$A_{N_1,measured} = \frac{7}{3}A_{N_1,intrinsic}$ and for the ferrous or ferryl iron $A_{N_2,measured} = -\frac{4}{3}A_{N_2,intrinsic}$ is employed [83].

In case of center H a three spin coupling model was introduced in the preceding section on ^{57}Fe ENDOR. The intrinsic nitrogen couplings are determined using the spin projection coefficients from this section. The procedure, however, is analogous to the case of Fe(III)Fe(IV) or Fe(II)Fe(III).

For center H, we get
$A_{N_1,measured} = \frac{7}{3}A_{N_1,intrinsic}$ and $A_{N_2,measured} = -\frac{14}{9}A_{N_2,intrinsic}$ in the case of antiferromagnetic coupling between the Fe(III)Fe(III) di-iron center and the ligand radical. For the case of ferromagnetic coupling the factors are 20/9 and -5/3, respectively.

The intrinsic couplings are calculated to 7.2 MHz for N_1 and 6.4 MHz for N_2 in the first case and 7.6 MHz for N_1 and 5.9 MHz for N_2 in the second case, respectively. The approximate unpaired spin density in a nitrogen 2s orbital is now estimated via the equation [158]:

$$a_{iso,intrinsic} = \frac{f_{2s}a^0_{2s}}{2S}$$

where f_{2s} denotes the unpaired spin density in the nuclear s-orbital, a^0_{2s} the isotropic coupling constant for a spin population of unity at the ^{14}N 1s-orbital, for which a value of 1163 MHz is reported [158], and S the spin quantum number of the electron spin. For the intrinsic nitrogen couplings to center H this yields a unpaired spin density for N_2 of approximately 2.8% and for N_1 of 3.1% (antiferromagnetic case) or of 2.5% (N_2) and 3.3% (N_1) (ferromagnetic case). In Table 3.9 these values are compared with the values received for other iron centers ligated by histidine. They all are found to be of the same magnitude within a factor of 2. The factors for center H are also a further evidence for the proposed structure Fe(III)Fe(III) plus ligand radical, since they are systematically larger than the factors determined for a ligation to the Fe(II)/Fe(IV) site and much more resemble the factors determined for a ligation to the Fe(III) site.

center	f_{2s} **Fe(II)/Fe(IV) site**	f_{2s} **Fe(III) site**	**reference**
Rieske 2Fe-2S	1.5% 2%		[143]
Fe(II)Fe(III) in MMO	1.4%	3%	[83]
metmyoglobin		3%	[159]
center H in Y122H	$2.8\%^{af}$ $2.5\%^{f}$	$3.1\%^{af}$ $3.3\%^{f}$	this work

Table 3.9: Spin densities on s-orbitals of coordinating nitrogen atoms calculated from the intrinsic isotropic hyperfine coupling component (see text) for different iron centers in proteins as reported in the literature and this work. For center H: ^{f} denotes ferromagnetic coupling between iron and ligand radical, ^{af} are the spin densities for the case of antiferromagnetic coupling.

3.3.4 Determination of Proton Hyperfine Couplings in the EPR and ENDOR Spectra of Center H

In biological samples protons can be regarded as one of the most prominent nuclei detected in EPR or ENDOR investigations, since numerous of them are expected in the environment of each metal center of a protein. Proton ENDOR and the investigation of the contribution of proton hyperfine couplings to the EPR line width of center H is expected to reveal interesting information on the electronic environment of the di-iron center H.

In metal centers, protons which are not directly coordinated to the metal often exhibit hyperfine interactions with a small isotropic part. Their hyperfine tensors are dominated by a dipolar interaction with the electron spin. Therefore, a model is applied, which describes dipolar interactions to a dimetal center. This will be used in the next sections for calculating dipolar proton couplings for center H in R2-Y122H.

First of all, dipolar hyperfine tensors are purely anisotropic and therefore exhibit zero trace. In a very simple point dipole model, which is applicable if the distance r between electron and nuclear spin is large enough, so that it is a good approximation to regard the spin distribution as point-like, the tensor can be considered as axial with tensor components (for a spin density of 1) [57]:

$$A_{\perp} = -79\, MHz/r^3 \tag{3.14}$$

$$A_{\parallel} = -2A_{\perp}, \tag{3.15}$$

where $A_{\parallel}$ points into the direction of the axis connecting both spins. An extended point dipole model, especially suitable for dinuclear metal centers of total electron spin 1/2, is described in reference [162]. It accounts for two centers of the electron spin distribution in a distance d from each other. It furtheron takes the spin projection coefficients s_1 and s_2 into consideration. The diagonal elements of the proton hyperfine coupling tensor are then given by [162]:

$$diag(\mathbf{A}) = g_e\beta_e g_n\beta_n \left\{ \begin{array}{c} -\delta \\ -\Gamma + \delta/2 \\ \Gamma + \delta/2 \end{array} \right\} \text{ MHz Å}^3 \tag{3.16}$$

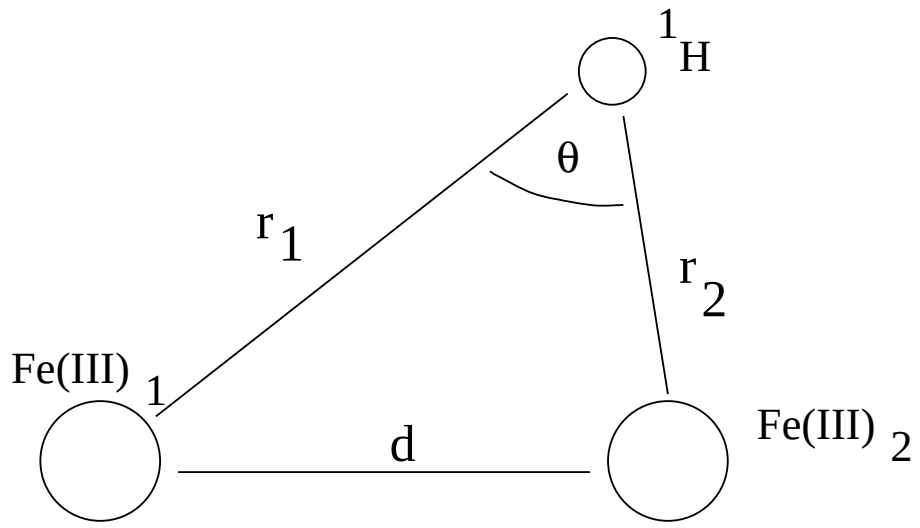

Figure 3.23: *Schematic representation of the geometric parameters for the extended dipole model [162].*

with

$$\delta = s_1 r_1^{-3} + s_2 r_2^{-3},$$

$$\Gamma = \frac{3}{2}\sqrt{s_1^2 r_1^{-6} + 2 s_1 s_2 r_1^{-3} r_2^{-3} cos(2\theta) + s_2^2 r_2^{-6}}$$

where r_1 and r_2 are the distances between each of the two centers and the nuclear spin, respectively, and θ denotes the angle enclosed by $\vec{r}_1$ and $\vec{r}_2$ (see Figure 3.23).

Information necessary for the assignment of proton ENDOR resonances can often be achieved from a H_2O/D_2O exchange: The protein is kept in D_2O buffer for a prolonged time. During this time exchangable protons will be substituted by deuterium. Deuterium nuclei exhibit different magnetic properties compared with protons: Their larmor frequency occurs at 2.2 MHz compared with 14 MHz for protons at X-band. Therefore, in D_2O exchanged samples new lines around 2 MHz are expected and the disappearance of lines in the proton region.

Thus ENDOR lines due to proton and deuterium nuclei are easy to discriminate, if the protein concentration and the yield of the paramagnetic center is high enough. Due to the large anisotropy of such protons, ENDOR lines are considerably broadened.

Using this technique, ENDOR lines in di-iron centers have been previously assigned to protons in ligating water [83, 85], in hydroxide bridges [83] or in hydrogen bridges [50, 53], which all are exchangeable in an H_2O/D_2O experiment: Evidence

for a hydroxide bridge could be gained in the case of the Fe(II)Fe(III) cluster in methane monooxygenase [83], while the absence of a hydroxide bridge was established for intermediate X [85].

CH-protons of tyrosine, histidine, tryptophan or CH_2 protons are not substituted by this technique and therefore their resonance position will not change. The assignment of couplings deriving from non-exchangeable protons can be done by substituting the amino acids in question by their deuterated analogues. The couplings are then expected to vanish from their symmetric pair positions around the proton matrix and reemerge with a factor of 6.5 decreased hyperfine coupling strength (due to the lower nuclear γ of deuterium: 2.2 MHz is the Zeeman frequency of deuterium at X-band).

ENDOR Analysis of the Small Proton Couplings of Center H

In the CW-ENDOR spectrum of center H in R2-Y122H several small ($A < 7$ MHz), overlapping proton couplings are resolved around the matrix peak at 14 MHz. The resolved hyperfine coupling components of these protons can be roughly estimated to 6.0, 5.3, 4.3, 2.5, 2.0 and 1.0 MHz. They presumably derive from protons of the ligating amino acids.

For an analysis of these proton couplings around the matrix line in the CW-ENDOR spectrum of center H, the extended dipole model was applied. The following assumptions were made:

- The structure of the center can be considered as identical or at least very similar to the Fe(III)Fe(III) cluster seen in the X-ray structure of mutant Y122H crystals.
- The extended point dipole model, as it was introduced above, is regarded as good approximation.

The protons of the ligating histidine His118, His241, glutamates, and aspartate were added to the X-ray crystal structure employing the program INSIGHT. For each hydrogen in the coordination sphere of the di-iron center as seen in the crystal structure the distance to the iron next to His122 and the H-Fe-Fe angle were determined. These parameters could now be used in order to determine the components of the hyperfine coupling tensor according to equations 3.16 of the extended point dipole model. The spin projection coefficients for the two iron atoms have been calculated before in this work for a model consisting of three spins coupled to each other. There are two cases, which have to be taken into account (see section 3.3.2): In the first case, the coupling between the third spin, the ligand radical, and the adjacent iron is ferromagnetic, in the second case antiferromagnetic.

Therefore, four simulations were made, two for the antiferromagnetic ($c_1 = -5/3$, $c_2 = 20/9$) and two for the ferromagnetic case ($c_1 = 7/3$, $c_2 = -14/9$). For each case the two spin projection coefficients were exchanged between the two Fe(III) in a second simulation. The simulation, which fits the spectrum best, was the one for the spin projection coefficients $c_1 = 7/3$, $c_2 = -14/9$ and is shown in Figure 3.24. Only the seven largest proton couplings have been used for the simulation. Table 3.10 lists the proton couplings used and what protons they belong to.

Hyperfine coupling tensor components (in MHz) used for the simulation of the proton matrix region in the CW ENDOR spectrum of H in Y122H.

proton	A_1^a	A_2^a	A_3^a
H_α at C_1 His118^b	-3.4	-7.4	10.8
H_α at C_1 His241^b	-0.4	-6.8	7.2
$H_{\beta,1}$ of His118^b	-3.6	-4.2	7.8
$H_{\beta,2}$ of His118^b	-2.5	-2.9	5.3
$H_{\beta,1}$ of His241^b	1.4	-4.0	3.6
$H_{\beta,2}$ of His241^b	1.2	-3.3	2.1
OH-proton Asp84^b	-5.0	-5.9	10.9

Table 3.10: *Hyperfine proton tensor components for a simulation of the proton matrix region of center H in R2-Y122H. Only the seven largest couplings (with components larger than 3 MHz) are used in the simulation. Below 3 MHz too many couplings are contributing which makes assignments impossible.*

[a] *The orientation of the tensor is chosen collinear with the g-tensor.*
The dependence on the position of the protons has been neglected.

[b] *For the His 118 ligating iron the spin projection coefficient 7/3 is chosen.*

Two possible assignments can be made from the simulation: The line pair labelled o in Figure 3.24 fits the calculated coupling constants for a OH-proton of aspargate 84 ligating the Fe(III) with spin projection coefficient 7/3. The resolved line pair around the matrix separated by approximately 4 MHz (label x) can be simulated by the perpendicular part of a β proton tensor belonging to the histidine ligating Fe(III) with spin projection coefficient 20/9 (His241 in Table 3.10). These are the most prominent features which can be assigned. The lines in the simulation belonging to larger hyperfine components like the two histidine α-protons and the perpendicular component of the Asp84 OH-proton are not resolved in the spectrum. To the lines belonging to smaller couplings (2-3 MHz, see Table 3.10) several protons are contributing (see tensors in Table 3.10), making an assignment impossible. Several other protons, as the two remaining α-protons of the two histidines and the protons belonging to the Asp and Glu ligands, lie in the same region. They are not included in the simulation. The protons with couplings in this region are presumably contributing to the overlapping lines around the matrix for $A < 3$ MHz.

Unfortunately, the agreement between experimental and simulated spectrum is not very good. This means that the environment of center H in R2-Y122H has slightly changed compared with the environment of the EPR silent Fe(III)-O-Fe(III) detected in the crystal structure. A possible explanation of this lies in the proposed structure for center H: Fe(III) - Fe(III) - R• (see section 3.2.2), and therefore the still unknown ^1H couplings of the ligand radical R•. Identification of the ligand radical and its hyperfine couplings in the future will presumably yield a more accurate structure of the environment of center H and a more accurate simulation of the proton ENDOR resonances.

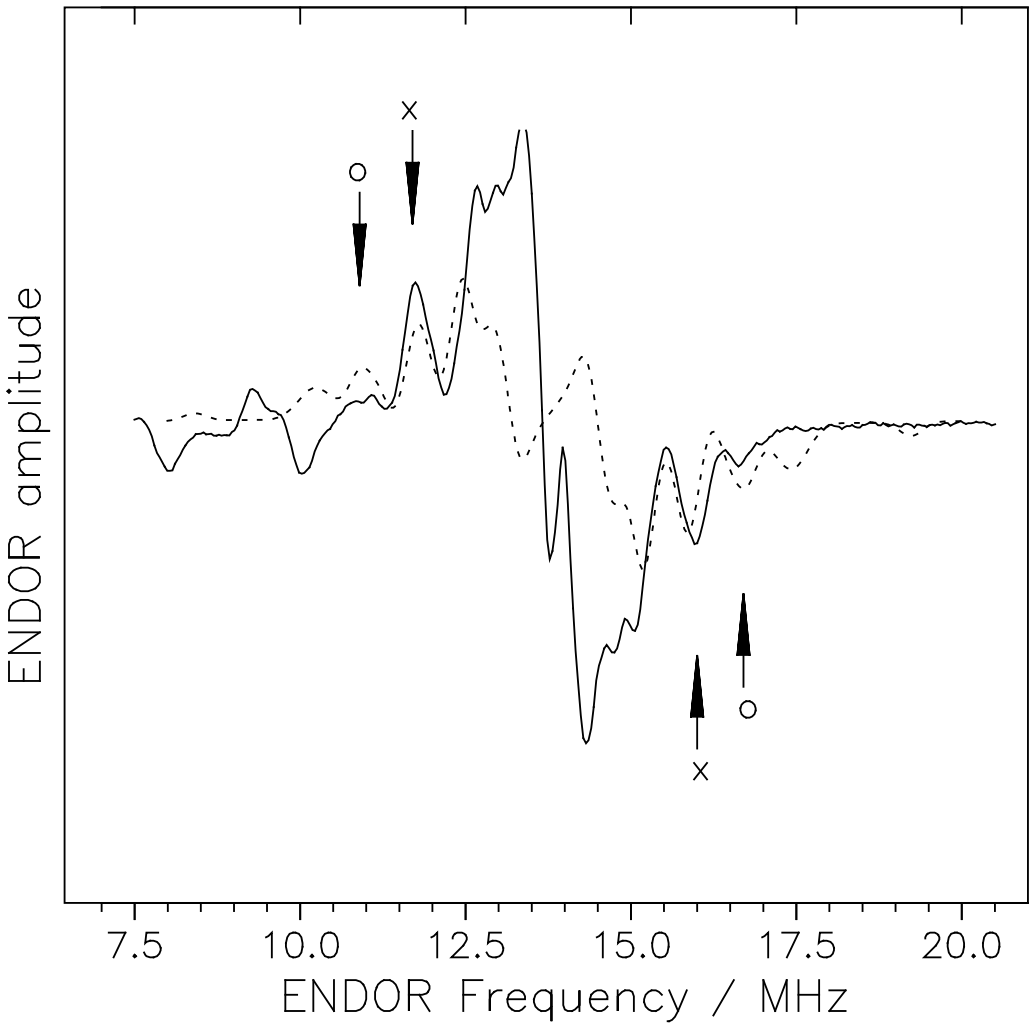

Figure 3.24: *Simulation of the proton ENDOR resonances (dashed line) for center H in R2-Y122H on the basis of the X-ray crystal structure of center H and a calculation according to the extended point dipole model (see text) in comparison with the X-band CW ENDOR spectrum of center H. The couplings employed are listed in the Table 3.10. Assignable proton couplings have been marked (couplings see Table 3.10):*
x*: H_β of His118 and/or H_β of His241*
o*: proton from the OH group of Asp84*
Experimental conditions of the CW-ENDOR spectrum: temperature 9 K, microwave power: 8 mW, radiofrequency power: 100-150 W, modulation frequency: 12.5 kHz, modulation amplitude: ±140 kHz

Analysis of the X-band EPR Lineshape of Center H with an Emphasis on Contributions from Proton Hyperfine Couplings

The X-band spectrum of center H (see Figure 3.9) exhibits a rather large inhomogeneous Gaussian line shape of 2.2 mT. This large line width is attributed to unresolved hyperfine tensors and/or the unresolved g-anisotropy. The spectrum of intermediate X, in comparison, has a line width of only 1.8 mT. Therefore, the contribution of the hf couplings and the g-tensor anisotropy to the X-band line width of center H is investigated: First, the spectrum is simulated with a much smaller basic line width and the g-values. The nitrogen hyperfine coupling tensor derived in the last section and several proton tensors are then added. The purpose of this simulation is to achieve information on the strength of one or more proton hyperfine couplings needed to account for the X-band line width of center H. An assignment of these hyperfine coupling tensors will be tried. In Figure 3.25 A the X-band signal for center H has been simulated with a Gaussian line width of 0.7 mT, g-tensor principal values 2.0088, 2.0040 and 1.9960 and two nitrogen tensors (hyperfine coupling components from Table 3.8). The nitrogen tensors alone evidently cannot account for the line width of 2.2 mT. The proton resonances observed in the CW-ENDOR spectrum of center H are too small to have a considerable effect on the line width (simulation not shown).

In the crystal structure of mutant Y122H, however, each iron atom of the di-iron center is ligated by one water molecule. The distances of the water oxygen from the iron atoms they are coordinated to are determined from the X-ray data. They are 2.07 and 2.11 Å, respectively. For center H, a rough estimate of the expected order of magnitude of the hyperfine coupling due to a proton of a water ligand was made by using the extended dipole model and the spin projection coefficients determined in section 3.3.2. The distance was calculated by assuming an O-H bonding length of 1 Å and a Fe-O-H angle of 120^o. For the water bound to the Fe(III) next to the residue H122 the spin projection coefficient 7/3 was used in the calculation and the following tensor components are calculated:

$$A_1^{H_1} = -6.5\ MHz,\ A_2^{H_1} = -11.1\ MHz\ A_3^{H_1} = 17.6\ MHz$$

$$A_1^{H_2} = -7.1\ MHz,\ A_2^{H_2} = -9.1\ MHz\ A_3^{H_2} = 16.2\ MHz$$

and for the water molecule ligating the other iron atom (spin projection coefficient

-14/9):

$$A_1^{H_1} = 1.4\ MHz,\ A_2^{H_1} = -11.5\ MHz\ A_3^{H_1} = 10.1\ MHz$$

$$A_1^{H_2} = 2.7\ MHz,\ A_2^{H_2} = -9.3\ MHz\ A_3^{H_2} = 6.5\ MHz$$

These couplings are larger than the small proton couplings around the proton matrix in the CW-ENDOR spectrum of center H. Therefore, in Figure 3.25 B these four proton couplings originating from the four protons of two water ligands are added: As can be seen in the spectrum of Figure 3.25 these couplings still cannot explain the Gaussian line width of 2.2 mT. Exchanging the spin projection coefficients between the iron atoms or using the spin projection coefficients -5/3 and 20/9 (for the antiferromagnetic case, see section 3.3.2) gives similar results.

In order to acquire more information about the proton couplings contributing to the line width of center H a buffered solution (pH=6.0) of mutant Y122H protein from cells grown in LB medium was treated with D_2O buffer for 96 h by M. Kolberg in order to exchange possible ligating water molecules or hydroxide bridges. The exact procedure is described in reference [107]. At the same time a control sample was treated in an equivalent procedure, but this time in H_2O buffer. Two X-band samples were prepared, one with 1 mM Y122H protein content in 80 μl D_2O buffer, the other 80 μl 0.8 mM in H_2O buffer as control sample. X-band CW EPR spectra were taken under non-saturating conditions (5 μW) and with a modulation amplitude (0.2 mT) well below the line width of center H. The spectra for both samples are shown in Figure 3.25 C. Indeed, in the sample treated with D_2O, the line width is decreased by approximately 1.5 G, while the shape has become assymmetric: The low field edge has grown steeper compared with the signal taken for the H_2O sample, which on the other hand exhibits a pure Gaussian shape. These differences, however, could not be explained by the couplings of the water protons calculated above. In order to simulate the spectra successfully (see Figure 3.25 D and E) another two large proton couplings have to be postulated. One of them exchanges in D_2O, the other one does not: A fit procedure applying the simulation program written by Kai Schäfer suggests an anisotropic coupling with a maximum parallel component of around 33 MHz and a perpendicular component of -16.8 MHz (along g_z). The proton responsible for this coupling exchanges. The other, non-exchangable proton is supposed to have a maximum hyperfine coupling component of 22.4 MHz

and a negligible component along g_z ($A_{zz} \approx 0$).

This is a clear evidence for a large coupling of an exchangeable proton in center H.

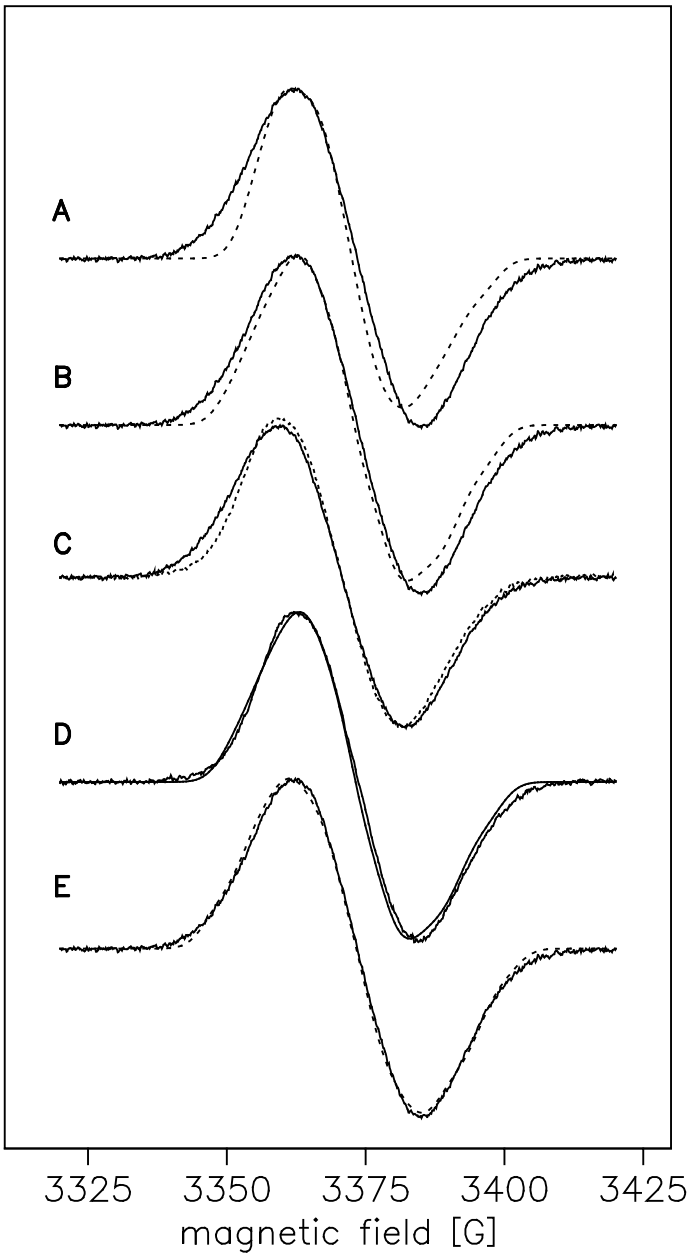

Figure 3.25: *Spectra and simulations (dashed lines) for the D_2O and H_2O buffered samples of mutant Y122H protein (see text).* **A***: Simulation (dashed line) for center H employing the g-tensor as measured from W-band spectra, a inhomogeneous line width of 0.7 G and the two ^{14}N nitrogen tensors from Table 3.8.*
B*: Four hyperfine tensors from protons from ligating waters are added to the simulation (dashed line). The parameters are reported in the text.*
C*: The X-band EPR spectra for D_2O treated Y122H (dashed lines) and the H_2O treated control sample are compared.*
D*: Simulation of the X-band EPR spectrum of the 1 mM D_2O Y122H sample (dashed line). The parameters for the proton couplings are listed in the text.*
E*: The deuterium coupling in D is exchanged for the corresponding proton coupling and the resulting simulation is compared with the X-band EPR spectrum of the 1 mM D_2O Y122H sample.*
Experimental conditions for the X-band spectra: temperature: 30 K, microwave power: 5 μW, modulation frequency: 12.5 kHz, modulation amplitude: 0.2 mT

^1H ENDOR Experiments of Center H and Intermediate X

In order to find out more about the couplings of the protons of the water ligands and the proton couplings needed to simulate the H_2O/D_2O spectra for the H_2O/D_2O exchanged samples, ENDOR studies are necessary. Therefore, ENDOR spectra of samples containing center H, and, for comparison, intermediate X were recorded. Q-band ENDOR measurements of D_2O exchanged samples proved successful in giving evidence for a water ligand in case of intermediate X [85] and for a hydroxide bridging the Fe(II)Fe(III) center in methane monooxygenase (MMO) [83, 160, 161]. In reference [85] the extended point dipole model was employed in order to estimate the tensors theoretically and to discriminate between a proton deriving from a hydroxide bridge and a water ligand. In Figure 3.26 the X-band CW ENDOR spectrum of intermediate X is shown and compared with the spectrum of center H. The region, where the tensor components of the H_2O protons were identified, is marked. Indeed, the resonances deriving from the axial components of both water protons are clearly visible. Unfortunately, no large proton couplings in this region are observed for center H.

Davies Pulsed ENDOR spectra were also recorded for both H_2O/D_2O samples of center H. Since anisotropic broad resonances are expected for both protons, pulsed ENDOR is more promising compared with CW ENDOR due to its advantages for detecting broad lines. Unfortunately, no large couplings could be detected. Beside the height of the matrix peak there is no significant difference observed between the sample in H_2O and D_2O buffer and no proton couplings in the expected order of magnitude are seen at all (spectra not shown).

The reason, that the expected large proton couplings are not detected, is most probably the large anisotropy of these couplings, which causes a large spectral broadening of the ^1H-ENDOR signal, and the low yield of center H (only 3%). As a consequence of the low yield, the concentration of center H is still very low even in very concentrated R2-Y122H protein solutions (2 mM). A successful increase of the yield of center H may eventually help to identify the missing large proton couplings and the type of protons they belong to and therefore will be a major aim for the future.

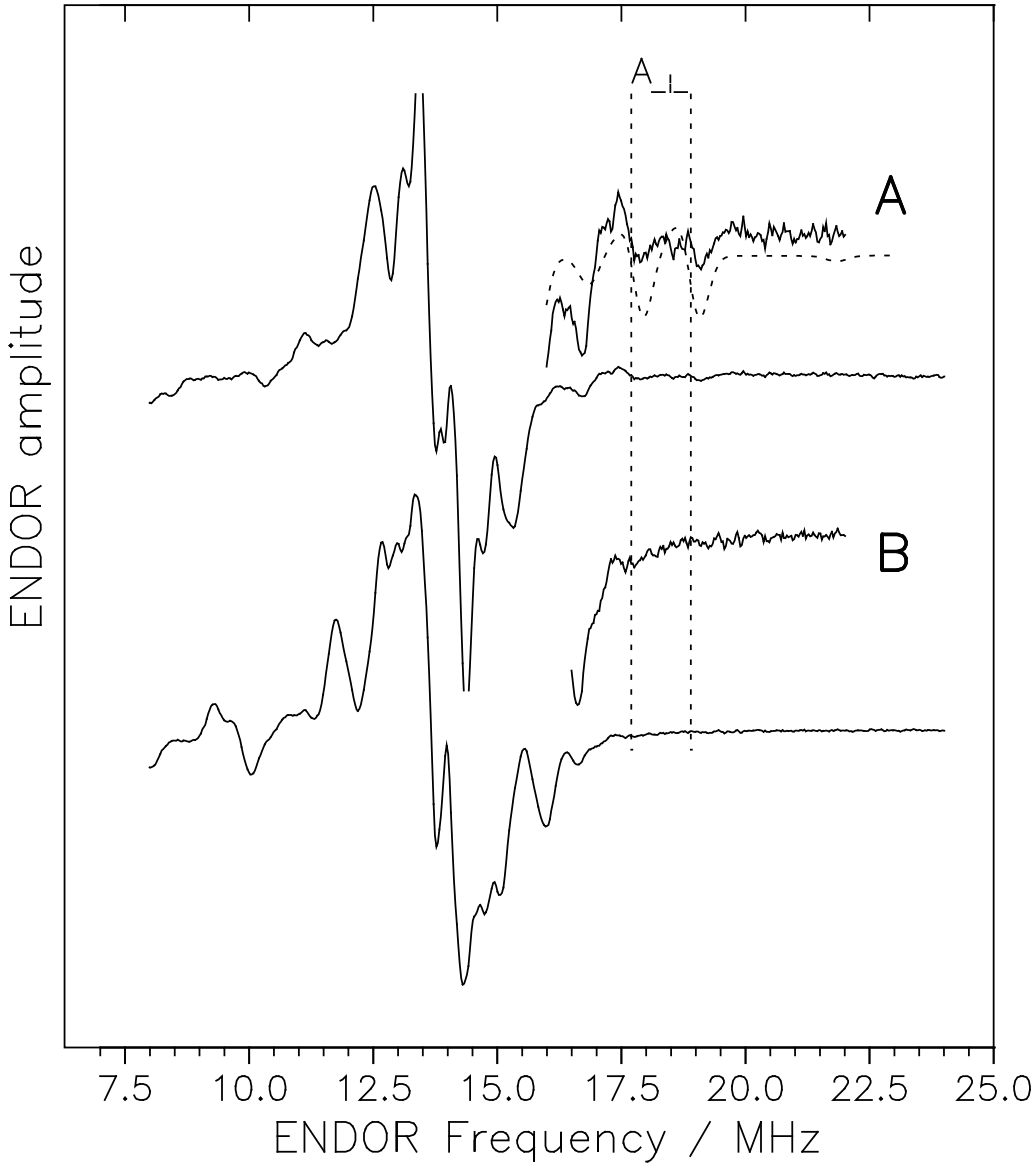

Figure 3.26: *Proton ENDOR of intermediate X in R2-Y122F freeze quenched at 300 ms (A) and center H in mutant R2-Y122H (B).*
A*: The region of the spectra, where the couplings from the water protons are expected is enlarged. For the simulation (program: SPLEEN) the following couplings were used:*
H_1: $A_\perp$: -10 MHz, $A_\parallel$: 20 MHz,
H_1: $A_\perp$: -8 MHz, $A_\parallel$: 16 MHz,
B*: For comparison the same region of the CW ENDOR spectrum for H in Y122H is displayed.*
Experimental conditions: temperature 9 K, microwave power: 8 mW, radiofrequency power: 100-150 W, modulation frequency: 12.5 kHz, modulation amplitude: ±140 kHz

3.4 High-Field EPR on Crystals of Mutant Y122H Protein

3.4.1 Introduction

EPR investigations on paramagnetic centers in crystals make it possible to reveal not only the principal values of the g-tensor, but also the orientation of the g-tensor principal axes with respect to the crystal axes and therefore the position of the g-tensor within the molecule. This can give valuable information on the electronic structure of the paramagnetic species since the g-axes are often oriented prefereably along certain symmetry axes of the molecule.

There exist many examples on paramagnetic centers in protein crystals, which have been characterized by EPR techniques [119, 120, 128, 129]. In a crystal rotation pattern, EPR spectra of the crystal are detected for different orientations whereby the crystal is turned around an axis perpendicular to the static magnetic field. In order to extract the orientation of the g-tensor from an EPR crystal rotation pattern an X-ray structure of the corresponding crystal has to be set into relation with the angular parameters gained from the analysis of the EPR spectra.

In order to resolve the angular dependence of the g-values, the EPR spectra of the paramagnetic signal have to be recorded at a frequency band, where the g-anisotropy is fully resolved. The 94 GHz EPR spectrum of center H in frozen solution R2-Y122H (see Figure 3.10 C) shows, that this is the case for center H.

Another reason, why W-band EPR at 94 GHz is a method well suited for crystal rotation pattern, is due to its ability to give sufficiently intense EPR spectra from small single crystals in the submillimeter range.

Center H forms spontaneously with about 3% yield and is found to be extremely stable: It survives in the crystal for at least two weeks at room temperature. The g-tensor principal values have been determined in EPR powder spectra at 94 GHz (see preceding sections).

3.4.2 Crystallisation and X-ray Diffraction Measurements

Y122H protein was prepared from cells possessing the R2-Y122H overexpressing *E. coli* strain and grown in LB medium by Dr. S. Pötsch in the laboratory of Prof. B.-M. Sjöberg at the University of Stockholm [27]. The purification of the pro-

tein was done as described previously [122]. After ultrafiltration a concentration of 30 $OD_{280-310}$/ml was achieved as checked by UV-Vis spectroscopy. A protein concentration of 30 $OD_{280-310}$/ml-40 $OD_{280-310}$/ml was necessary for the subsequent crystallisation procedure. The purity of the protein solution was checked by applying SDS PAGE with Coomassie Brilliant Blue Staining [121]. The crystallisation procedure is equivalent to the one applied for crystallisation of wild type R2 as described in references [10, 122]. The crystals were grown in the laboratory of Prof. Dr. D. Logan, Institute of Molecular Biology at the University of Stockholm, using the hanging drop method [122] from 18%-22% PEG, 0.4 M NaCl, 0.1 M MES at pH 6.0 as buffer and 10 mM thimerosal [10]. The solutions were placed in plastic dishes air-tight for two weeks in a dark place at a temperature of 23 ^{o}C. The size of the crystals studied by W-band EPR was about 1 mm $\times$ 0.4 mm $\times$ 0.4 mm.

The structure of the Y122H protein crystals was determined by X-ray diffraction at the Swiss-Norwegian beamline of the ESRF synchroton in Grenoble, France by Prof. Dr. D. Logan to a resolution of 1.95 Å.
The crystals belong to the rhombic space group $P2_12_12_1$ with four magnetically inequivalent protein R2-Y122H homodimers in a unit cell. These sites are related to each other by crystallographic symmetry operations: Starting with one site, the three other sites are obtained by a 180^o rotation around each of the three crystal axes. The unit cell dimensions are a = 73.77 Å, b = 84.69 Å, c = 114.31 Å with angles $\alpha = \beta = \gamma = 90^o$.
For the low temperature EPR measurements, the crystals were transferred together with a drop of mother liquor to quartz W-band EPR tubes (0.87 mm o.d., 0.7 mm i.d.) and rapidly frozen in liquid nitrogen.

3.4.3 EPR Experiments at 94 GHz

The EPR experiments on single protein R2 Y122H crystals were performed on a W-band EPR spectrometer BRUKER ESP680. The magnetic field was calibrated by employing a sample of Li:LiF as g standard ($g_{Li:LiF}$=2.002293 [124]). The spectra of the single crystals were recorded at 20 K. The cylindrical sample tube with the sample carrier rod was mounted on a goniometer for turning the crystal around the vertical axis, as drawn in Figure 3.27.

A rotation pattern was taken for a R2-Y122H crystal by rotating the sample

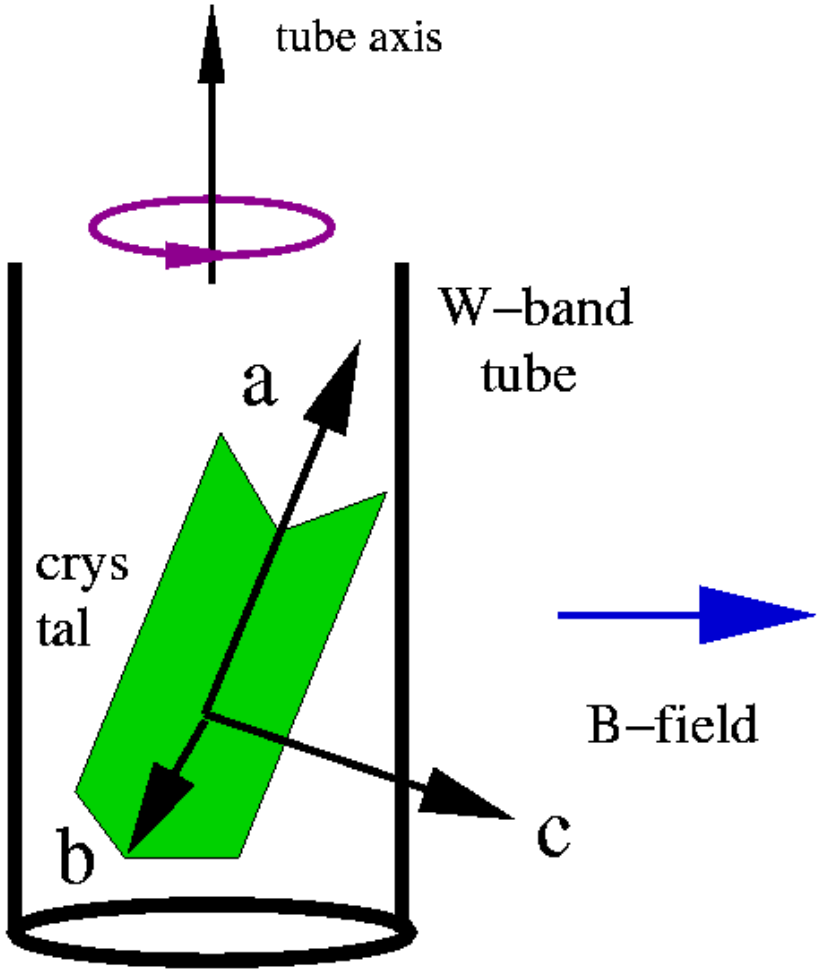

Figure 3.27: *The picture shows the position of the Y122H crystal in a quarz tube used for W-band EPR. The crystal axes are labelled a, b and c. The initial direction of the static magnetic field is indicated.*

in steps of 7.5^o after each EPR sweep, while the static magnetic field was fixed perpendicular to the rotation axis (see Figure 3.27). The orientation of the crystal in the W-band tube was observed through a microscope, while the identification of the position of the crystal axes a, b, and c was achieved by X-ray diffraction of crystal I in the frozen state in the EPR tube right after the EPR measurement. The spectra of center H in crystal I of R2-Y122H is displayed in Figure 3.28. The best resolved EPR spectra were obtained at 20 K and a microwave power of 0.05 mW where the signal is not saturated yet as has been checked by recording a saturation curve for a powder sample. Due to the space group of the crystal at least 4 single EPR lines are expected for each orientation, which move on the field scale upon crystal rotation. The four resonance lines partly overlap and require an accurate simulation in order to retrieve the orientation of the g-tensor.

The spectra shown in figure 3.28 were scaled linearly to 94 GHz [101]. This correction is important, since the W-band resonator is very sensitive to small variations regarding the position of the sample tube. Therefore the resonance frequency changes slightly while the crystal is rotated. The linear scaling of the spectra to 94 GHz, however, causes an error, since the g-anisotropy is frequency dependent while the splittings and line broadening effects caused by hyperfine couplings are not. This leads to an incorrect transformation of spectral patterns caused by hyperfine interactions. The error was estimated for a maximal frequency shift of 0.2 GHz, an isotropic g-value of 2.0029, and a maximal hyperfine coupling of 2.2 mT (line width of center H at X-band frequency) and lies below 0.01 mT. Therefore the error is very small compared with the line width and can be neglected.
A remark should be made on the four small lines appearing in the spectral background and at the low and high field sides of the rotation pattern. They obviously do not derive from the paramagnetic center in the crystal, since their saturation behaviour is totally different and their position independent of the rotation angle. They can be attributed to manganese(II) impurities in the sample or the resonator. These give rise to altogether six lines separated by about 90 G (four of them are visible) and are caused by a single hyperfine splitted EPR transition (manganese exhibits a nuclear spin of 5/2). They may be used as internal g-markers in addition to the method with Li:LiF.

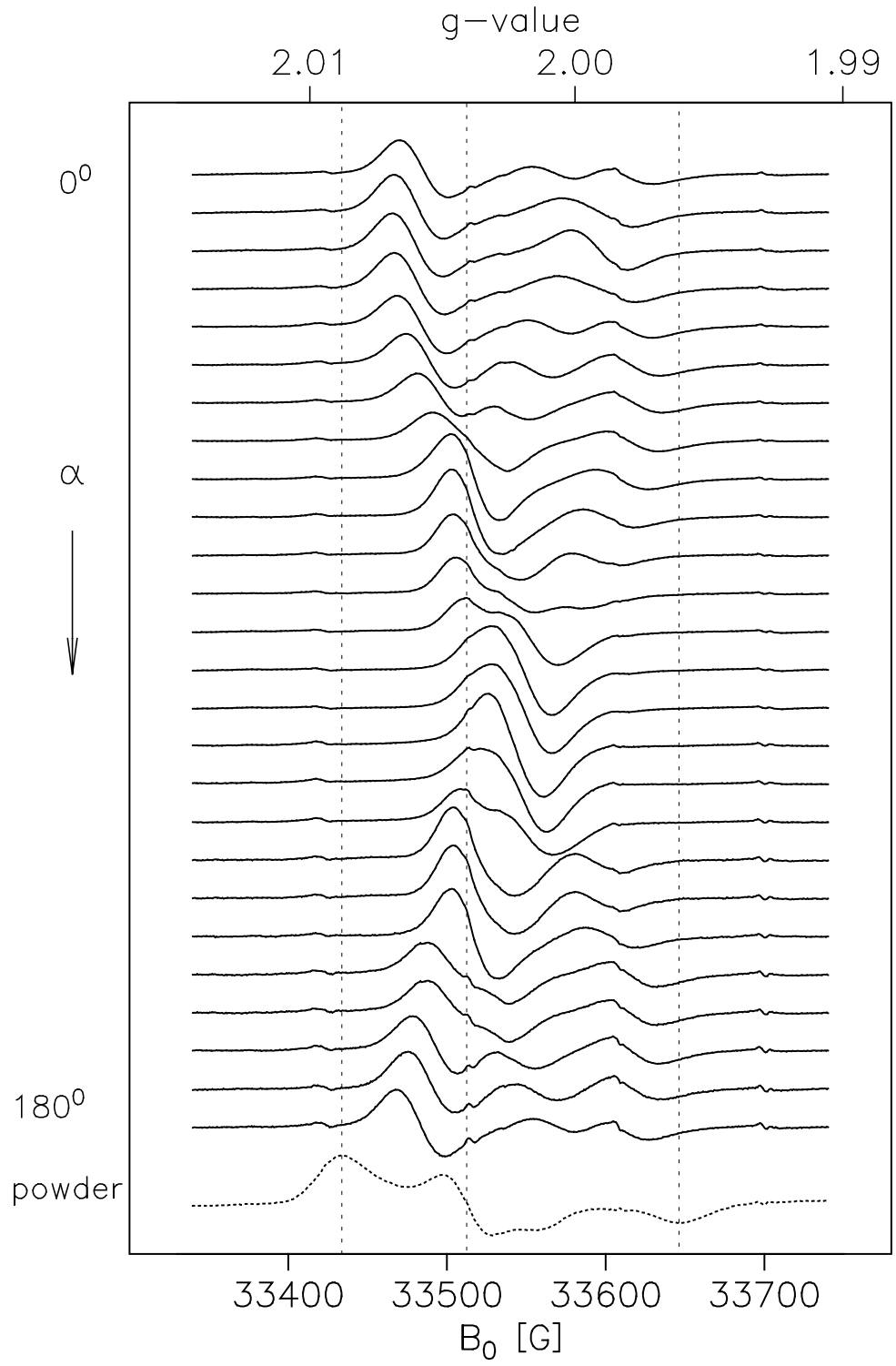

Figure 3.28: *Rotation pattern of a crystal (labelled I in this work) of mutant Y122H with center H taken at 94 GHz W-band frequency. The parameters for the measurements were: temperature: 20 K, microwave power: 0.05 mW, modulation amplitude: 5 G, modulation frequency: 100 kHz, time constant: 20.48 ms, sweep time 42 s; For comparison the powder spectrum of the center in mutant Y122H is displayed below the rotation pattern and the position of the g-tensor principal values is indicated by the dashed vertical lines.*

3.4.4 G-Tensor of Center H: Analysis and Spectral Simulation

The resonance condition in an EPR experiment with single crystals becomes

$$h\nu = g_{eff}(\theta, \phi)\beta B_0, \tag{3.17}$$

where B_0 is the static magnetic field, β the Bohr magneton, θ and ϕ horizontal and azimuthal angles describing a specific orientation on a sphere and g_{eff} is the effective g-value which depends upon the orientation of the anisotropic g-tensor with respect to the magnetic field [126]:

$$g_{eff} = \sqrt{\mathbf{l} \cdot \mathbf{g} \cdot \mathbf{g}^{\dagger} \cdot \mathbf{l}^{\dagger}}. \tag{3.18}$$

Here, $\mathbf{g}$ describes the g-tensor in its principal axis system, where it is diagonal and its diagonal elements are simply the g-tensor principal values:

$$\mathbf{g} = \begin{pmatrix} g_x & 0 & 0 \\ 0 & g_y & 0 \\ 0 & 0 & g_z \end{pmatrix} \tag{3.19}$$

The vector $\vec{l} = (l_x, l_y, l_z)$ gives the orientation of the static magnetic field within the frame of the g-tensor axes system via the corresponding direction cosines. $\mathbf{g}^{\dagger}$ and $\vec{l}^{\dagger}$ denote the transposed matrix and vector, respectively. The number of angular dependent resonance transitions seen in a single crystal EPR experiment depends upon the number of magnetically inequivalent paramagnetic species in a unit cell. Each site generates one single Gaussian EPR line, so that in case of the R2-Y122H crystals up to four lines are expected due to the four sites of space group $P2_12_12_1$ crystals. The number of lines increases to eight lines in case the species occurs in each of the two protein chains of the homodimer. Both chains are connected via a 180^o symmetry around the dimer axis. For an orientation of the magnetic field parallel to one of the crystal symmetry axes, the resonance lines due to the four sites will coincide and a single EPR resonance is observed.

The algorithm applied for the simulation of the EPR rotation pattern is based on the one described in in [101, 128]: Three right-handed, orthogonal coordinate systems are defined, the laboratory system (x,y,z), the crystal axes system (a,b,c) and the g-system (g_x, g_y, g_z), along whose axes the g-tensor is diagonal. The three coordinate systems are shown in Figure 3.29.

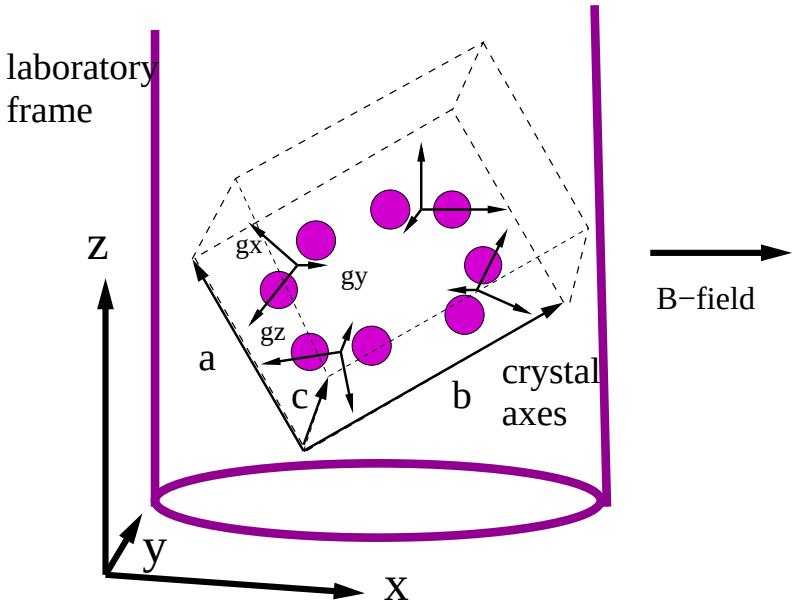

Figure 3.29: *This figure sketches the three coordinate systems necessary to describe a EPR crystal rotation pattern: The g-tensor axes system , which is drawn for all four sites, the crystal axes system defined by the three axes of the crystal unit cell a,b and c and the laboratory system.*

The following parameters are needed in order to describe a crystal rotation pattern by defining the rotations between these coordinate systems and the principal values of the g-tensor [125]:

- The three Euler angles ϕ_c, θ_c and ψ_c describing the rotation $\mathbf{R_{crys \rightarrow lab}}$ from the crystal axes system into the laboratory sytem
- The three Euler angles ϕ_g, θ_g and ψ_g for the rotation $\mathbf{R_{g \rightarrow crys}}$ from the g-tensor system into the crystal axes system
- The g-tensor principal values $g_x = 2.0088$, $g_y = 2.0040$, and $g_z = 1.9960$ determined from EPR powder spectra recorded at 94 GHz.

The rotations between the coordinate systems are performed by employing rotation matrices, which are defined as:

$$\mathbf{R} = \mathbf{R}_\psi \cdot \mathbf{R}_\theta \cdot \mathbf{R}_\phi, \tag{3.20}$$

where $\mathbf{R}_\phi$ rotates each vector around the z-axis:

$$\mathbf{R}_\phi = \begin{pmatrix} cos\phi & sin\phi & 0 \\ -sin\phi & cos\phi & 0 \\ 0 & 0 & 1 \end{pmatrix}$$

$\mathbf{R}_\theta$ around the new x-axis:

$$\mathbf{R}_\theta = \begin{pmatrix} 1 & 0 & 0 \\ 0 & cos\theta & sin\theta \\ 0 & -sin\theta & cos\theta \end{pmatrix}$$

and $\mathbf{R}_\psi$ executes once again a rotation around the new z-axis:

$$\mathbf{R}_\psi = \begin{pmatrix} cos\psi & sin\psi & 0 \\ -sin\psi & cos\psi & 0 \\ 0 & 0 & 1 \end{pmatrix}$$

with ψ, θ, and ϕ being the corresponding Euler angles. The whole simulation algorithm then is expressed as [128]:

$$g_{eff} = \sqrt{\vec{n} \cdot \mathbf{R_{crys \rightarrow lab}} \cdot \mathbf{S_i} \cdot \mathbf{D} \cdot \mathbf{R_{g \rightarrow crys}} \cdot \mathbf{g} \cdot \mathbf{g}^\dagger \cdot \mathbf{R}^\dagger_{\mathbf{g \rightarrow crys}} \cdot \mathbf{D}^\dagger \cdot \mathbf{S}^\dagger_\mathbf{i} \cdot \mathbf{R}^\dagger_{\mathbf{crys \rightarrow lab}} \cdot \vec{n}^\dagger} \tag{3.21}$$

Here, $\mathbf{g}$ describes the g-tensor in its own axes system, where it is diagonal, the symmetry operations $\mathbf{S_i}$ relate the four sites and yield four line positions for the four different matrices $\mathbf{S_i}$ $(i = 1, 2, 3, 4)$ [125]:

$$S_1 = \begin{pmatrix} 1 & 0 & 0 \\ 0 & 1 & 0 \\ 0 & 0 & 1 \end{pmatrix}, \; S_2 = \begin{pmatrix} -1 & 0 & 0 \\ 0 & -1 & 0 \\ 0 & 0 & 1 \end{pmatrix},$$

$$S_3 = \begin{pmatrix} -1 & 0 & 0 \\ 0 & 1 & 0 \\ 0 & 0 & -1 \end{pmatrix}, \; S_4 = \begin{pmatrix} 1 & 0 & 0 \\ 0 & -1 & 0 \\ 0 & 0 & -1 \end{pmatrix}$$

The R2 protein is a homodimer with two iron centers, which are related by C_2 symmetry. A matrix $\mathbf{D}$ describes this symmetry by a rotation of 180^o around the twofold dimer axis. This leads to eight lines for each spectrum at the end. $\mathbf{D}$ is a symmetrical matrix. It has been determined from the X-ray structure of the crystals:

$$D = \begin{pmatrix} -0.82277 & 0.54862 & 0.14855 \\ 0.54862 & 0.69825 & 0.45985 \\ 0.14855 & 0.45985 & -0.87548 \end{pmatrix}$$

In order to simulate the EPR rotation pattern a program was written in *C++* which calculates the resonance positions g_{eff} for each orientation for a given set of parameters and subsequently convolutes Gaussian envelopes at the different resonance positions.

3.4.5 Results

A rotation pattern was recorded and simulated for two different R2-Y122H crystals labelled I and II. The spectra and simulations are shown in Figure 3.30 and 3.31. Each paramagnetic center in one crystal site yields a single EPR line whose position on the magnetic field axis changes with the angle between the crystal axes and the magnetic field. The rotation pattern shows a 180^o periodicity as expected.

At around 105^o for crystal I and 165^o for crystal II the four resonances collapse into a single line indicating that at this point the B_0 field is approximately aligned with one of the crystal axis and all four sites become magnetically equivalent. For comparison the corresponding powder spectrum of center H in Y122H is drawn at the bottom of Figure 3.30 and 3.31. In case of the powder sample each possible orientation is contributing and the spectral line shape is obtained by integrating over all orientations on a sphere. Thus, the powder spectrum covers the whole range of possible single crystal resonance positions on the g-axis and marks the principal g-values. It therefore limits the line positions in the crystal. By comparing the ranges on the field axis covered by the pattern and the powder spectrum, it becomes clear that the g_x axis and also the g_z axis form a rather large angle with the rotation plane for all sites in the crystal.

Each of the four sites in a unit cell contains a homodimer of protein R2-Y122H suggesting two paramagnetic centers per site or, equivalently, eight centers per unit cell. This means that up to eight lines are expected in an EPR rotation pattern in the case that each monomer carries the paramagnetic center and the symmetry axis connecting both halves of the dimer does not coincide with one of the crystal axis. If it coincides with one of them, two lines are magnetically equivalent and fall together resulting in a four line pattern. This is not the case for center H, as has

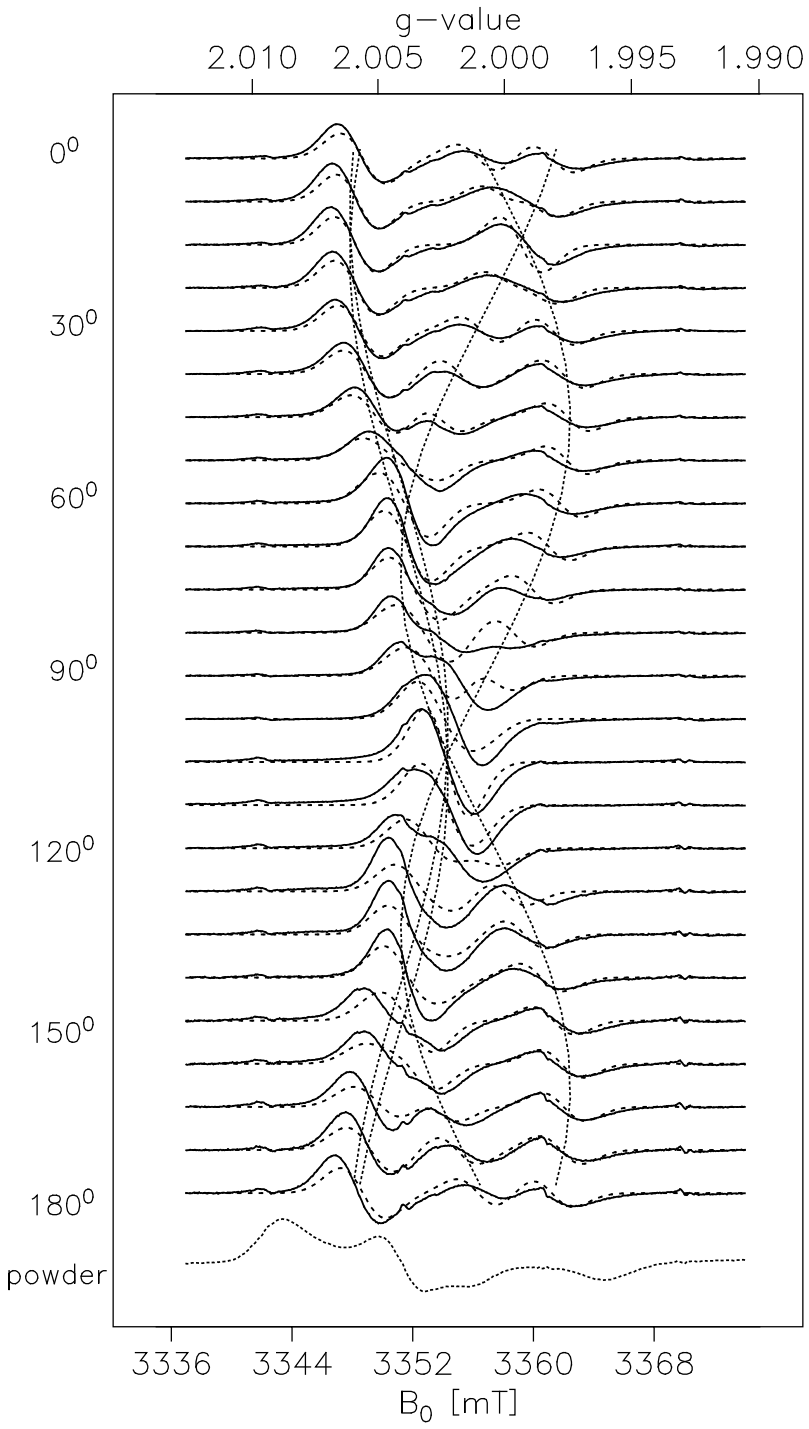

Figure 3.30: *EPR rotation pattern of center H in crystal I of mutant R2-Y122H taken each 7.5 degrees at 94 GHz W-band frequency. The parameters for the measurements were: temperature: 20 K, microwave power: 0.05 mW, modulation amplitude: 0.5 mT, modulation frequency: 100 kHz, time constant: 20.48 ms, sweep time 42 s; The parameters used for the simulation (dashed lines) are listed in the Table 3.11. The dotted lines show the position of g_{eff} for each line during a rotation.*

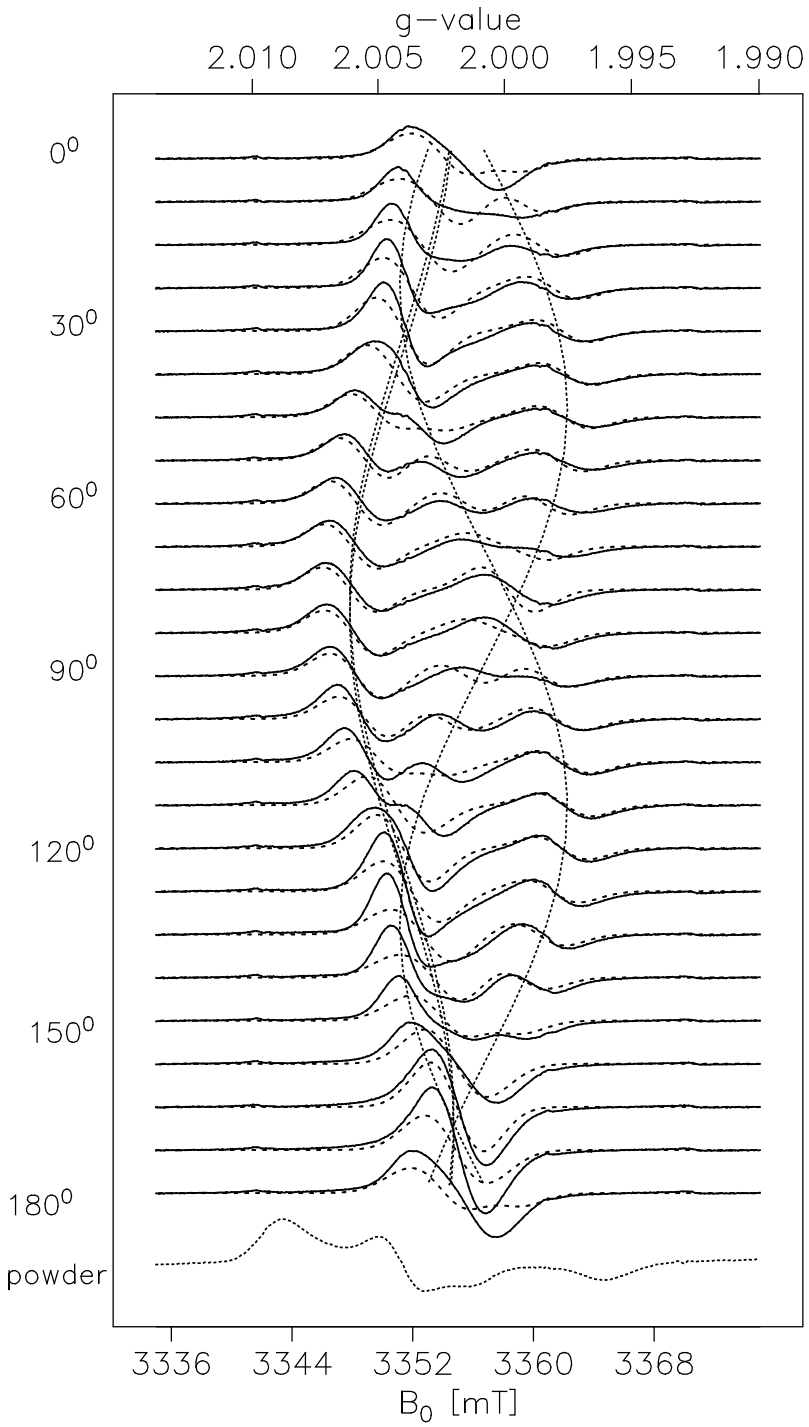

Figure 3.31: *EPR rotation pattern of center H in crystal II of mutant Y122H taken each 7.5 degrees at 94 GHz W-band frequency. The parameters for the measurements were: temperature: 20 K, microwave power: 0.63 mW, modulation amplitude: 0.2 mT, modulation frequency: 100 kHz, time constant: 20.48 ms, sweep time 42 s; The parameters used for the simulation (dashed lines) are listed in the Table 3.11. The dotted lines show the position of g_{eff} for each site during a rotation.*

Simulation parameter for center H in two different crystals of mutant Y122H		
	crystal II	**crystal I**
ϕ_c	15 ± 3	105 ± 2
θ_c	22 ± 3	22 ± 2
ψ_c	0 ± 3	0 ± 2
ϕ_g	45 ± 4	41 ± 3
θ_g	53 ± 2	53 ± 1
ψ_g	83 ± 2	83 ± 2
g_x	2.0088(1)	
g_y	2.0040(1)	
g_z	1.9960(2)	

Table 3.11: *Parameters for the simulation of the rotation patterns of center H in crystal I and II of mutant R2-Y122H. Numbers in parenthesis denote errors in the last digit.*

been verified by checking the position of the dimer axis within the crystal frame; the dimer axis encloses angles of 107.3^o, 157.1^o and 75.6^o with the crystal axis a, b and c, respectively, and therefore does not coincide with one of these axes.
In case the paramagnetic species occurs on only one of the two specific chains in each homodimer, only four lines are expected. To distinguish between these two possibilities an accurate simulation of the partly overlapping broad resonances is required.

Both sets of spectra were successfully simulated with four lines. The corresponding parameters are given in Table 3.11.

The best simulations for the crystal rotation pattern could be achieved with a Gaussian width of (3.3 ± 0.3) mT for crystal I and (3.5 ± 0.3 mT) for crystal II. G-strain has not been taken into account in the simulated pattern. The orientation of the g-tensor axes in the crystal frame gave consistent results for both crystals. The errors are estimated by varying the angular parameters and checking the coincidence of the resonance transitions between experimental rotation pattern and simulated spectra. An approach with eight lines, connecting both chains via the dimer rotation

matrix, did not yield satisfactory results; both crystals could not be simulated in a consistent way.

Both crystals investigated in this work, however, exhibit a similar orientation with respect to the rotation axis: The crystal axis a is nearly aligned with the tube axis and therefore the rotation axis. This leads to a similar rotation pattern for both crystals. In order to definitely exclude the possibility of 8 lines a Y122H crystal has to be analyzed in a different rotation plane. To achieve this, a different technique has to be used to mount the crystal in the W-band tube. The measurements for a different rotation plane are not reported in this work, but remain a task for the future. The results presented here are based on the measurements reported in this work and therefore have to be confirmed in the future.

For interpretation the data of the EPR simulation and thus the orientation of the g-tensor axes have to be compared with the known crystal structure. Here, it is important to remark that the anglular parameters for a simulation are not unambigous with regard to the simulated rotation pattern: One site in the crystal unit cell may well be represented by any of the four symmetry operations $\mathbf{S_i}$ for the sites. A second ambiguity arises due to the fact that 4 sites were simulated for one crystal from which is known that it contains four R2 homodimers and thus eight di-iron centers in its unit cell. The simulations show only four paramagnetic centers per unit cell. This means that species H occurs exclusively either in chain A or chain B of the homodimer, but not in both.
Since it does not come out of the simulations, what site it appears in, there are two further possibilities connected via the dimer rotation matrix $\mathbf{D}$. Summing up, 8 possible orientations of the g-tensor with respect of the geometry of the Fe-Fe center remain which are consistent with the simulations of the two rotation patterns. As a first result, however, the simulations imply that center H occurs in only one definite chain of the R2 homodimer.

In order to reduce this ambiguity the position of the g-tensor within a homodimer has to be discussed. It is known that only 3% of the homodimers in a R2-Y122H sample carry the paramagnetic center H. The crystal structure, however, reflects the remaining 97%, which carry the EPR silent μ-oxo bridged iron center Fe(III)Fe(III) as was confirmed by UV-Vis and Mössbauer spectroscopy [130]. Nev-

Y122H xtal: direction cosines between g-axis and Fe-Fe axis						
site	**CHAIN B**			**CHAIN A**		
symmetry	g_x	g_y	g_z	g_x	g_y	g_z
S_1	0.689	-0.676	-0.261	-0.547	0.276	0.790
S_2	-0.163	-0.119	-0.979	-0.092	0.691	0.717
S_3	-0.531	0.813	0.240	0.080	-0.679	-0.730
S_4	**0.005**	**-0.017**	**1.000**	0.559	-0.288	-0.777

Table 3.12: *Direction cosines between g-axes and the Fe-Fe connecting axis for the 8 orientations of the g-tensor allowed by the simulation of the EPR rotation pattern*

ertheless and under the assumption that center H most likely is structurally similar to the Fe(III)Fe(III) center, it is instructive to compare the directions imposed by the g-tensor system with the orientations of chemical bonds near the iron center. Since the signal indeed derives from a dinuclear iron center (see ^{57}Fe results presented in chapter 3.2.2) and its structure and orientations are supposed to be similar to those of the di-iron center of the 97 % in the crystal structure, one g-axis is expected to point along the Fe-Fe connecting vector [127]. Therefore the direction cosines between the Fe-Fe vector and the g-tensor principal axis were calculated for all remaining 8 possibilities. The numbers are shown in the Table 3.12.

For one assignment the direction cosine becomes 1.000. An exact calculation shows that the angle between the g_z axis and Fe-Fe connection axis becomes $\mathbf{1.6}^o \pm \mathbf{2.2}^o$. The error was estimated by comparing the simulations and the experimental spectra for various angular parameters.
So, as the first main result, the g-tensor orientation in the molecular frame has been determined.

In the subsequent section these results will be discussed and tested for consistency with literature reports from similar di-iron centers.

3.4.6 Discussion

EPR investigations on paramagnetic centers in crystals makes it possible to reveal not only the principal values of the g-tensor, but also the orientation of the g-tensor principal axes with respect to the crystal axes and therefore the orientation of the

g-tensor within the molecule. Here a g-tensor of a paramagnetic di-iron site in a protein single crystal has been determined and correlated to the molecular structure of the metal complex.
As was established by UV-Vis and Mössbauer measurements [130], 97% of the di-iron in mutant Y122H protein form an EPR silent antiferromagnetically coupled Fe(III)Fe(III) μ-oxo species found also in the active form of wild type R2 protein. Only 3% of R2-Y122H exhibit the paramagnetic center H. The reason for the low yield is hitherto unknown. A careful discussion of the suggested g-tensor orientation in the crystal frame is necessary, since it is based on the structure of the Fe(III)Fe(III) species which is seen in the X-ray structure of the R2-Y122H protein. We suppose that center H is a minority species within the R2-Y122H protein exhibiting a EPR active oxidation state with S=1/2 and having an almost similar geometry as 97% of the residual EPR silent di-iron site. The estimated smallest g-tensor component g_z lies parallel to the axis connecting the two iron atoms (see Figure 3.32).

For comparison with the found g-tensor orientation, it is necessary to discuss earlier measurements and calculations for mixed valence di-iron centers. In the case of Fe(II)Fe(III) centers in iron-sulfur clusters [127], theoretical calculations assign the axis of the largest g-value pointing in the Fe-Fe direction. This does not have to be a contradiction to the case reported here, since the g-tensor principal values for Fe(II)Fe(III) clusters differ rather strongly from the ones found for our center (Table 3.4). Theoretical calculations for Fe(III)Fe(IV) are not known so far, however orientation selective proton and deuterium ENDOR on terminal water ligating the Fe(III) site in the Fe(III)Fe(IV) center in intermediate X in *E. coli* ribonucleotide reductase was reported by Willems et al. [85] and may be of interest to be compared with our case. The g-tensor of intermediate X has been measured [84]: g_1=2.007, g_2=1.999, g_3=1.994. Intermediate X has not been studied in crystals yet, however, orientation selective ENDOR is a suitable technique to get information on the position of a g-tensor with respect to an anisotropic hyperfine tensor. By comparing experimental results with theoretical models, it was suggested by Willems et al. [85] that one of the axial proton hyperfine coupling components of the terminal water lies parallel to the corresponding Fe(III)-H connecting axis and nearly aligns with g_1 [85]. Inspection of the crystal structure of wild type R2 and mutant Y122H

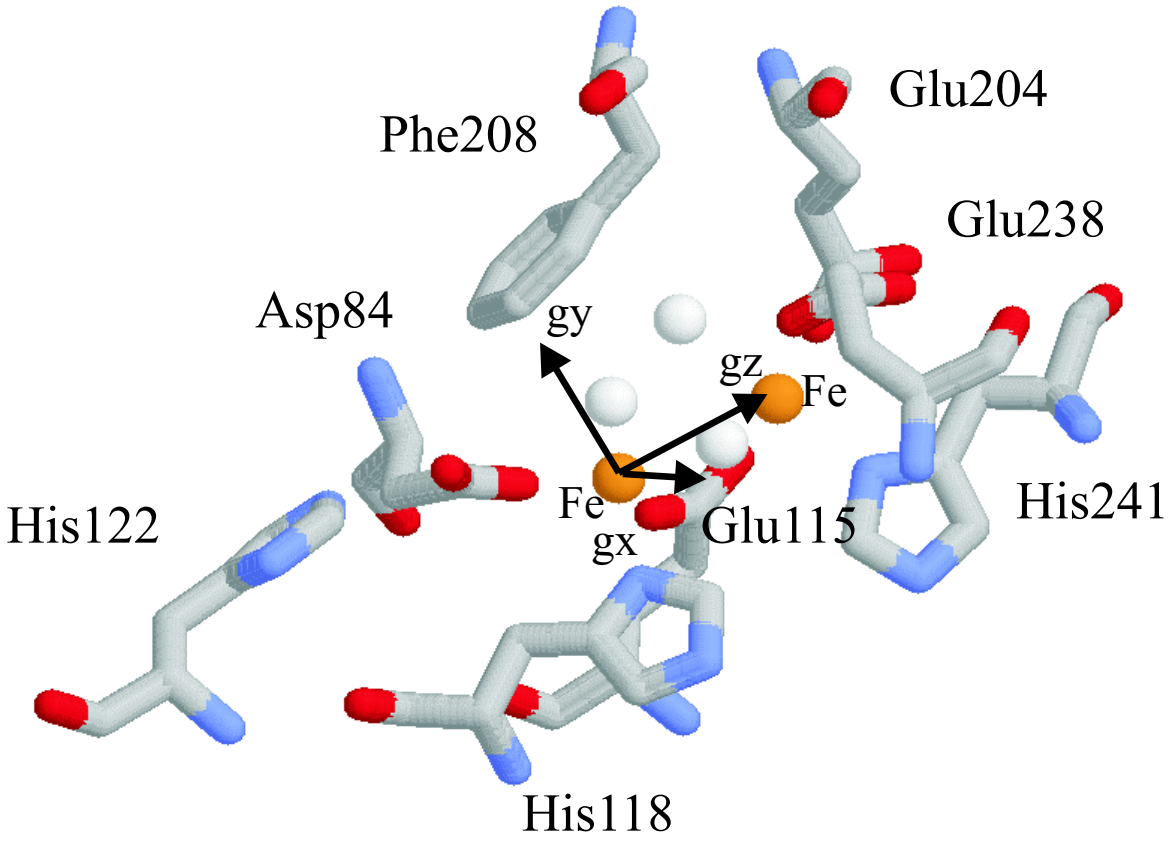

Figure 3.32: *Position of the g-tensor axes system of center H for the case of Fe-Fe connecting axis parallel to g_z in the structure of R2-Y122H as it was determined by X-ray.*

R2 suggests a mainly perpendicular orientation of the Fe-H axes for the ligating waters and the di-iron axis (angles between 45^o and 118^o are possible between H-Fe and Fe-Fe axes), which may apply to intermediate X as well. In this case the largest g-tensor component does not align with the di-iron axis, which is consistent with the interpretation of the simulations for center H reported in this work.

According to the single crystal EPR data in this work, center H occurs exclusively on chain B of the homodimer. The occurence of a species on only one definite chain of a protein homodimer is not unusal: There exist reports about other R2 mutants where e.g. the hydroxylation of residue Phe208 in mutant Y122F/E238A [131] occurs also exclusively in one protein chain of the homodimer.

On the basis of the ^{57}Fe ENDOR data and a theoretical three spin coupling model (see preceding chapter) an antiferromagnetical Fe(III)Fe(III) plus ligand radical with ground state S=1/2 is suggested for center H in R2-Y122H. There are important hints for the position of this ligand radical from this work and from other studies:

- First of all, the direction of the g_y axis as it was determined in this study points to the C-atom in the meta position of the Phe208 ring (see Figure 3.32).
- Furtheron, there are reports on quite stable phenoxyl radicals ligating mononuclear iron [132]. Center H is very stable as well compared with other mixed valence di-iron centers.
- The proposal, that F208 may be the site of the ligand radical, is also supported by a paramagnetic species found in mutant R2-F208Y, which exhibits a paramagnetic center named Z with EPR and ENDOR features nearly identical to center H [133]. Z has been shown to possess considerable spin density on the Y208 residue [133].

Therefore a hydroxylation and subsequent ligation of Phe208 to one iron is proposed. Especially the orientation of g_y of center H in the R2-Y122H crystals indicates the importance of residue Phe208 to the interpretation of center H. According to this hypothesis, Phe208 carries a spin 1/2, which couples to the two spins 5/2 of the di-iron to form a paramagnetic species of spin 1/2. For further evidence of this model new studies are necessary. Especially ENDOR on Y122H with deuterated Phe is expected to yield information on the spin density at the Phe208 residue.

Chapter 4

Summary and Outlook

In this work the electronic structure of protein-associated paramagnetic centers in Ribonucleotide Reductase has been investigated by advanced EPR techniques:

Transient tryptophan radicals, in particular W111• in mutant R2-Y122F (*E. coli*) and W177• in mutant R2-Y177W (mouse) have been characterized by high-field EPR at 94 GHz and compared with stable tyrosine radicals Y177• and Y122• in wild type R2 in mouse and *E. coli*, respectively. The g-tensor anisotropy exhibited by these radicals and the hyperfine couplings resolved in the spectra have been analyzed. Due to the different g-anisotropy of these two types of radical the g-tensor can serve as fingerprint for the identification of the type of radical. This is not possible at X-band frequency, since the g-tensor is not resolved at 9.7 GHz. Therefore, W-band EPR represents a novel method to distinguish between tyrosine and tryptophan radicals.

Furtheron a novel paramagnetic di-iron center (center H) which is observed in mutant R2-Y122H (*E. coli*) was identified and its electronic structure characterized: At 94 GHz the g-tensor principal values have been resolved in frozen solution.

CW- and pulsed ENDOR techniques resolved the hfs of two ^{57}Fe nuclei confirming that center H is a di-iron center. A three spin coupling model was introduced, which yielded ^{57}Fe hyperfine coupling components which are in agreement with the measurements on center H. On the base of the three spin coupling model center H was identified as Fe(III)Fe(III) center exchange coupled to a ligand radical.

The analysis and simulation of two hyperfine couplings deriving from nitrogen atoms in the CW- and pulsed ENDOR spectra of center H gave evidence for two coordinated N_δ histidine nitrogens thus elucidating the ligand structure of center H.

For the first time a paramagnetic di-iron center was characterized in a crystal

at W-band CW-EPR: The simulations of the rotation pattern for center H in a R2-Y122H crystal observed at 94 GHz yielded the orientation of the g-tensor in the molecular structure. As a preliminary result it was found that

- center H occurs in only one protein chain (chain B, respectively)
- the lowest g-tensor principal value points into the direction of the di-iron axis
- the medium g-tensor principal value points at the meta position in the Phe208 residue.

The results have to be confirmed by repeating the measurements with R2-Y122H crystals rotated in a different rotation plane in the future.
Residue Phe208 is postulated to be the position of the ligand radical coupled to the Fe(III)Fe(III) center.

Summarizing, the investigation presented in this thesis shows the electronic structure of center H as a di-iron center.

Future investigations have to complete our knowledge by

- confirming the g-tensor orientation in R2-Y122H crystals presented in this work
- identifying the nature of the ligand radical and give evidence for a ligand radical at a phenoxyl residue: Until now the assignment to position Phe208 is a postulation supported in particular by literature data. CW- and pulsed ENDOR investigations on deuterated Phe208 are expected to provide experimental evidence for this suggestion and complete the characterization of center H.

Additional future work will also be an increase of the yield of center H in R2-Y122H and a characterization of similar centers which have been found in other mutants of R2 (such as F208Y).

Generation of intermediate X in crystals R2-Y122F will be of major interest, because this makes it possible to determine the orientation of the g-tensor of a mixed valence di-iron center of type Fe(III)Fe(IV). Comparison with center H will be instructive and increase the knowledge about di-iron centers, which are known to play an important role for enzymatic oxygen activiation in many cases (as in RNR, methane monooxygenase and hemerythrine). The application of EPR at high fields will thereby be the method of choice, whenever the g-anisotropy or the sizes of the crystals lie in a similar order of magnitude as in the case of center H.

Q-band and W-band ENDOR will, in the future, allow a orientation selective investigation of the hyperfine tensors in center H. The orientation of the g-tensor is known by EPR investigation of center H in crystals. Q-band and W-band ENDOR investigations could yield the orientation of the hyperfine tensors in the molecular frame and therefore give additional structural information on the center and maybe general information on the electronic state of ligating nuclei in di-iron centers.

Chapter 5

Zusammenfassung

In dieser Arbeit wird die elektronische Struktur paramagnetischer Zentren in Klasse Ia Untereinheit R2 von Ribonukleotid Reduktase mittels EPR Techniken untersucht.
Wildtyp R2 besitzt im aktiven Zustand ein bereits gut charakterisiertes Tyrosylradikal an der Position Y122 und ein antiferromagnetisch gekoppeltes Fe(III)Fe(III) Zentrum etwa 5 Å davon entfernt. Im Laufe der sogenannten Rekonstitutionsreaktion wird Eisen im Oxidationszustand +II in eisenfreies apo-Protein R2 eingebaut, was wiederum durch O_2 aktiviert wird und nach Durchlauf eines intermediären Zustands Fe(III)Fe(IV) (Intermediate X) und Oxidation des Tyrosins Y122 in den Fe(III)Fe(III)-Zustand gelangt. Das Tyrosinradikal Y122•, das in eine Umgebung von hyrophoben Aminosäureresten eingebettet ist, weist eine erstaunliche Stabilität auf, wenn man seine Lebensdauer (im Bereich von Tagen) mit der von freien Tyrosinradikalen vergleicht. Durch Mutationen der Position Y122 wurde in einem Projekt, in dessen Rahmen auch diese Doktorarbeit fällt, untersucht, ob andere Aminosäureradikale an der gleichen Position erzeugt und stabilisiert werden können.

Vor diesem Hintergrund wird in dieser Doktorarbeit eine bisher unveröffentliche W-Band Studie an Tryptophanradikalen, wie sie als W111• in der Mutation R2-Y122F (*E. coli*) und W177• in der Mutation R2-Y177W (Maus) auftreten, präsentiert: Die g-Tensor Anisotropie wird für beide Radikale bestimmt sowie die in den Spektren aufgelösten Hyperfeinkopplungen werden analysiert. Die Spektren werden zudem mit denen der Tyrosinradikale in den jeweiligen Wildtypproteinen verglichen: Aufgrund der charakteristischen Anisotropie des g-Tensors für beide Radikaltypen lassen sich beide im W-Band ohne aufwendige Isopotenmarkierungen sehr einfach identifizieren und voneinander unterscheiden. Im X-Band ist das nicht möglich, da

hier die die g-Anisotropie nicht aufgelöst ist. Die unterschiedliche g-Anisotropie läßt sich mit Hilfe der unterschiedlich stark ausgeprägten Spinbahnkopplung von Sauerstoff (Tyrosin) im Vergleich zu Kohlenstoff- und Stickstoffatomen (Tryptophan) erklären.
Im zweiten Teil dieser Arbeit wird ein bisher unbekanntes paramagnetisches Zweieisenzentrum (Zentrum H), das in der R2-Mutanten Y122H beobachtet wird, identifiziert und charakterisiert: Im X-Band zeigt Zentrum H nur eine einzelne EPR Linie ohne aufgelöste Hyperfein- oder g-Tensoranisotropie. Das Sättigungsverhalten sowie die beträchtliche Verbreiterung für Zentrum H in ^{57}Fe markiertem Protein weisen auf eine eisenzentrierte Spezies hin. Im W-Band ist es möglich, die g-Tensorhauptwerte vollständig aufzulösen.

^{57}Fe substituiertes Protein zeigt eine Verbreiterung der Linie von 2.2 mT auf 4.3 mT im X-Band, was auf starke aber unaufgelöste Eisenkopplungen hinweist. Mittels Davies Puls-ENDOR als auch CW ENDOR konnten zwei ^{57}Fe Tensoren vollständig aufgelöst werden. Ein 3-Spin Kopplungsmodell wurde eingeführt, das ^{57}Fe Hyperfeintensoren liefert, die in sehr guter Übereinstimmung mit den gemessenen Werten für Zentrum H in R2-Y122H sind. Aufgrund dieses Modells wird Zentrum H als Fe(III)Fe(III) Eisenzentrum interpretiert, das mit einem S=1/2 Ligandenradikal austauschgekoppelt ist. Aufgrund früherer Arbeiten über relativ stabile Phenoxylligandradikale sowie einem Isotopeffekt, der für ein paramagnetisches Zentrum in der Mutante R2-F208Y, das ein fast identisches EPR Verhalten wie Zentrum H aufweist, gefunden wurde, wird in Y122H eine Hydroxilierung von Phe208 angenommen und zugleich Phe208 als Ort des Ligandenradikals vorgeschlagen.

Im weiteren wurden im Rahmen dieser Doktorarbeit die Hyperfeintensoren von Stickstoffatomen sowie die der Protonen in ENDOR Spektren an gefrorenen Lösungen von Zentrum H in R2-Y122H untersucht. Aufgrund der erfolgreichen Simulation der Stickstofflinien, wobei die Hyperfein- als auch die Quadrupolkopplungen berücksichtigt wurden, konnten beide Stickstoffatome durch Vergleich mit Literaturwerten als an die Eisen koordinierte N_δ Stickstoffe von Histidinliganden identifiziert werden.

Die erfolgreiche Kristallisation des Proteins R2-Y122H durch Dr. Stephan Pötsch und die Bestimmung der Proteinstruktur mittels Röntgenkristallographie durch Prof Dr. D. Logan ermöglichten eine W-Band Analyse des Zentrums H in R2-Y122H Kristallen. Durch eine Simulation der W-Band Rotationspattern von Zentrum H in

R2-Y122H Kristallen ist erstmals eine Zuordnung der g-Tensorhauptachsen in die Molekülstruktur in einem paramagnetischen Zweieisenzentrum möglich.

Als vorläufige Resultate aus der Analyse der Kristallspektren läßt sich folgendes zusammenfassen:

- Nach den ersten Mesungen und Auswertungen kommt Zentrum H nur auf einer Proteinkette des Y122H Homodimers vor (Kette B).
- Die kleinste g-Tensorkomponente verläuft in Richung der Eisen-Eisen Verbindungsachse.
- Die mittlere g-Tensorkomponente zeigt in Richtung der Aminosäure Phe208, die als Ort des Ligandenradikals angenommen wird.

Diese Resultate sollen in naher Zukunft durch eine Messung an einem Kristall Y122H, der so befestigt wird, dass seine Längsachse (Kristallachse a) eine unterschiedliche Orientierung zur Rotationsachse aufweist, überprüft werden. Die Ergebnisse waren bei Fertigstellung dieser Arbeit noch nicht bekannt.

Weitere Experimente in der Zukunft werden unser Wissen über Zentrum H vervollständigen. Geplant sind insbesondere die Identifizierung des Ligandenradikals durch ENDOR Messungen an Y122H Proteinlösungen, in denen Phe208 deuteriert vorliegt. Sowohl W-Band als auch Q-Band ENDOR wird orientierungsselektive Untersuchungen der Protonen und Stickstoffkopplungen in Zentrum H ermöglichen und damit die Aufklärung der elektronische Struktur des Zentrums vervollständigen.

Bibliography

[1] P. Reichard, *Science*, 260, 1773-1777, **1993**

[2] J. Stubbe and W. A. van der Donk, **Chem. Rev.**, 98, 705-762, **1998**

[3] P. Reichard and L. Ruthberg, *Biochim. Biophys. Acta*, 37, 554-555, **1960**

[4] L. Thelander, S. Eriksson, and L. Akerblom, *J. Biol. Chem.*, 255, 7426-7432, **1980**

[5] J. Harder and H. Follmann, *FEBS Lett.*, 222, 171-174, **1987**

[6] Y. Huque, F. Fieschi, E. Torrents, I. Gibert, R. Eliasson, P. Reichard, M. Sahlin, and B.-M. Sjöberg, *J. Biol. Chem.*, 275, 25365-25371, **2000**

[7] R. L. Blakley, H. A. Barker, *Biochem. Biophys. Res. Commun.*, 16, 391-397, **1964**

[8] M. Fontecave, R. Eliasson, and P. Reichard, *Proc. Nat. Acad. Sci.*, 86, 2147-2151, **1989**

[9] P. Young, M. Öhman, M. Q. Xu, D. A. Shub, and B. M. Sjöberg, *J. Biol. Chem.*, 269, 20229-20232, **1994**

[10] P. Nordlund, B. M. Sjöberg, and H. Eklund, *Nature*, 345, 593-598, **1990**

[11] B. Kauppi, B. B. Nielsen, S. Ramaswamy, I. K. Larsen, M. Thelander, L. Thelander, and H. Eklund, *J. Mol. Biol.*, 262, 706-720, **1996**

[12] U. Uhlin and H. Eklund, *Nature*, 370, 533-539, **1994**

[13] S. S. Mao, T. P. Holler, G. X. Yu, J. M. Bollinger, S. Booker, M. I. Johnston, and J. Stubbe, *Biochemistry*, 31, 9733-9743, **1992**

[14] A. Aberg, S. Hahne, M. Karlsson, A. Larsson, M. Ormö, A. Ahgren, and B. M. Sjöberg, *J. Biol. Chem.*, 264, 12249-12252, **1989**

[15] J. Stubbe, J. Ator, T. Krenitsky, *J. Biol. Chem.*, 258, 1625-1630, **1983**

[16] H. Zipse, *J. Am. Chem. Soc.*,117, 11798-11806, **1995**

[17] J. Stubbe, D. Ackles, *J. Biol. Chem.*, 255, 8027-8030, **1980**

[18] A. I. Lin, G. W. Ashley, J. Stubbe, *Biochemistry*, 26, 6905-6909, **1987**

[19] W. A. van der Donk, G. Yu, D. J. Silva, J. Stubbe, J. R. McCarthy, E. T. Jarvi, D. P. Matthews, R. J. Resvick, E. Wagner, *Biochemistry*, 35, 8381-8391, **1996**

[20] P. E. M. Siegbahn, *J. Am. Chem. Soc.*, 120, 8417-8429, **1998**

[21] R. Lenz and B. Giese, *J. Am. Chem. Soc.*, 119, 2784-2794, **1997**

[22] K. Regnström, A. Aberg, M. Ormö, M. Sahlin, B. M. Sjöberg, *J. Biol. Chem.*, 269, 6355-6361, **1994**

[23] B. B. Nielsen, Dissertation, Royal Danish School of Pharmacy Copenhagen, Copenhagen, **1994**

[24] B. J. Waller and J. D. Libscomb, *Chem. Rev.*, 96, 2625-2657, **1996**

[25] A. Åberg, M. Ormö, P. Nordlund, and B.-M. Sjöberg, *Biochemistry*, 32, 9845-9850, **1993**

[26] M. Sahlin, A. Gräslund, L. Petersson, A. Ehrenberg, and B.-M. Sjöberg, *Biochemistry*, 28, 2618-2625, **1989**

[27] A. Larsson, B. M. Sjöberg, *EMBO*, 5, 2037-2040, **1986**

[28] J. B. Lynch, C. Juarez-Garcia, E. Münck, and L. Que, *J. Biol. Chem.*, 264, 8091-8096, **1989**

[29] C. L. Atkin, L. Thelander, P. Reichard, G. Lang, *J. Biol. Chem.*, 248, 7464-7472, **1973**

[30] P. P. Schmidt, U. Rova, B. Katterle, L. Thelander, and A. Gräslund, *J. Biol. Chem.*, 273, 2163-2172, **1998**

[31] J. Y. Han, J. C. Swarts, A. G. Sykes, *Inorg. Chem.*, 35, 4629-4634, **1996**

[32] G. Lassmann, L. Thelander, A. Gräslund, *Biochem. Biophys. Res. Commun.*, 188, 879-887, **1992**

[33] M. Sahlin, B. M. Sjöberg, G. Backes, T. Loehr, and J. Sanders-Loehr, *Biochem. Biophys. Res. Commun.*, 167, 813-818, **1990**

[34] W. H. Tong, S. Chen, S. G. Lloyd, D. E. Edmondson, B. H. Huynh, J. Stubbe, *J. Am. Chem. Soc.*, 118, 2107-2108, **1996**

[35] K. Kim, S. J. Lippard, *J. Am. Chem. Soc.*, 118, 4914-4915, **1996**

[36] P. Moënne-Loccoz, J. Baldwin, B. A. Ley, T. M. Loehr, and J. M. Bollinger Jr., *Biochemistry*, 37, 1659-1663, **1998**

[37] T. Ookubo, H. Sugimoto, T. Nagayama, H. Masuda, T. sato, K. Tanaka, Y. Maeda, H. Okawa, Y. Hayashi, A. Uehara, M. Suzuki, *J. Am. Chem. Soc.*, 118, 701-702, **1996**

[38] B. M. Sjöberg, *Structure*, 2, 793-796, **1994**

[39] B. O. Persson, M. Karlsson, I. Climent, J. Ling, J. Sanders-Loehr, M. Sahlin, B. M. Sjöberg, *J. Biol. Inorg. Chem.*, 1, 247-256, **1996**

[40] M. Ekberg, M. Sahlin, M. Eriksson, B. M. Sjöberg, *J. Biol. Chem.*, 271, 20655-20659, **1996**

[41] P. E. M. Siegbahn, L. Eriksson, F. Himo, and M. Pavlov, *J. Phys. Chem. B*, 102, 10622-10629, **1998**

[42] P. E. M. Siegbahn, M. R. A. Blomberg, M. Pavlov, *Chem. Phys. Let.*, 292, 21-30, **1998**

[43] M. Sahlin, G. Lassmann, S. Pötsch, B. M. Sjöberg, and A. Gräslund, *J. Biol. Chem.*, 270, 12361-12372, **1995**

[44] F. Lendzian, M. Sahlin, F. McMillan, R. Bittl, R. Fiege, S. Pötsch, B. M. Sjöberg, A. Gräslund, W. Lubitz, and G. Lassmann, *J. Am. Chem. Soc.*, 118, 8111-8120, **1996**

[45] C. J. Bender, M. Sahlin, G. T. Babcock, B. A. Barry, T. K. Chandrashekar, S. P. Salowe, J. Stubbe, B. Lindström, A. Ehrenberg, B. M. Sjöberg, *J. Am. Chem. Soc.*, 111, 8076-8083, **1989**

[46] C. W. Hoganson, M. Sahlin, B. M. Sjöberg, and G. T. Babcock, *J. Am. Chem. Soc.*, 118, 4672-4679, **1996**

[47] G. J. Gerfen, B. F. Bellew, S. Un, J. M. B. Jr., J. Stubbe, R. G. Griffin, and D. J. Singel, *J. Am. Chem. Soc.*, 115, 6420, **1993**

[48] M. Bennati, C. T. Farrar, J. A. Bryant, S. J. Inati, V. Weis, G. J. Gerfen, P. Riggs-Gelasco, J. Stubbe, and R. G. Griffin, *J. Magn. Res.*, 138, 232-243, **1999**

[49] M. Sahlin, L. Petersson, A. Gräslund, A. Ehrenberg, B. M. Sjöberg, L. Thelander, *Biochemistry*, 26, 5541-5548, **1987**

[50] P. J. van Dam, J. P. Willems, P. P. Schmidt, S. Pötsch, A. L. Barra, W. R. Hagen, B. M. Hoffman, K. K. Andersson, and A. Gräslund, *J. Am. Chem. Soc.*, 120, 5080-5085, **1998**

[51] P. P. Schmidt, K. K. Andersson, A. L. Barra, L. Thelander, and A. Gräslund, *J. Biol. Chem.*, 271, 23615-23618, **1996**

[52] P. Allard, A. L. Barra, K. K. Andersson, P. P. Schmidt, M. Atta, and A. Gräslund, *J. Am. Chem. Soc.*, 118, 895-896, **1996**

[53] S. Pötsch, F. Lendzian, R. Ingemarson, A. Hörnberg, L. Thelander, W. Lubitz, G. Lassmann, and A. Gräslund, *J. Biol. Chem.*, 274, 17696-17704, **1999**

[54] M. Sahlin, G. Lassmann, S. Pötsch, A. Slaby, B. M. Sjöberg, and A. Gräslund, *J. Biol. Chem.*, 269, 11699-11702, **1994**

[55] J. J. Sakurai, *Modern Quantum Mechanics*, Addison-Wesley Publishing Company, **1994**

[56] P. W. Atkins, *Molecular Quantum Mechanics*, Oxford University Press, **1983**

[57] J. E. Wertz, J. R. Bolton, *Electron Spin Resonance*, Chapman and Hall N.Y. London, **1986**

[58] N. M. Atherton, *Principles of Electron Spin Resonance*, Ellis Horwood Limited, Chicester, England, **1993**

[59] J. R. Pilbrow, *Transition Ion Electron Paramagnetic Resonance*, Clarendo Press, Oxford, **1990**

[60] W. Lubitz and F. Lendzian, *Biophysical Techniques in Photosynthesis*, 255-275, **1996**

[61] M. Plato, W. Lubitz, and K. Möbius, *J. Phys. Chem.*, 85 1202-1219

[62] J. Rautter, Dissertation, Techn. Univ. Berlin, Berlin **1995**

[63] J. Hüttermann, *Biological Magnetic Resonance Vol. 13*, 219-251, **1993**

[64] S. A. Dikanov and Y. D. Tsvetkov, *Electron Spin Echo Envelope Modulation Spectroscopy*, CRC Press **1992**

[65] H. Käss, Dissertation, Technical University of Berlin, Berlin, **1994**

[66] C. C. Lawrence, M. Bennati, H. V. Obias, G. Bar, R. G. Griffin, and J. Stubbe, *Proc. Natl. Acad. Sci. USA*, 96, 8979-8984, **1999**

[67] R. D. Britt, *Advances in Photosynthesis Vol.3*, 235-253, **1996**

[68] D. Burdi, J. P. Willems, P. Riggs-Gelasco, W. E. Antholine, J. Stubbe, and B. M. Hoffman, *J. Am. Chem. Soc.*, 120, 12910-12919, **1998**

[69] A. Schweiger, *Angewandte Chemie*, 103, 223-250, **1991**

[70] H. Thomann and M. Bernardo, *Biological Magnetic Resonance* Vol. 13, 275-321, **1993**

[71] C. P. Poole Jr., *Electron Spin Resonance*, Wiley-Interscience, New York, **1983**[2]

[72] W. Zweygart, R. Thanner, W. Lubitz, *J. Magn. Res. A*, 109, 172-176, **1994**

[73] G. G. Maresch, *Bruker E600/680 User's Manual Version 1.13*, **1997**

[74] K. K. Andersson and A. Gräslund, *Adv. Inorg. Chem.*, 43, 359-07, **1995**

[75] L. Petersson, A. Gräslund, and A. Ehrenberg, B. -M. Sjöberg and P. Reichard, *J. Bio. Chem.*, 255, 6706-6709, **1980**

[76] O. Kahn, *Molecural Magnetism*, VCH Publishers, 135, **1993**

[77] A. Bencini and D. Gatteschi, *EPR of Exchange Coupled Systems*, Springer, New York, **1990**

[78] D. M. Kurtz Jr., *Chem. Rev.*, 90, 585-606, **1990**

[79] E. I. Solomon, T. C. Brunold, M. I, Davis, J. N. Kemsley S.-K. Lee, N. Lehnert, F. Neese, A. J. Skulan, Y.-S. Yang, and J. Zhou, *Chem. Rev.*, 100, 235-349, **2000**

[80] C. Galli, M. Atta, K. K. Andersson, A. Gräslund, and G. W. Brudvig, *J. Am. Chem. Soc.*, 117, 740-746, **1995**

[81] M. B. Yim, L. C. Kuo, and M. W. Makinen, *J. Magn. Res.*, 46, 247-256, **1982**

[82] S. C. Pulver, W. H. Tong, J. M. Bollinger, J. Stubbe, and E. I. Solomon, *J. Am. Chem. Soc.*, 117, 12664-12678, **1995**

[83] V. J. DeRose, K. E. Liu, S. J. Lippard, and B. M. Hoffman, *J. Am. Chem. Soc.*, 118, 121-134, **1996**

[84] B. E. Surgeon, D. Burdi, S. Chen, B. H. Huynh, D. E. Edmondson, J. Stubbe, and B. M. Hoffman, *J. Am. Chem. Soc.*, 118, 7551-7557, **1996**

[85] J. P. Willems, H. I. Lee, D. Burdi, P. E. Doan, J. Stubbe, and B. M. Hoffman, *J. Am. Chem. Soc.*, 119, 9816-9824, **1997**

[86] D. Burdi, B. E. Surgeon, W. H. Tong, J. Stubbe, and B. M. Hoffman, *J. Am. Chem. Soc.*, 118, 281-282, **1996**

[87] P. J. Riggs-Gelasco, L. Shu, S. Chen, D. Burdi, B. H. Huynh, L. Que Jr., and J. Stubbe, *J. Am. Chem. Soc.*, 120, 849-860, **1998**

[88] Y. Dong, and L. Que Jr., K. Kauffmann, and E. Münck, *J. Am. Chem. Soc.*, 117, 11377-11378, **1995**

[89] Y. Dong, Y. Zang, L. Shu, E. C. Wilkinson, and L. Que Jr., K. Kauffmann, and E. Münck, *J. Am. Chem. Soc.*, 119, 12683-12683, **1997**

[90] D. Lee, J. Du Bois, D. Petasis, M. P. Hendrich, C. Krebs, B. H. Huynh, and S. J. Lippard, *J. Am. Chem. Soc.*, 121, 19893-9894, **1999**

[91] A. M. Valentine, P. Tavares, A. S. Pereira, P. Davydov, C. Krebs, B. M. Hoffman, D. E. Edmondson, B. H. Huynh, and S. J. Lippard, J. Am. Chem. Soc. , 120, 2190-2191, 1998

[92] R. Davydov, S. Kuprin, A. Gräslund, and A. Ehrenberg, J. Am. Chem. Soc., 116, 11120-11128, 1994

[93] M. Atta, K. K. Andersson, R. Ingemarson, L. Thelander, and A. Gräslund, *J. Am. Chem. Soc.*, 116, 6429-6430, **1994**

[94] D. Lee, C. Krebs, B. H. Huynh, M. P. Hendrich, and S. L. Lippard, *J. Am. Chem. Soc.*, 122, 5000-5001, **2000**

[95] R. Davydov, S. Menage, M. Fontecave, A. Gräslund, A. Ehrenberg, *J. Bio. Inorg. Chem.*, 2:242-255, **1997**

[96] M. P. Hendrich, B. G. Fox, K. K. Andersson, P. G. Derbrunner, and L. D. Libscomb, *J. Bio. Chem.*, 267, 261-267, **1992**

[97] B. G. Fox, M. P. Hendrich, K. K. Surerus, K. K. Andersson, W. A. Froland, J. D. Lipscomb, and E. Münck, *J. Am. Chem. Soc.*, 115, 3688-3701, **1993**

[98] C. Krebs, R. Davydov, J. Baldwin, B. M. Hoffman, J. M. Bollinger Jr., and B. H. Huynh, *J. Am. Chem. Soc.*, 122, 5327-5336, **2000**

[99] F. Himo and L. A. Eriksson, *J. Phys. Chem. B*, 101, 9811-9819, **1997**

[100] S. Un, X. Tang, A. B. Diner, *Biochemistry*, 35, 679-684, **1996**

[101] W. Hofbauer, A. Zouni, R. Bittl, J. Kern, P. Orth, F. Lendzian, P. Fromme, H. T. Witt, and W.Lubitz, *Proc. Natl. Acad. Sci.*, Vol. 98, 12, 6623-6628, **2001**

[102] K. A. Campbell, J. M. Peloquin, X.-S. Tang, D. A. Chisholm, R. D. Britt, *J. Am. Chem. Soc.*, 119, 4787-4788, **1997**

[103] D. A. Force, D. W. Randall, R. D. Britt, X.-S. Tang, and B. A. Diner, *J. Am. Chem. Soc.*, 117, 12643-12644, **1995**

[104] O. Burghaus, M. Plato, M. Rohrer, and K. Möbius, *J. Phys. Chem.*, 97, 7639-7647, **1993**

[105] O. Nimz, F. Lendzian, C. Boullais, and W. Lubitz, *Applied Magn. Res.* 14, 255-274, **1998**

[106] A. Carrington, A. D. McLachlan, *Introduction to Magnetic Resonance*, Harper & Row, New York, **1969**

[107] M. Kolberg, Dissertation, in preparation

[108] M. Kolberg, G. Bleifuss, S. Pötsch, A. Gräslund, W. Lubitz, G. Lassmann, and F. Lendzian, *J. Am. Chem. Soc.*, 122, 9856-9857, **2000**

[109] M. Kolberg, G. Bleifuss, D. Logan, S. Pötsch, B.-M. Sjöberg, W. Lubitz, F. Lendzian, and G. Lassmann, in preparation

[110] F. Neese, Dissertation, Universität Konstanz, Konstanz, **1996**

[111] R. Aasa, T. Vänngård, *J. Magn. Res.*, 19, 308, **1975**

[112] R. Fiege, Dissertation, Technical University Berlin, Berlin 1995

[113] I. H. Karkoff, N. C. Brown, and P. Reichard, *Cancer Res.*, 28 1559-1565, **1968**

[114] J. G. DeWitt, J. G. Bentsen, A. C. Rosenzweig, B. Hedman, J. Green, S. Pilkington, G. C. Papaefthymiou, H. Dalton, K. O. Hodgson, and S. J. Lippard, *J. Am. Chem. Soc.*, 113, 9219-9235, **1994**

[115] B. G. Fox, Y. Liu, J. E. Dege, and J. D. Libscomb, *J. Biol. Chem.*, 266, 540-550, **1991**

[116] H. Zheng, S. J. Yoo, E. Münck, and L. Que Jr., *J. Am. Chem. Soc.*, 122, 3789-3790, **2000**

[117] V. L. MacMurdo, H. Zheng, and L. Que Jr., *Inorg. Chem.*,39, 2254-2255, **2000**

[118] K. Jayaraj, A. Gold, R. N. Austin, and L. M. Ball, J. Terner, D. Mandon, R. Weiss, J. Fischer, and A. DeCian, E. Bill, M. Müther, V. Schünemann, and A. X. Trautwein, *Inorg. Chem.*, 36, 4555-4566, **1997**

[119] J. W. A. Coremans, O. G. Poluektov, E. J. J. Groenen, G. C. M. Warmerdam, G. W. Canters, H. Nar, and A. Messerschmidt, *J. Phys. Chem.*, 100, 19706-19713, **1996**

[120] R. A. Isaacson, F. Lendzian, E. C. Abresch, W. Lubitz, and G. Feher, *Biophysical Journal*, 69, 311-322, **1995**

[121] U. K. Laemmli, *Nature*, 227, 680-685, **1970**

[122] P. Nordlund, U. Uhlin, C. Westergren, T. Joelsen, B.-M. Sjöberg, and H. Eklund, *FEBS Letters*, 258, 251-254, **1989**

[123] P. Nordlund, Dissertation, Sveriges Lantbruksuniversitet, Uppsala, **1990**

[124] A. Stesmans and G. vanGorp, *Rev. Sci. Instrum.*, 60, 2949-2952, **1989**

[125] C. Gessner, Dissertation, Techn. Univ. Berlin, Berlin, **1996**

[126] A. Kamlowski, Dissertation, Techn. Univ. Berlin, Berlin, **1997**

[127] P. Bertrand and J.-P. Gayda, *Biochim. Biophys. Acta*, 579, 107-121, **1979**

[128] C. Gessner, O. Trofanchuk, K. Kawagoe, Y. Higuchi, N. Yasuoka, and W. Lubitz, *Chem. Phys. Lett.*, 256, 518-524, **1996**

[129] O. Trofanchuk, M. Stein, Ch. Gessner, F. Lendzian, Y. Higuchi, and W. Lubitz, *J. Biol. Inorg. Chem.*, 5, 36-44, **2000**

[130] V. Schünemann, personal communication

[131] D. T. Logan, F. deMaré, B. O. Persson, A. Slaby, B. M. Sjöberg, and P. Nordlund, *Biochemistry*, 37, 10798-10807, **1998**

[132] M. D. Snodin, L. Ould-Moussa, U. Wallmann, S. Lecomte, L. Bachler, E. Bill, H. Hummel, T. Weyhermüller, P. Hildebrandt, and K. Wieghardt, *Chem. Eur. J.*, 5, 2554-2565, **1999**

[133] A. Liu, S. Pötsch, and A.Gräslund, B.-M. Sjöberg and M. Sahlin, G. Lassmann and F. Lendzian, in preparation

[134] J. Telser, H. Huang, H.-I. Lee, M. W. W. Adams, and B. M. Hoffman, *J. Am. Chem. Soc.*, 120, 861-870, **1998**

[135] J. M. Mouesca, L. Noodleman, D. A. Case, and B. Lamotte, *Inorg. Chem.*, 34, 4347-4359, **1995**

[136] H.-I. Lee, B. J. Hales, and B. M. Hoffman, *J. Am. Chem. Soc.*, 119, 11395-11400, **1997**

[137] C. Gessner, Dissertation, Technical University Berlin, Berlin **1996**

[138] R. E. Watson, A. J. Freeman, *Phys. Rev.*, 123, 2027, **1961**

[139] W. T. Oosterhuis, G. Lang, *Phys. Rev.*, 178, 439-456, **1969**

[140] P. G. Debrunner, *Hyperfine Interact*, 53, 21-36, **1990**

[141] T. A. Kent, B. H. Huynh, and E. Münck, *Proc. Natl. Acad. Sci.*, Vol. 77, 11, 6574-6576, **1980**

[142] N. Ravi, J. M. Bollinger,Jr.,B. H. Huynh, D. E. Edmondson, and J. Stubbe, *J. Am. Chem. Soc.*, 116, 8007-8014, **1994**

[143] R. J. Gurbiel, C. J. Batie, M. Sivaraja, A. E. True, J. A. Fee, B. M. Hoffman, and D. P. Ballou, *Biochemistry*, 28, 4861-4871, **1989**

[144] V. Schünemann and H. Winkler, *Rep. Prog. Phys.*, 63, 263-353, **2000**

[145] C. I. H. Ashby, C. P. Cheng, and T. L. Brown, *J. Am. Chem. Soc.*, 100, 6057-6063, **1978**

[146] C. P. Keijzers, E. J. Reijerse, P. Stam, M. F. Dumont, and M. C. M. Gribnau, *J. Chem. Soc. , Faraday Trans 1*, 83, 3493-3503, **1987**

[147] J. W. A. Coremans, O. G. Poluektov, E. J. J. Groenen, G. W. Canters, H. Nar, and A. Messerschmidt, *J. Am. Chem. Soc.*, 118, 12141-12153, **1996**

[148] J. W. A. Coremans, O. G. Poluektov, E. J. J. Groenen, G. W. Canters, H. Nar, and A. Messerschmidt, *J. Am. Chem. Soc.*, 119, 4726-4731, **1997**

[149] F. Lendzian, J. Rautter, H. Käß A. Gardiner, and W. Lubitz, *Ber. Bunsenges. Phys. Chem.*, 100, 2036-2040, **1996**

[150] D. T. Edmonds and C. P. Summers, *J. Magn. Res.*, 12, 134, **1973**

[151] R. Blinc, M. Mali, R. Osredkar, J. Seliger, and L. Ehrenberg, *Chem. Phys. Lett.*, 28, 158, **1974**

[152] G. F. Bryce, *J. Phys. Chem.*, 70, 3549-3557, **1966**

[153] R. S. Magliozzo and J. Peisach, *Biochemistry*, 32, 8446-8456, **1993**

[154] M. Fahnenschmidt, Dissertation, Technical University of Berlin, Berlin **2000**

[155] M. M. Werst, C. E. Davoust, and B. M. Hoffman, *J. Am. Chem. Soc.*, 113, 1533-1538, **1991**

[156] B. M. Hoffman, V. J. DeRose, P. E. Doan, R. J. Gurbiel, A. L. P. Houseman, and J. Telser, *Biological Magnetic Resonance*, Vol. 13, Plenum Press N. Y. London, **1993**

[157] C. J. Bender, A. C. Rosenzweig, S. J. Lippard, and J. Peisach, *J. Biol. Chem.*, 269, 15993-15998, **1994**

[158] J. R. Morton, K. F. Preston, *J. Magn. Reson.*, 30, 577-582, **1978**

[159] C. P. Scholes, A. Lapidot, R. Mascarenhas, T. Inubushi, R. A. Isaacson, G. Feher, *J. Am. Chem. Soc.*, 104, 2724-2735, **1982**

[160] V. J. deRose, K. E. Liu, D. M. Kurtz, B. M. Hoffman, and S. J. Lippard, *J. Am. Chem. Soc.*, 115, 6440-6441, **1993**

[161] H. Thomann, M. Bernardo, J. M. McCormick, S. Pulver, K. K. Andersson, J. D. Libscomb, and E. I. Solomon, *J. Am. Chem. Soc.*, 115, 8881-8882, **1993**

[162] K.-O. Schäfer, R. Bittl, W. Zweygart, F. Lendzian, G. Haselhorst, T. Weyhermüller, K. Wieghardt, and W. Lubitz, *J. Am. Chem. Soc.*, 120, 13104-13120, **1998**

Danksagung

Zuallererst möchte ich meinen Betreuern, den Leitern des Projekts, Dr. habil. Günter Laßmann und Dr. Friedhelm Lendzian ganz besonders danken, zunächst einmal, dass sie diese interessante Arbeit überhaupt möglich gemacht haben, vorallem aber auch für ihr großes Engagement und ihre Unterstützung während meiner Promotion, durch die ich sehr viel über magnetische Resonanzmethoden und Enzymologie gelernt habe und ohne die diese Arbeit überhaupt nicht möglich gewesen wäre. Ganz besonderer Dank gilt natürlich Matthias Kolberg, der ebenfalls im Rahmen seiner Promotion an diesem Projekt gearbeitet hat. Matthias war insbesondere für den biochemischen Teil des Projekts verantwortlich, während meine Aufgabe der spektroskopische Teil war. Die Arbeit mit ihm hat mir sehr viel Spaß gemacht. Matthias war sich nie zu Schade, mir allzu oft ahnungslosem Physiker die Grundlagen der Biochemie nahe zu bringen und alle Fragen geduldig zu beantworten. Vorallem aber hat er nicht nur im biochemischen Teil des Projekts hervorragende Arbeit geleistet, sondern gleichermaßen auch ganz entscheidend zu dem Erfolg der EPR Messungen und deren Auswertung beigetragen. Aber auch im privaten Bereich werde ich vorallem die sonntäglichen Kino- und Kneipenabende mit ihm und Taryn (und im letzten Jahr immer öfter auch Wulf, was eine große Bereicherung war) nicht vergessen, die Erholung in den oft harten Arbeitsalltag brachten.
Besonderen Dank möchte ich auch dem Leiter der Arbeitsgruppe, Prof. Dr. Wolfgang Lubitz, sagen, der sich immer mit großem Engagement für seine Mitarbeiter eingesetzt hat, für alle Fragen immer ein offenes Ohr hatte. Der Dank gilt vorallem für seine fachliche Unterstützung, die Zuverfügungstellung des Puls-EPR und Puls-ENDOR Gerätes und sein stetiges Interesse am Erfolg dieses Projekts.
Herzlich danken möchte ich Wulf Hofbauer: Wulf hat mit seiner großen Hilfsbereitschaft und seinem bemerkenswerten Fachwissen dem Projekt entscheidend mit zum Erfolg geholfen. Er war zu jeder Unterstützung bereit, besonders bei den Messungen im W-Band und bei der Auswertung der Kristallspektren, aber nicht nur dort. Danken möchte ich auch allen anderen Mitarbeitern (soweit möglich in alphabetischer Reihenfolge): Dr. Robert Bittl (insbesondere für die Einführung in die Puls EPR/ENDOR), Beatrix Blümel, Marc Brecht, Celine Elsässer, Dr. Monika Fahnenschmidt (insbesondere für die Einführung in MAGRES), Stefanie Förster, Dr. Petra Fromme, Jan Kern, Dr. Athina Zouni (den drei letztgenannten insbesondere für die Hilfe bei der Röntgenanalyse des R2-Y122H Kristalls), Dr. Catherine Fursman, Irene Geißenheimer, Raffael Jordan (insbesondere für die Beratung in PC Fragen), Michael Kammel, Rolf Kunert (insbesondere für seine Bereitschaft, jegliche noch so komplizierte Konstruktion, die wir Wissenschaftler uns ausgedacht haben, in seiner mechanischen Werkstatt zu verwirklichen), Dr. Johannes Messinger, Dr.

Frank Müh (für seine Präparationsarbeit in unserem Projekt), Kai Schäfer (für die Bereitstellung und Einführung in sein selbstgeschriebenes Simulationsprogramm, die Einführung in SPLEEN und seine Arbeit als Beauftragter für Kühlgase) , Matthias Stein (insbesondere für die Einführung in INSIGHT und das Gessnersche Kristallsimulationsprogramm), Herrn Schneider, Claudia Schulz, Christian Teutloff (insbesondere für die Unterstützung bei den ENDOR Messungen), Olga Trofanchuk, Herrn Wenzel und Herrn Richter von der Elektronikwerkstatt, Dr. Heike Witt.

Danken möchte ich auch Prof. Astrid Gräslund von der Universität in Stockholm, die das Projekt zur Mutation von R2 an der Stelle Y122 b.z.w Y177 zusammen mit Dr. habil. Günter Laßmann ins Leben gerufen und betreut hat, für die hervorragende Kooperation und Prof. Britt-Marie Sjöberg für ihre Unterstützung des Projekts (insbesondere durch die Anleitung von Dr. Stephan Pötsch und Matthias Kolberg bei der Proteinpräparation für die Mutanten). Mein Dank gilt inbesondere auch Dr. Stephan Pötsch (von der Universität Frankfurt) für die wichtige Arbeit, die er als unser Vorgänger und als Postdoc bei Astrid Gräslund in dem Projekt geleistet hat sowie insbesondere für die R2-Y122H Kristalle, die er gezüchtet hat, und die Bereitschaft, uns bei allen Fragen bereitwillig zu helfen. Ebenso möchte ich Prof. Dr. Pär Nordlund und Prof. Dr. Derek Logan von der Universität Stockholm danken für Röntgenstrukturaufklärung der R2-Y122H Kristalle und die bereitwillige Unterstützung bei allen Fragen, die die Kristallstruktur betrafen.

Lebenslauf

Persönliche Daten

Name	Günther Bleifuß
Anschrift	Bahnhofstraße 45
	63743 Aschaffenburg

Schulausbildung

1979-1983	Grundschule Aschaffenburg/Obernau
1983-1992	Kronberggymnasium Aschaffenburg
	Abschluß: Abitur

Zivildienst

07/1992-09/1993	Ableistung des Zivildienstes im Altenheim des katholischen Frauenbundes in Aschaffenburg

Hochschulausbildung

09/1993-07/1996	Studium der Physik (Diplom) an der Universität Würzburg Vordiplom: 07/1995
08/1996-08/1997	Studium an der University of Texas at Austin Abschluß: master of arts in Physik Thema der Abschlußarbeit: *Measurement of the Yttrium Nuclear Spin-Spin Relaxation Time in* $La_{1.5}Y_{0.5}CuO_4$ *above Roomtemperature*
09/1997-	Beginn der Promotion in der Arbeitsgruppe von Prof. Dr. Lubitz unter der Leitung von Dr. habil. Laßmann und Dr. Lendzian